University of South Carolina
Scholar Commons

Theses and Dissertations

1-1-2013

Boiling and Evaporation on Micro/nanoengineered Surfaces

Xianming Dai
University of South Carolina

Follow this and additional works at: https://scholarcommons.sc.edu/etd

 Part of the Mechanical Engineering Commons

Recommended Citation

Dai, X.(2013). *Boiling and Evaporation on Micro/nanoengineered Surfaces.* (Doctoral dissertation). Retrieved from https://scholarcommons.sc.edu/etd/2333

This Open Access Dissertation is brought to you by Scholar Commons. It has been accepted for inclusion in Theses and Dissertations by an authorized administrator of Scholar Commons. For more information, please contact digres@mailbox.sc.edu.

BOILING AND EVAPORATION ON MICRO/NANOENGINEERED SURFACES

by

Xianming Dai

Bachelor of Science
Chongqing University, 2007

Master of Science
Huazhong University of Science and Technology, 2009

Submitted in Partial Fulfillment of the Requirements

For the Degree of Doctor of Philosophy in

Mechanical Engineering

College of Engineering and Computing

University of South Carolina

2013

Accepted by:

Chen Li, Major Professor

Jamil Khan, Committee Member

Xinyu Huang, Committee Member

Roger Dougal, Committee Member

Guiren Wang, Committee Member

Lacy Ford, Vice Provost and Dean of Graduate Studies

© Copyright by Xianming Dai, 2013
All Rights Reserved.

DEDICATION

God created the world. Scientists are working to understand the world and engineers are working to develop the world based on sciences. May all the discoveries and inventions be filled with the glory of the Lord.

ACKNOWLEDGEMENTS

In experimental philosophy we are to look upon propositions collected by general induction from phenomena as accurately or very nearly true, notwithstanding any contrary hypotheses that may be imagined, till such time as other phenomena occur, by which they may either be made more accurate, or liable to exceptions. This rule we must follow to ensure that the argument of induction may not be evaded by hypotheses.

----Isaac Newton

I would like to thank those who directly or indirectly gave me faith, reason, knowledge and truth to make me as a human being. Without those ancient sages, such as Isaac Newton, who provided me methodologies to conduct my research, I will not be able to finish my dissertation.

At this time, I greatly appreciate my advisor Professor Chen Li's guidance and kind help during my Ph. D. studies. He is a nice mentor with great patience and helps me develop a professional personality for my future career. I would also thank my parents, brothers and sisters, committee members, labmates and friends. Your encouragements and continuous supports are greatly appreciated.

I thank you all in my life. It is you that made me who I am.

ABSTRACT

Two-phase transport is widely used in energy conversion and storage, energy efficiency and thermal management. Surface roughness and interfacial wettability are two major impact factors for two-phase transport. Micro/nanostructures play important roles in varying the surface roughness and improving interfacial wettability. In this doctoral study, five types of micro/nanoengineered surfaces were developed to systematically study the impacts of interfacial wettability and flow structures on nucleate boiling and capillary evaporation. These surfaces include: 1) superhydrophilic atomic layer deposition (ALD) coatings; 2) partially hydrophobic and partially hydrophilic composite interfaces; 3) micromembrane-enhanced hybrid wicks; 4) superhydrophilic micromembrane-enhnaced hybrid wicks, and 5) functionalized carbon nanotube coated micromembrane-enhnaced hybrid wicks.

Type 1 and 2 surfaces were developed to investigate the impacts of intrinsic superhydrophilicity and hydrophobic-hydrophilic composite wettability on nucleate boiling. Superhydrophilicity was achieved by depositing nano-thick ALD TiO_2 coatings, which were used to enable intrinsically superhydrophilic boiling surfaces on the microscale copper woven meshes. Critical heat flux (CHF) was substantially increased because of the superwetting property and delayed local dryout. Carbon nanotube (CNT) enabled partially hydrophobic and partially hydrophilic interfaces were developed to form ideal cavities for nucleate boiling. The hydrophobic-hydrophilic composite interfaces were synthesized from functionalized multiwall carbon nanotubes (FMWCNTs)

by introducing hydrophilic functional groups on the surfaces of pristine MWCNTs. The nanoscale FMWCNTs with heterogeneous wettabilities were coated on the micromeshes to form hierarchical surfaces, which effectively increase the heat transfer coefficient (HTC) and CHF of pool boiling.

To enhance capillary evaporation, micromembrane-enhanced capillary evaporating surfaces, i.e., type 3 surfaces, were developed to separate liquid flows and capillary pressure generation. This new type of surfaces consists of a microchannel array and a micromembrane made from a single layer of micromesh. The capillary evaporation CHF were substantially increased because of the increased capillary pressure provided by micromeshes and the reduced friction drag resulted from microchannels. Based on this newly developed hybrid wick, the effect of interfacial wettability on capillary evaporation was systematically studied. Firstly, superhydrophilic ALD SiO_2 was deposited on this type of hybrid wick to create intrinsically superhydrophilic interfaces, i.e., type 4 surfaces, resulting in significantly increased HTC because of the enhanced thin film evaporation on micromeshes. Secondly, CNT-enabled hydrophobic-hydrophilic composite interfaces were deposited on the hybrid wicks to increase the nucleate site density, bubble departure frequency and reduce friction drag. Both nucleate boiling and thin film evaporation were improved, resulting in enhanced HTC and CHF.

In conclusion, the interfacial wettability of micro/nanoengineered surfaces can significantly alter bubble dynamics such as nucleation site density, bubble departure diameter and frequency. Superhydrophilic surface can substantially increase the boiling CHF because of the superwetting property. In addition, more hydrophobic surfaces yield higher HTC, while more hydrophilic surfaces result in higher CHF. The partially

hydrophobic and partially hydrophilic surfaces perform better than both superhydrphobic and superhydrophilic surfaces. The separation of liquid flow and capillary pressure generation can be achieved using micromembranes, resulting in dramatically increased CHF. Improved wettability can result in better wettings and enhanced thin film evaporation. Hydrophobic and hydrophilic nanoporous coatings can improve the wetting and reduce the friction, resulting in enhanced HTC and CHF simultaneously.

TABLE OF CONTENTS

LIST OF TABLES

LIST OF FIGURES

LIST OF SYMBOLS

A	Area of cross section.
C_f	Compress factor.
d	Diameter of copper mesh.
D_b	Bubble departure diameter.
D_h	Hydrodynamic diameter.
D_p	Equivalent spherical diameter of porous media.
f	Friction factor.
f_b	Bubble departure frequency.
h	Heat transfer coefficient.
h_{fg}	Specific enthalpy.
k	Thermal conductivity of copper.
L	Length along the macroscopic.
L_0	Pressure gradient in porous media microchannel length.
M	Mesh number.
N_A	Number of active nucleation sites.
R_e	Reynolds number.
S_v	Surface area per unit volume of solid phase.
T_5	Temperature of the thermocouple.
q''	Input heat flux.
Q	Flow rate.

v_s Superficial velocity.

Δp Pressure drop.

ΔT Temperature difference between two thermocouples.

Δx Distance between two thermocouples.

$\Delta x'$ Distance from T_{C5} to the evaporating surface.

β, γ Constant number.

μ Fluid viscosity.

E Porosity

ρ Fluid density

ρ_g Vapor density

List of Abbreviations

ALD ..... Atomic Layer Deposition

CHF ..... Critical Heat Flux

CNT ..... Carbon Nanotube

FMWCNTs ..... Functionalized Multiwall Carbon Nanotubes

F-FMWCNT ..... Fluorinated FMWCNT

HTC ..... Heat Transfer Coefficient

MWCNTs ..... Multiwall Carbon Nanotubes

NFMWCNT ..... Nafion and FMWCNT

PID ..... Proportional-Integral-Derivative

TC ..... Thermocouple

CHAPTER 1

INTRODUCTION

Thermal management is critical for electronic devices [1], batteries [2], fuel cells [3], light-emitting diode lightings [4], Air Force systems [5], power plants [6], et al. Phase change heat transfer can achieve high heat transfer coefficient (HTC) and reduce pumping power by taking advantage of the latent heat [7]. Boling and evaporation are the primary two modes of two-phase heat transports, which exhibit promising perspectives for micro/nanoscale thermal management.

1.1 BOILING HEAT TRANSFER

According to the boiling heat transfer theory [8], $h = q''/\Delta T$, h is the HTC, q'' is the heat flux and ΔT is the wall superheat. Here, $q'' = 1/6\pi D_b^3 \rho_g h_{fg} f_b N_A$, and D_b is the bubble departure diameter, ρ_g is the vapor density, h_{fg} is the specific enthalpy, f_b is the bubble departure frequency and N_A is the number of active nucleation sites. According to this correlation, to enhance boiling heat transfer at the identical superheat, we can increase the number of active nucleation sites and augment surface areas using micro/nanostructures [9-10]. In addition, improving the interfacial wettability can increase bubble growth rate and reduce bubble departure force, resulting in increased bubble departure frequency [11]. To increase the critical heat flux (CHF) of boiling heat transfer, efforts have been spent to delay the transition to film boiling. Both surface roughness [10] and interfacial wettability [12] have shown significant impacts on the CHF.

1.1.1 MICROSTRUCTURES

Microstructures have been widely used to enhance boiling and evaporation. Li et al. [13] investigated the boiling and evaporation on the copper woven meshes systematically, including the effects of thickness, mesh size and volumetric porosity. The maximum HTC and CHF for the sintered multiple layers of copper meshes were shown to be as high as 245.5 kW /m^2·K and 367.9 W /cm^2, respectively. Wei et al. [14] studied the effects of fin geometry on boiling heat transfer using silicon chips with micro-pin-fins, and then Chu et al. [10] studied the surface roughness-augmented wettability on CHF systematically with well defined microstructures. Liter et al. [15] investigated the CHF enhancement by modulated porous-layer coating using experimental and theoretical methods. They found the modulation separated the liquid and vapor phases, thus reducing the liquid-vapor counterflow resistance adjacent to the surface. The completely separated liquid and vapor flow paths resulted in substantial enhancement of CHF. Subsequently, Min et al. [16] studied the two dimensional (2-D) and three dimensional (3-D) modulated porous coatings for enhanced boiling, respectively. They found 2-D coatings behaved similar to the 3-D coatings by carbon-molding in modulating the stability of the vapor-liquid interface thus causing enhancement in the CHF. Li et al. [17] made different types of multiscale modulated porous structures and compared the liquid replenishing impacts on CHF and heat transfer coefficient of nucleate boiling. The modulated structures were shown to further enhance the CHF by delaying the onset of hydrodynamic instability when the vapor-liquid counterflow was separated by the pillars.

1.1.2 NANOSTRUCTURES

It has been indicated that nano-scale surface may not improve the nucleate boiling heat transfer, because the bubble nucleation process is hardly expected to be initiated in

nano-sized cavities based on the conventional theory [18-19]. However, silicon and copper nanowires were investigated to be superior to increase the nucleate site density and thus enhance the heat transfer rate [9]. Chen et al. claimed that the CHF could also be enhanced by the Si/Cu nanowires due to the superhydrophilicity and enhanced capillary effect [20]. Ahn et al. [21] reported the enhanced boiling heat transfer on the nanostructured surface made by carbon nanotube arrays. The "nano-fin″ effect was taken as the primary enhancement mechanisms.

1.1.3 HIERARCHICAL STRUCTURES

Hierarchical or hybrid structures combined the advantages of both microscale and nanoscale structures, resulting in robust superiorities to enhance the boiling heat transfer. Launay et al. [22] developed the hybrid micro-nano structured thermal interfaces for pool boiling. The conventional Si-etched microstructures performed better than the CNTs-based surfaces in all cases examined. This was mainly due to the change in the nature of surface-fluid interactions (i.e., rendering surface non-wetting) when pristine CNTs were used as the interface. McHale et al. [23] deposited the carbon nanotubes on the sintered microscale copper particles and rendered the hydrophobic CNTs to hydrophilic by E-beam evaporative deposition of pure copper. The CHF and heat transfer rate were both enhanced significantly. Ahn et al. [24] studied the micro, nano and micro/nano duplicated structures and demonstrated that the CHF enhancement on the modified surfaces was a consequence of both the improved surface wettability and the liquid spreading ability. The micro/nanostructured surface had the greatest liquid spreading ability and the maximum CHF.

1.1.4 INTERFACIAL WETTABILITY

The mechanism of the micro/nanostructure enhanced boiling heat transfer attributes to the augmented surface areas, increased nucleate site density and enhanced capillary effects. The superhydrophilicity of the micro/nano structured surface primarily results from the Wenzel effect [25]. Hence, those structured interfaces are just apparently superhydrophilic. Increasing the intrinsic interfacial wettability is able to promote the evaporative rate of the thin film liquid layer inside the bubble. Phan et al. [26] studied the influences of the surface wettability on nucleate boiling. They made nanocoatings to vary the water contact angle from 20^o to 110^o by modifying the nanoscale surface topography. The more hydrophobic interfaces were found to have a smaller bubble departure diameter and larger bubble departure frequency. Bourdon et al. [27] concluded that significant reduction of the superheat at the onset of incipient boiling due to the enhanced wettability. Jo et al. [28] compared the nucleate boiling on hydrophilic SiO_2 and hydrophobic Teflon nanostructured surfaces, respectively. The SiO_2 coated interface could reach a higher CHF but a lower HTC. The improved surface wettability and capillary effect contributed to the CHF enhancement, while the decreased nucleate site density determined the deteriorative heat transfer performance. Moreover, the SiO_2 obtained by the plasma treatment was not reliable. Takata et al. [29] coated the plain copper with TiO_2 and maintain the superhydrophilicity with UV light. The CHF was promoted by approximately 200% and heat transfer rate was improved as well. However, Feng et al. [30] reported that the CHF was promoted by 200% on the alumina coated Pt wire using atomic layer deposition but without apparent change in heat transfer rate.

1.1.5 MY WORK ON BOILING HEAT TRANSFER

Base on the brief literature review of the previous work, we can see that the effects of interfacial wettability in the porous and hierarchical structures have barely been reported due to the difficulty in depositing conformal hydrophilic coatings on the high aspect ratio surfaces. Further investigations on the fundamental issues of the interfacial effects on bubble dynamics and thin film evaporation still need to be done.

To distinguish the effects of surface roughness and interfacial wettability, this work systematically studied the intrinsic wettability on heat transfer enhancement. First, intrinsically superhydrophilic porous structures were obtained by depositing conformal Titania (TiO_2) on microscale copper woven meshes using atomic layer deposition (ALD) technique. Second, partially hydrophobic and partially hydrophilic composite interfaces were synthesized from functionalized multiwall carbon nanotubes (FMWCNTs) by introducing hydrophilic functional groups on the surfaces of pristine multiwall carbon nanotubes (MWCNTs). The synthesized FMWCNTs with composite wettability were then coated on the microscale copper woven meshes to form hierarchical structures with heterogeneous wettabilities. The intrinsically superhydrophilic TiO_2 coated porous structures and FMWCNTs enabled hierarchical structures were superior to pool boiling enhancement.

1.2 EVAPORATION HEAT TRANSFER

Capillary evaporation [31] is one of the most efficient heat transfer modes and has been widely used in heat exchangers [32] and heat pipes [33-35]. Evaporators with high HTC and CHF are highly desirable for compact heat exchangers for high heat flux applications [36-37]. To increase the evaporative HTC, we can augment the surface area

using porous structures [13] or improve intrinsic interfacial wettability to achieve enhanced thin film evaporation as indicated in the theoretical model [38]. To increase the evaporative CHF, high capillary pressure and simultaneous low flow resistance are required to maintain sufficient liquid supply to avoid the dryout.

1.2.1 LITERATURE REVIEW OF CAPILLARY EVAPORATION

Most of porous coatings used in enhancing capillary evaporation are usually mono-porous structures [39]. For example, sintered particles and powders were developed to substantially enhance thin film evaporation HTC [39-40]. The effects of porosity, wick thickness and other factors on the optimal design of the wicking structures were also examined [39-40]. Copper woven mesh laminates [41-44] were extensively studied to enhance the capillary evaporation HTC due to the augmented surface areas and increased capillary forces. However, the flow resistances in these microscale mono-porous structures remain high, resulting in low CHFs due to the liquid supply crisis. Micro-grooves [45-46] or channels [47] were superior for liquid supply because of the attributed low flow resistance, but the capillary forces induced by the disjoining pressure differences in grooves [46] were still too low to reach high CHFs.

This brief review shows that both the microscale mono-porous structures (such as sintered meshes or particles/powders) and micro-grooves or channels cannot meet the needs of high heat flux applications. To solve this dilemma, various types of bi-porous surfaces were proposed and developed [35, 48-52]. Semenic et al. [49, 51] found that biporous surface of sintered powders performed better than the mono-porous copper wicks because the working fluid can be supplied to the hot spots through micropores inside the clusters even though the voids were filled with vapor. Cao et al. [53] reported

that when a mono-dispersed wick was replaced by bi-dispersed wicks with the same small pore diameter, both HTC and CHF were increased significantly. Cai et al. [36] studied the heat transfer performance on the carbon nanotube bi-porous structures, which consisted of carbon nanotube (CNT) array separated by microchannels. The nanoscale pores in the CNT bi-porous structure provided ultrahigh capillary pressure and augmented surface areas, which significantly reduced the menisci radii and increased thin-film evaporation area and evaporation efficiency. Ćoso et al. [54] examined a type of bi-porous media consisting of microscale pin fins periodically separated by microchannels to simultaneously increase the heat dissipation capacity as well as the HTC of the evaporator wick. Some of the bi-porous wicks have also been integrated in heat pipes [50, 55-57] to decrease the thermal resistance and increase working heat fluxes. Heat pipe performance was found to be greatly enhanced by applying modulated wick because of enhanced axial capillary liquid flows and extra evaporation surface area resulting from the cross-sectional area [35]. In these reported bi-porous structures, the main fluid passages were still through the micro or nanoscale mono-porous structures (such as microscale powders or CNTs). As a result, the overall liquid flow resistances still remain high.

1.2.2 MY WORK ON EVAPORATION HEAT TRANSFER

Inspired from tree transpirations and water transport processes, a micromembrane-enhanced hybrid wick, which consisted of a microchannel array covered by a single layer copper mesh screen, was developed to increase evaporation HTC and CHF. In this structures, micromeshes provide high capillary forces and microchannels can reduce the flow resistance, resulting in sufficient liquid supply to reach high heat flux.

In addition, the micromesh can not be flooded since the liquid flows through the microchannels, resulting in thin film evaporation on micromeshes.

The interfacial wettability of this newly developed hybrid wick was tuned to study the effect of wettability on liquid supply and thin film evaporation. Two types of nanocoatings, superhydrophilic ALD SiO_2 and partially hydrophobic and partially hydrophilic FMWCNTs, were utilized to enhance capillary evaporation. The intrinsically superhydrophilic ALD SiO_2 coated hybrid wick was demonstrated to significantly enhance the HTC. In addition, hydrophobic-hydrophilic FMWCNTs coated hierarchical hybrid wicks with heterogeneous wettability were superior to enhance capillary evaporation HTC and CHF in this study.

1.3 SUMMARY OF THE INTRODUCTION

Surface roughness and interfacial wettability are the two critical impact factors for boiling and evaporation. Since many people studied various types of structures, this study focused more on the effect of wettability. Using two layer sintered copper meshes as the base, superhydrophilic ALD TiO_2 and hydrophobic and hydrophilic FMWCNTs were employed to enhance nucleate boiling. Then the micromembrane-enhanced hybrid wicks were developed to enhance capillary evaporation. Based on this structure, superhydrophilic ALD SiO_2 and hydrophobic and hydrophilic FMWCNTs were used to enhance capillary evaporation.

CHAPTER 2

CONFORMAL NANO-TITANIA COATINGS FOR ENHANCED NUCLEATE BOILING

Conformal nano-thick titania (TiO_2) was deposited on two layer copper woven meshes by atomic layer deposition (ALD) technique. The surface morphologies were maintained without taking big surface roughness on each copper wire. The intrinsic surface wettabilities were significantly improved. Nucleate boiling CHF was dramatically increased from 141.8 W/cm^2 on bare two layer meshes to 194.5 W/cm^2 on ALD TiO_2 coated two layer meshes. The improved wettability substantially enhanced the wetting of the "microlayers″, resulting in delayed local dryout and increased CHF.

2.1 INTRODUCTION OF NUCLEATE BOILING ENHANCEMENT TECHNIQUES

Nucleate boiling, as one of the most efficient heat transfer modes, is critical for energy conversion and thermal management [1, 3, 58-62]. Many approaches have been developed to enhance boiling heat transfer, such as increasing the nucleate site density, e.g. nanowires [9] and carbon nanotubes [23]; augmenting the surface areas, e.g. sintered particles[37, 63], copper woven meshes [13] and pin-fin structures [14], which can introduce more cavities as well; improving surface wettability, e.g. superhydrophilic coatings [30] and nanofluids [64-65], which is able to promote the rewetting of the "hot spot″ and delay the dryout; partially hydrophilic and partially hydrophobic interfaces [66-67], which proved ideal cavities for nucleate boiling. Most of the aforementioned

methods are based on surface modifications, which may introduce big roughnesses, create nucleate sites, increase surface areas, or improve surface wettabilities. To study a single impact factor of surface wettability, several intrinsically hydrophilic metal oxides, such as alumina (Al_2O_3) [30], silica (SiO_2) [68] and titania (TiO_2) [69], have been investigated to enhance nucleate boiling. Al_2O_3 coated platinum (Pt) wire was tested in de-ionized water and over 100% enhancement of CHF in pool boiling has been demonstrated in Peterson′s group [30]. TiO_2 coated plain surface was tested in pure water and the priority in increasing the HTC and CHF has been observed as well [69]. Johnathan [70] compared the heat transfer performance of both plain copper surface with hydrophilic coating in water and bare copper surface in Al_2O_3/water nanofluids. Interestingly, similar CHF enhancement was achieved because the nanoparticles deposited on the tested sample and dramatically improved the wettability, which was similar to the effect of hydrophilic coatings. Thus, investigating the effect of surface wettability is also very helpful to understand the mechanisms of those nanofluids with hydrophilic particles. Bare NiCr wire was tested in S_iO_2/water nanofluids [71] and plain copper surface was tested in Al_2O_3/water nanofluids [72], and both investigations found a dramatic CHF enhancement with no appreciable change in heat transfer. These were consistent with Feng′s observations [73] and again verified that the improved surface wettability contributed significantly to the CHF enhancement [70]. Whereas, a stainless steel disc was investigated in gamma phase Al_2O_3/water nanofluids [74] and a heating wire was tested in Al_2O_3/water nanofluids [75] and both of them demonstrated a dramatic heat transfer enhancement.

The aforementioned techniques substantially improved the interfacial wettability and surface energy. However, the TiO_2 coatings deposited on plain surface [69] using sputtering were not reliable. The Al_2O_3 coated single Pt wire did not show obvious HTC enhancement [30] and Al_2O_3 coating was not superior to prevent water corrosions [76]. Atomic layer deposition is able to grow conformal nano-thick coatings on the porous structures. Most recently, ALD TiO_2 has shown great capabilities in water corrosion resistance for copper protection [76]. The aging test has demonstrated that a 200 Å TiO_2 thin film is able to prevent the copper from corrosion in water for more than 80 days [76]. Intrinsically superhydrophilic ALD coated porous structures have not yet been reported due to the difficulty in coating high aspect ratio surfaces. In this study, conformal ALD TiO_2 coated copper woven meshes have been experimentally investigated in highly purified water to show the effects of improved wettability on heat transfer performances.

2.2 POOL BOILING TESTING AND DATA REDUCTION

A closed system was established for experimental study (Figure 2.1). The aluminum chamber was made as a reservoir. The inner walls were coated with high temperature polyester to reduce contamination. Two side walls of the chamber were covered by quartz glass as observation windows and the bottom of the chamber was used for sample assembly. The temperature was accurately controlled by a proportional-integral-derivative (PID) temperature controller. A compact water heat exchanger was used to condense and recycle the vapor to keep a constant water level. A pressure gauge was installed to monitor the vapor pressure in the chamber. Additionally, the water and vapor temperature inside the chamber were monitored by two T-type thermocouples.

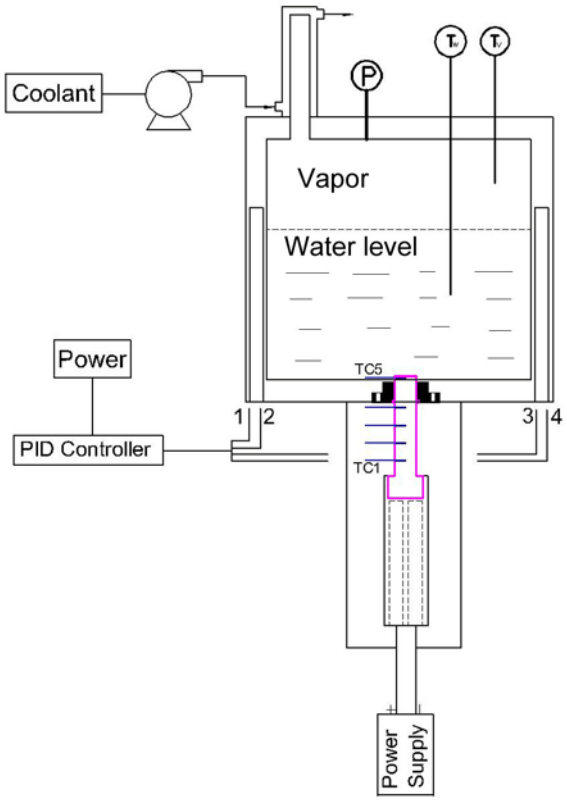

Figure 2.1 Experimental setup of pool boiling. TC-thermocouple; 1, 2, 3 and 4 are four heaters.

High purity water was degassed for at least two hours at approximately 99.9 ^{o}C to remove non-condensable gases prior to tests. Four cartridge heaters were installed in the corners of the aluminum chamber to maintain the water temperature between 99.8 ± 0.2 ^{o}C and 100.2 ± 0.2 ^{o}C to ensure saturated work condition.

Copper woven meshes were sintered on a TC block (Figure 2.2) by diffusion bonding technique to achieve good contact conditions. The whole structure was sintered in high temperature furnace at 1000 ^{o}C in hydrogen (H_2) atmosphere for 150 min. A copper heating block with 1 cm^2 cross-section area was used to generate one-dimensional (1-D) heat flux. In order to reach high heat flux, a pure copper heating block was made

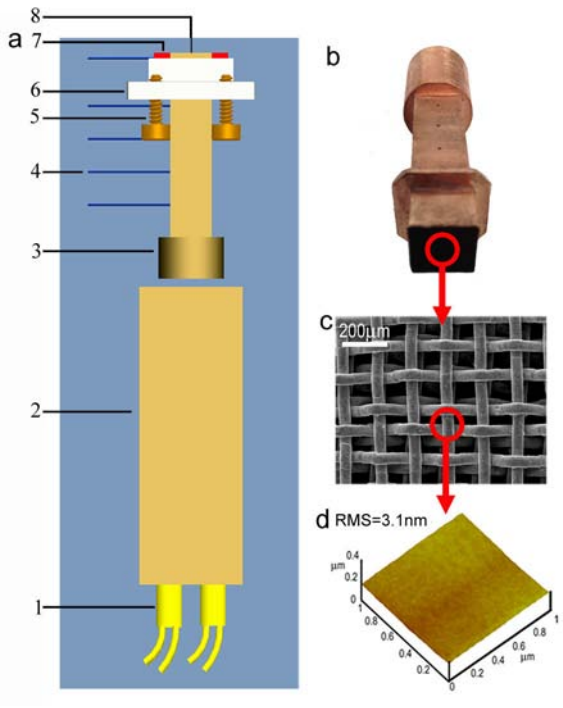

Figure 2.2 Schematic of the test sample assembly. (a) 1. 120V-500W 3/8" diameter × 4" long cartridge heater, 2. 1" square copper heating block with 4 holes on the bottom side for heaters and 1 hole on the top side, 3. 1 cm × 1 cm square copper block with holes for thermocouple (TC block) 4. 0.02″ diameter × 6″ long K type thermocouple, 5. Screw, 6. G-7 fiberglass, 7. High temperature RTV silicone . 8. 10 mm × 10 mm sintered copper woven meshes. (b) Two layer copper woven meshes sintered on TC block. (c) Scanning electron microscope (SEM) image of the two layer woven meshes. (d) Three dimensional atomic force microscopy (AFM) images of TiO_2 coated mesh surface.

with 4 holes for heaters on one side and a hole on the other side for the TC block. Thermal grease was used to enhance the contact conditions between the heating and TC blocks. The whole heating elements were finally insulated in an aluminum housing by Nelson Firestop Ceramic Fiber. G-7 Fiberglass was used to insulate the TC bock to ensure the 1-D heat conduction. Power supply was used to control the input power and five K type thermocouples (diameter 0.61mm) with linear temperature distribution were used to estimate the input heat flux (Figure 2.2). High temperature RTV silicone was used to seal the gaps between fiberglass and copper block. High temperature silicone was

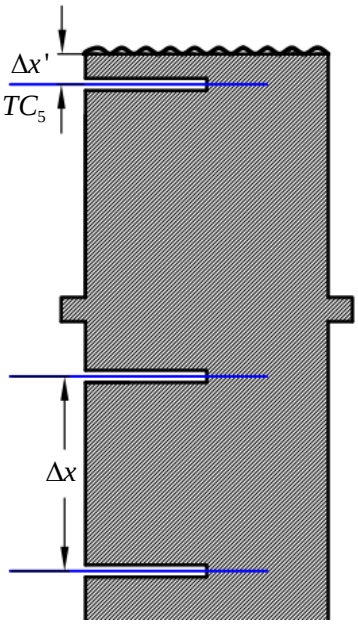

Figure 2.3 Thermocouple arrangement and parameters for data reduction.

Table 2.1 Dimensions of two layer meshes.

Samples	**Parameters**		
2 layer Mesh	Thickness: 0.16 mm	Wire diameter: 0.56 mm	Porosity: 0.72

also used to insulate the TC block inside the chamber, the thermocouple inside the chamber and the edge of the copper woven meshes, leaving only the woven mesh surfaces in the chamber for boiling.

Data reduction was conducted according to the parameters shown in Figure 2.3.

$$q'' = k\frac{\Delta T}{\Delta x} \tag{1}$$

$$T_s = T_5 - q''\frac{\Delta x'}{k} \tag{2}$$

$$h = \frac{q''}{T_w - T_{sat}} \tag{3}$$

The uncertainties of the temperature measurements, the length or width are ± 0.5 K, 0.01 mm, respectively. The Kline and McClintock method was used to estimate the uncertainties [77]: $\Delta y = [(\frac{\partial y}{\partial x_1}\Delta x_1)^2 + (\frac{\partial y}{\partial x_2}\Delta x_2)^2 + \cdots + (\frac{\partial y}{\partial x_n}\Delta x_n)^2]^{1/2}$. Estimations of uncertainties are: the heat flux was less than ± 3.2 W/cm^2; the heat transfer coefficient was less than ± 1.2 W/(cm^2·K); the superheat $\Delta T = T_w - T_{sat}$ was less than ± 0.8 °C.

2.3 ALD DEPOSITION OF T_IO_2

The deposition of active material TiO_2 on the conducting copper surface was carried out in a viscous-flow, hot-wall type ALD reactor as shown in Figure 2.4 [78]. The deposition was performed in static mode in order to conformal coat the high surface area copper woven meshes (made by Belleville Wire Cloth). Ultra high purity (UHP) grade N_2 was used as the carrier gas during the deposition. Base pressure of the reactor was kept at one Torr. Prior to the ALD coating process, two layer copper meshes were sintered on a 1×1 cm^2 copper block to achieve nearly perfect contact conditions. The whole structures were sintered in a high temperature furnace at approximately 1000 ^oC in hydrogen (H_2) atmosphere. Thereafter, ALD thin film was deposited at 150°C in a viscous-flow, hot-wall type ALD reactor [78]. The reactor was operated in flow/static mode for conformal growth of oxides on copper woven meshes. Ultra high purity nitrogen was used to maintain the reactor pressure at 0.9 Torr. Prior to the TiO_2 deposition, ALD Al_2O_3 was pre-deposited as a seed layer to facilitate the TiO_2 nucleation. The sequential dosing of titanium tetrachloride ($TiCl_4$) and water were used as the deposition technique [76, 78]: $TiCl_4 + 2H_2O \rightarrow TiO_2 + 4HCl$. Trimethylaluminum (TMA) and water chemistry were used for ALD Al_2O_3 [79]: $2Al(CH_3)_3 + 3H_2O \rightarrow Al_2O_3 + 3CH_4$. The chemistries used for ALD have been well studied and have been demonstrated to obtain high quality film

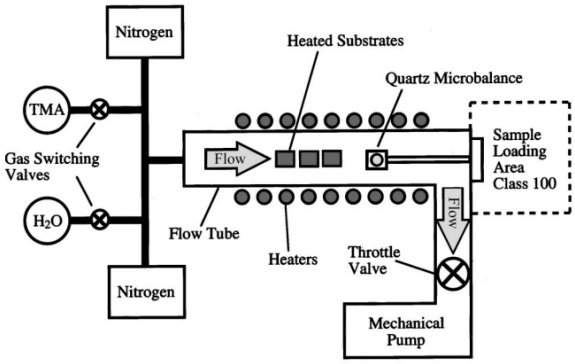

Figure 2.4 Schematic view of viscous flow reactor for ALD TiO_2 [78].

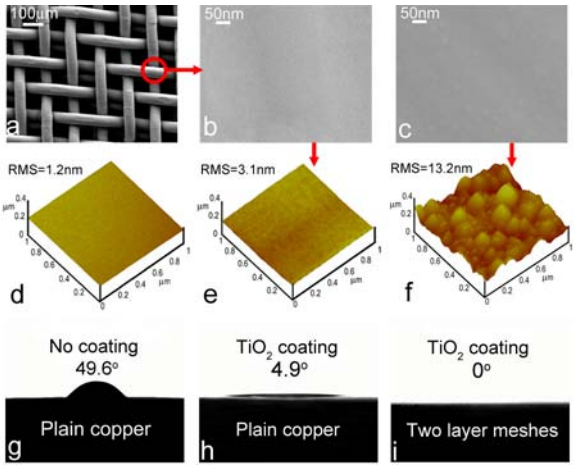

Figure 2.5 Characterization of the TiO_2 coated interfaces. (a) Two layer copper woven meshes. (b) SEM image of the surface morphology of the conformal TiO_2 coated mesh wire. (c) SEM image of the surface morphology of the rough TiO_2 coated mesh wire. (d) 3-D AFM image of the bare mesh wire. (e) 3-D AFM image of the conformal TiO_2 coated mesh wire. (f) 3-D AFM image of the rough TiO_2 coated mesh wire. (g, h and i) Contact angle measurement.

deposition [79-81].

2.4 CHARACTERIZATION OF THE CONFORMAL ALD T_IO_2 COATING

The three dimensional (3-D) atomic force microscopy (AFM) surface morphology analysis of the ALD TiO_2 coated mesh wires (Figure 2.5a) illustrated that the ALD TiO_2 coatings could keep the original surface morphology of individual copper mesh wire (Figures 2.5b, c). The root mean square (RMS) roughness increased from 1.2 nm on bare copper wire (Figure 2.5d) to 3.1 nm after the conformal ALD Al_2O_3 and TiO_2 depositions

in the flow mode (Figure 2.5e). In the static mode, the chemicals stayed in the reactor for a longer time and the chemical vapor deposition (CVD) occurred. Thus the RMS roughness increased to 13.2 nm (Figure 2.5f). Compared with reported surface modification techniques [9, 82], the conformal ALD TiO_2 coating showed great conformality and hence the surface area augmentation can be neglected. However, the wettability was improved significantly according to the contact angle measurement. The contact angle on a plain copper sheet, 51.2^o (Figure 2.5g), was reduced to 4.9^o (Figure 2.5h) on the ALD TiO_2 coatings, which indicated that the intrinsic water affinity of TiO_2 could significantly improve the hydrophilicity of individual copper mesh wire. This was different from the apparent superhydrophilicity induced by structure effect [9]. Moreover, the ALD TiO_2 coated two-layer meshes showed a reduced contact angle (Figure 2.5i), which was consistent with Wenzel′s law [25].

2.5 ENHANCED BOILING HEAT TRANSFER

Experimental study was conducted to characterize the pool boiling on the conformal ALD TiO_2 coated copper woven meshes. The bare two layer meshes, which performed better than the bare plain copper, were tested as the baseline. The test system was calibrated by the plain copper (Figure 2.6a) [13]. According to the nucleate boiling theory [83], the mesh wires have smaller nucleate cavities than the plain copper surface, thus the boiling incipience is delayed as show in Figure 2.6a. Since the copper meshes have a much larger surface areas than the plain copper surface, the CHF is promoted from 63.7 W/cm^2 on bare two layer meshes to 141.8 W/cm^2. Whereas, TiO_2 coated meshes were not superior in the low heat flux regime because on the more hydrophilic TiO_2 coated surfaces cavities were easier to be flooded and loose the activities for bubble

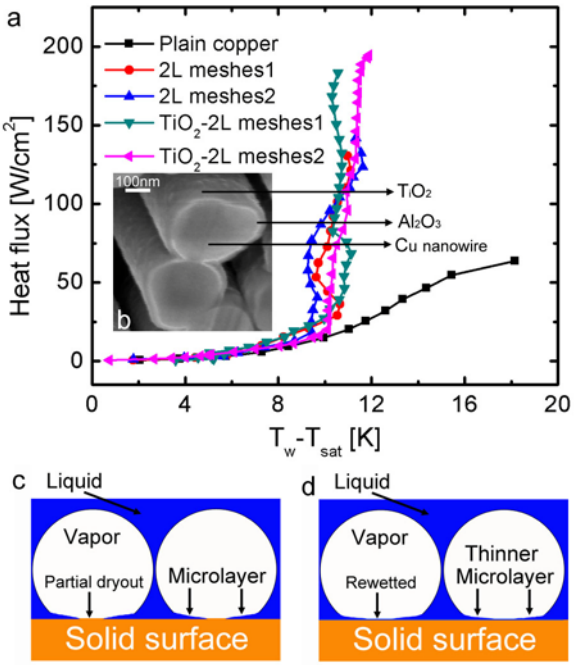

Figure 2.6 Heat transfer performances (a) ΔT-q" (ΔT = T_{wall} - T_{sat}) curves of the nano-thick TiO_2 coated two copper layer woven meshes. (b) Characterization of the ALD coating thickness. (c) Microlayer and partial dryout on the bare surface. (d) Heat transfer enhancement mechanism on the TiO_2 coated surface

growth. However, CHF was significantly increased from 141.8 W/cm^2 to 194.5 W/cm^2 on the conformal ALD coatings. The ALD TiO_2 coating with the surface roughness of 13.2 nm reached the CHF of 183.3 W/cm^2, which was slightly increased to 194.5 W/cm^2 when the surface roughness decreased to 3.1 nm. This indicates the augmented nanoscale surface rougheness could not increase the CHF. Therefore, the CHF enhancement results from the improved interfacial wettability.

To quantitatively characterize the thickness of TiO_2 coatings, copper nanowires were deposited in the same working conditions and was cut by focused ion beam (FIB) (Figure 2.6b). The number of deposition cycles of Al_2O_3 was 50 and the typical growth rate was 0.12 nm/cycle. Subsequently, TiO_2 was coated for 320 cycles with the growth rate of 0.05 nm/cycle. Therefore, the total film thickness was approximately 22 nm (6 nm

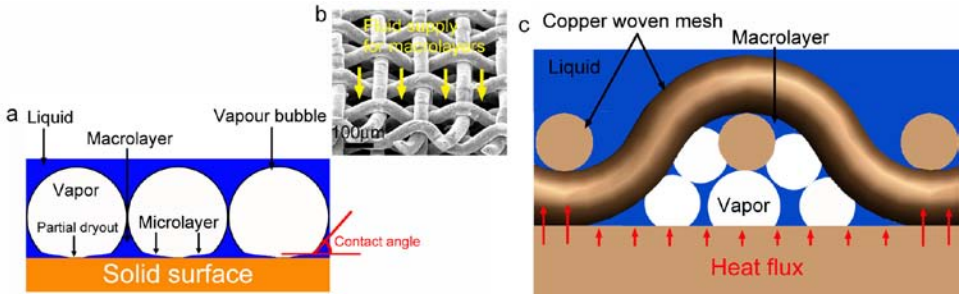

Figure 2.7 Heat transfer mechanisms. (a) Macrolayer & microlayer for nucleate boiling. (b) Fluid supply for the macrolayers in porous structures. (c) Macrolayer formation in two layer meshes.

ALD Al_2O_3 and 16 nm for ALD TiO_2). This was directly shown in Figure 2.6b.

The CHF enhancement mechanism resulted primarily from the improved wettability, instead of the surface roughness as shown in Figures 2.6c and d. The temperature distribution inside the bubble was measured by Gerardi [84]. It indicated that the thin film evaporation of microlayer was the primary phase change mechanism and the center of the bubble might be partially dry (Fig. 2.6c). The superwetting property of the TiO_2 coating was able to rewet the dryout areas inside the bubbles and reduced the thickness of the microlayer. Thus, in the high heat flux regime, the thin film evaporation inside the bubble was dramatically enhanced and the superheat was significantly reduced. The superwetting property of the TiO_2 coating was superior to improve the local wettability to form the microlayer liquid film, which could maintain the wetting of sufficient areas on the mesh wires for evaporative heat transfer and hence delayed local dryout.

In previous investigations, structured or hierarchical surfaces were able to increase the CHF due to the augmented surface roughness [10, 20, 23, 85]. Improved wettabilities have been demonstrated to be able to promote the CHF in terms of single Pt wire [30]. The CHF is sensitive to the surface wettability in the macrolayer dryout theory

[86] and the hot/dry spot theory [87], while the hydrodynamic instability theory excludes the impact of surface wettability on CHF [88]. According to the macrolayer dryout theory (Figure 2.7a) [86], CHF is limited by the fluid supply to form the macrolayers trapped under the vapor bubbles [89]. On a Pt wire or plain surface, the formation of the macrolayer is primarily governed by the surface wettability. However, in microporous meshes, it is primarily determined by capillary flow and liquid spreading as the liquid needs to go through the microscale pores and enter into the bottom surface (Figure 2.7b). Furthermore, the bubble growth and collapse result in local oscillation and mixing, which may significantly affect the local liquid supply. Although the capillarity was enhanced due to the improved hydrophilicity, it could not govern the formation of the macrolayers because the expansion force induced by bubble growth and vacuum induced by bubble collapse were the dominated forces. The fluid oscillations governed the liquid supply to form the macrolayers inside the porous structures. The conformal ALD TiO_2 coating maintained the surface morphologies and cavities. Hence, the bubble growth and collapse motions are similar on the coated and non-coated surfaces. In the high heat flux regime, the liquid motions were governed by the high frequency bubble growth and collapse oscillations (Figure 2.7c). Therefore, the superwetting property can not contribute to the liquid supply of macrolayers. Consequently, the improved wettability induced by the nano-thick conformal ALD TiO_2 coating can significantly enhance the CHF.

CHAPTER 3

CARBON NANOTUBE ENABLED HYDROPHOBIC-HYDROPHILIC COMPOSITE INTERFACES TO ENHANCE NUCLEATE BOILING

Ideal hydrophobic-hydrophilic composite cavities are highly desired to enhance nucleate boiling. However, it is challenging and costly to fabricate this type of cavities by conventional micro/nano fabrication techniques. In this study, a hydrophobic-hydrophilic composite interface was synthesized from functionalized multiwall carbon nanotubes by introducing hydrophilic functional groups on the pristine multiwall carbon nanotubes. This type of carbon nanotube enabled hydrophobic-hydrophilic composite interface was systematically characterized. Ideal cavities created by the new interfaces were experimentally demontrated to be the primary reason resulting in substantially enhanced nucleate boiling.

Nucleate boiling is widely used in a variety of heat transfer and chemical reaction applications. The state-of-the-art techniques in enhancing nucleate boiling have focused on using micro/nanoscale structures [9] as well as applying hydrophilic coatings [30]. Guided by nucleate boiling theory [90] and the most recent study [91], ideal boiling surfaces should be hydrophilic to delay flimwise tranistion and contain hydrophobic cavities to trap gases or vapor by taking advantages of both of the hydrophilic and hydrophobic properties [91].

3.1 INTRODUCTION OF NUCLEATE BOILING

Enhanced transport phenomena have been reported on partially hydrophobic and

partially hydrophilic interfaces [92-93]. For examples, Daniel [94] reported that the interfaces with hydrophobic-hydrophilic composite wettabilities were able to accelerate drop motion [95], and thus significantly enhance the condensation heat transfer. Miljkovic [96] observed that partially wetting droplets exhibited a much higher growth rate than suspended droplets during dropwise condensation. Martines [93] confirmed that a forest of hydrophilic/hydrophobic slender pillars was shown to be the most effective superwettable/water-repellent configuration. Cottin-Bizonne [97] found that partial dewetting on a composite interface was superior in producing a "water repellent" effect and thus in reducing the surface friction. In addition, a superhydrophobic and sticky interface was found to be exceptional in transporting small volumes of liquids without loss [98-99]. Enhanced nucleate boiling was experimentally demonstrated on micro-fabricated techniques [100]. However, the enhanced nucleate boiling on CNT-enabled hydrophobic hydrophilic interfaces was not reported. Additionally, the conventional micro/nano-fabricated hydrophobic-hydrophilic composite interfaces [93, 100-101] are usually costly and challenging to tune the wettability in a controlled manner.

In this study, hydrophobic-hydrophilic composite interfaces were synthesized from FMWCNTs by introducing hydrophilic functional groups on the pristine MWCNT surfaces. The ideal boiling surfaces created by the CNT enabled hydrophobic-hydrophilic composite interfaces were experimentally demonstrated to effectively enhance nucleate boiling.

3.2 SYNTHESIS OF HYDROPHOBIC-HYDROPHILIC COMPOSITE INTERFACES

CNTs [102] with defects, which were generally regarded to have mechanical [103], electrical [104] and thermal disadvantages [105], were shown to exhibit intriguing

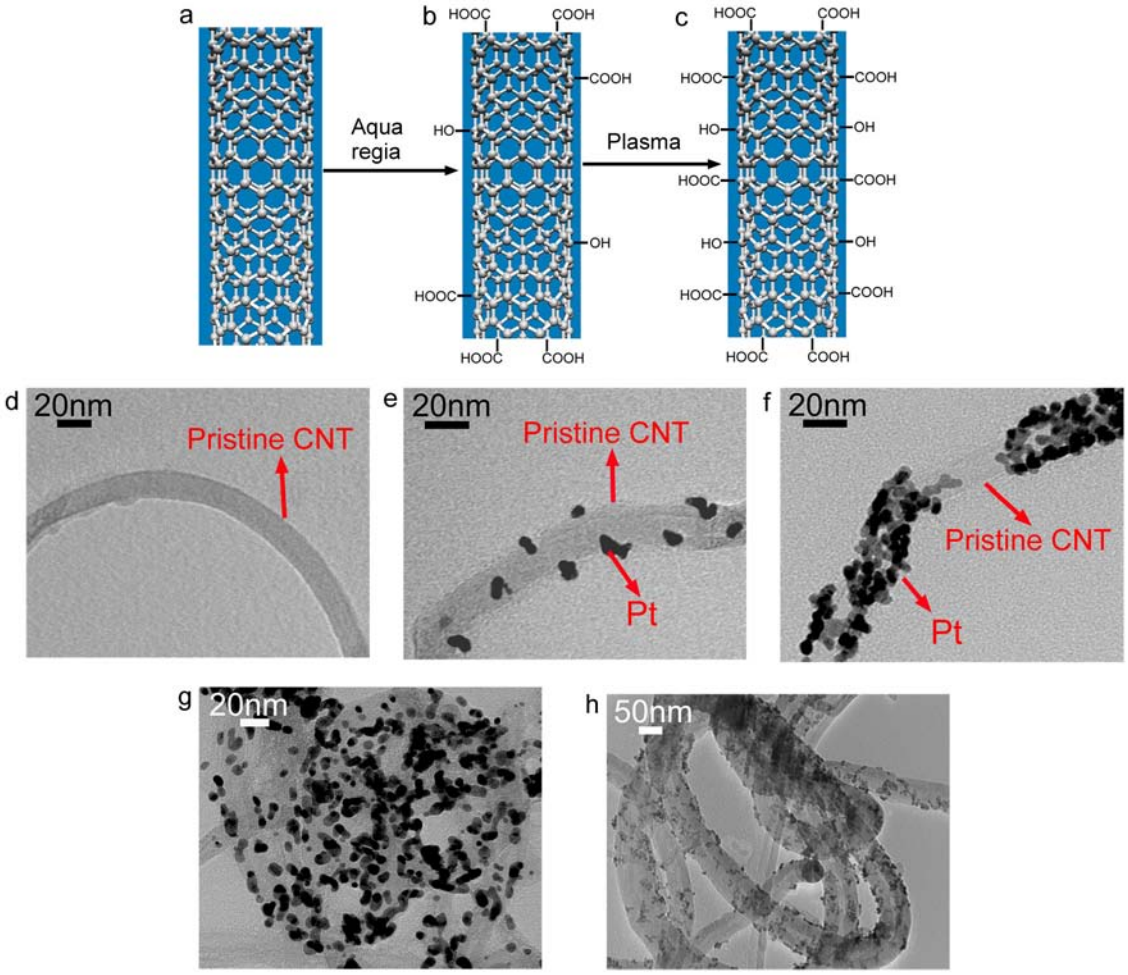

Figure 3.1 Synthesis and characterization of the hydrophobic-hydrophilic FMWCNTs. (a) Pristine MWCNTs. (b) Aqua regia oxidized MWCNTs. (c) Plasma treated FMWCNTs. (d) Pristine MWCNT without defect. (e) Defects on slightly functionalized FMWCNT indicated by Pt ions. (f) Defects on deeply functionalized FMWCNT indicated by Pt ions. (g) Hydrophobic and hydrophilic areas on FMWCNT coated interfaces. (h) Interconnected cavities formed by partially hydrophobic and partially hydrophilic FMWCNTs.

properties for many emerging applications such as nano-sensors [106], super conductors [107], catalysts [108] and field effect transistors [109]. In this study, the hydrophobic-hydrophilic composite interfaces were synthesized by partially oxidizing pristine MWCNT surfaces to form hydrophilic carboxylic and hydroxylic functional groups on the defect sites of MWCNTs [108]. The commercially available MWCNTs were initially

oxidized in aqua regia solutions (Figures 3.1a and b). Then, 5 mg of synthesized FMWCNTs with 20 mg of 5% Nafion solution were ultrasonically dispersed in the isopropyl alcohol to form "inks". Greater dispersions of FMWCNTs were obtained by ultrasonically mixing with isopropyl alcohol, and adding amphiphilic Nafion [110]. The well-dispersed FMWCNT "inks" were deposited on a copper substrate by an ultrasonic spray coater. Oxygen plasma was used to further functionalize the FMWCNT coated samples, which added more hydrophilic functional groups [111] (Figure 3.1c). The extent of functionalization can be conveniently tuned by varying the reaction time and the oxygen flow rate. Here, Nafion was also used to strengthen the bonding of the FMWCNT coatings with the substrate, introduce the additional hydrophobic functional groups (-CF_2-) and hydrophilic sulfuric acid groups (-SO_3H) and improve the dispersion.

In this study, the distribution and concentration of hydrophilic groups were approximately indicated by tracer particles (Figures 3.1d and e) due to the challenge in directly visualizing the hydrophobic-hydrophilic network on FMWCNTs. Positively charged platinum ions (Pt^{4+}) from chloroplatinic acid (H_2PtCl_6) were used to locate the functional groups on the FMWCNT wires and bundles since the reduced platinum particles tend to nucleate on the defects of FMWCNTs [108]. Since the functional groups grow preferentially in the defect sites [112]. Pt loaded areas were taken favorably as functionalized regions.

3.3 CONTACT ANGLE MEASUREMENT

The hydrophilic functional groups grown on the defected areas are at the nanoscale. Thus, it is challenging to quantify the ratio of the hydrophilic surface areas in the porous coatings. In this study, the macroscopic contact angle measurements were

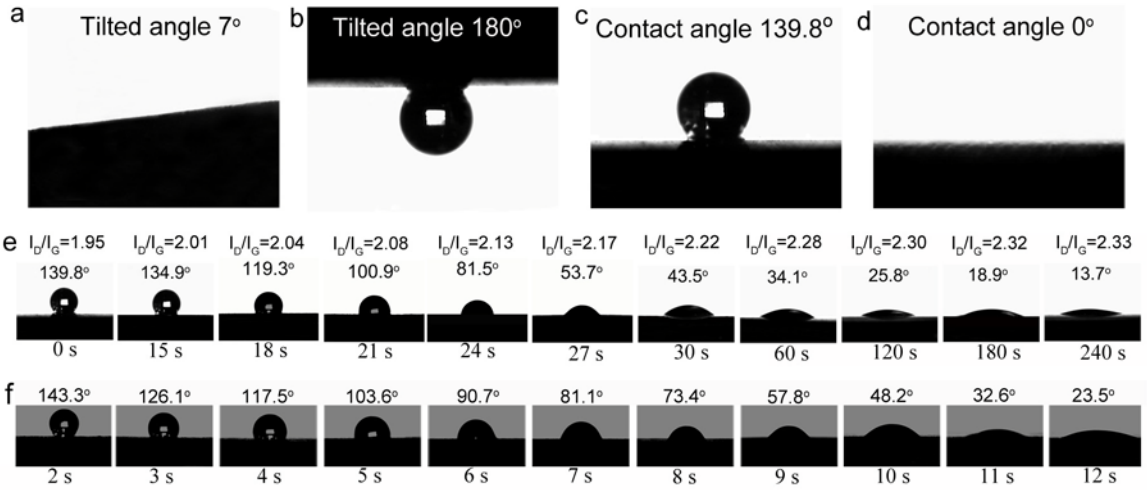

Figure 3.2 Characterization of the wettability of hydrophobic-hydrophilic FMWCNTs interfaces. (a) On pristine CNT coated interface with a tilt angle of 7^o. (b) On FMWCNT coated interface with a tilt angle of 180^o. (c) On dry FMWCNT coated interface. (d) On wet FMWCNT coated interface. (e) Contact angle as a function of Raman I_D/I_G ratio and plasma treatment time (on FMWCNT coated flat copper surface). (f) Contact angle as a function of plasma treatment time on pristine MWCNT coated flat copper surface.

employed to characterize the wettability of the hydrophilic-hydrophobic composite interfaces. The pristine MWCNT coatings are hydrophobic [113] and non-adhesive (Figure 3.2a). The straw-like pristine MWCNT coated interface is superhydrophobic [114] and is non-wettable even totally immersed in water. In contrast, the dry FMWCNT coatings on a flat copper substrate were apparently hydrophobic, but adhesive, which was evidenced by a water droplet adhering to the coatings with a tilt angle of 180^o (Figures 3.2b and c). Although having almost the same surface morphologies as the non-adhesive pristine MWCNT coatings, the FMWCNT coatings show stickiness, which is believed to be induced by the hydrophilic functional groups on the defect areas (Figure 3.1e). This indicates that the Van der Waals [99] and/or the capillary force between the nanostructured interfaces and water are introduced by the partial wetting [115]. Therefore, transitions between the Cassie-Baxter and Wenzel [25] states can be induced by enhancing stickiness [116]. When the wetting behavior changes from the Cassie mode to

the Wenzel mode, the liquid droplet can at least partially fill the cavities of the rough substrates with a reduced apparent contact angle [115]. The characterization of sticky property clearly indicated the effect of partial hydrophilicity on surface wettabilities (Figures 3.1d and e). FMWCNT interfaces were shown to be wettable (Figure 3.2d). The reason could be the capillary flow induced at the solid-liquid-gas interfaces. As a result, the majority of pores can be filled with water, causing the interfaces to lose its water-repellent properties [116] as shown in Figure 3.2d. These observations are consistent with the hydrophobic-hydrophilic wettability of FMWCNTs as shown in the TEM images (Figures 3.1g, h). In contrast to the non-wettable MWCNT coating, this wettable FMWCNT coated interface can improve the local liquid supply during the boiling process as the whole interfaces are immersed in the liquids.

Regular FMWCNT wires or bundles, i.e., those only treated by aqua regia, contain fewer hydrophilic functional groups (Figure 3.1e) than oxygen plasma treated FMWCNTs (Figure 3.1f). This observation implies the superior tunability of hydrophobic-hydrophilic composite wettability enabled by the enhanced FMWCNTs. In this study, the relative hydrophilicity of individual FMWCNT wires and coatings was found to be conveniently tuned by controlling the plasma treatment time. Figure 3.2e quantitatively shows that the apparent contact angle of FMWCNT interfaces decreased with increasing plasma treatment time at a given oxygen flow rate. Raman analysis showed that more defects were introduced by longer plasma treatment time [117], e.g. with more C=O, O-C=O and O-H groups [111], which were indicated by an increasing I_D/I_G ratio [117] (refer to the Supplement Information). To better understand the effects of plasma treatment on the wetting property of CNTs, variation of contact angle on

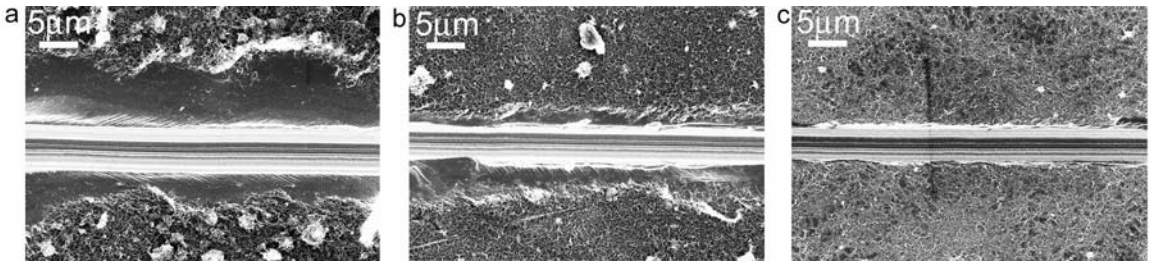

Figure 3.3 Characterization of the bonding. (a) Scratches on the pure MWCNT coated interface (b) Scratches on the FMWCNT coated interface (c) Scratches on the FMWCNT-Nafion mixture coated interface.

pristine MWCNTs coatings without Nafion was studied. Longer plasma treatment time resulted in a higher hydrophilicity, which was indicated by the reduced contact angle (Figure 3.2f). It was found that the required time of plasma treatment was much less than that of FMWCNTs coatings with Nafion. This could be a result of protection effects from Nafion wrapping.

3.4 CHARACTERIZATION OF THE BONDING FORCES

Microscratch tests were carried out on a CETR microtribometer to examine the bonding strength of the FMWCNT coatings on copper substrates, as well as the interactions between individual FMWCNT wires (Figure 3.3). Pristine CNTs peeled off the copper substrate near the scratch edge (Figure 3.3a), which indicated hydrophobic pristine CNTs were not bonding with the copper substrate. However, the bonding between the FMWCNT coating and the copper substrate was improved by inducing hydrophilic functional groups (Figure 3.3b). The reason could be the superhydrophicility of the functional groups that enhanced the bonding to the hydrophilic copper substrates. Additionally, amphiphilic Nafion served as a gluing media to further strengthen the bonding after thermally curing, which was indicated by the residual FMWCNTs wrapped by polymer near the scratch edge (Figure 3.3c). Superhydrophobic CNTs have poor

bonding forces with hydrophilic copper substrates as the hydrophobic interaction is a type of enthalpic or entropic forces [118], which are weak Van der Waal based forces acting through limited contacts. The microscratch tests showed that the bonding was greatly strengthened by introducing hydrophilic functional groups and amphiphilic Nafion. Moreover, further enhancement of bonding can be achieved by thermally curing the coating at approximately 130 ^{o}C, above the glass transition temperature of Nafion for five minutes. This occurred because the polymer chain inter-diffuses, allowing a greater degree of interlocking and Van der Waals interactions.

3.5 BOILING EXPERIMENT ON THE HYDROPHOBIC-HYDROPHILIC SURFACES

Ideal boiling surfaces to achieve high HTC and CHF should simultaneously have a combination of features: high active nucleating site density, optimized cavities favorable for bubble growth and departure and in reducing superheat, minimized flow resistance to improve liquid supply, and an evenly distributed liquid film to induce and promote thin film evaporation. The straw-like FMWCNT coatings, which can randomly form a large number of interconnected pores or cavities (Figure 3.1h) with partially hydrophobic and partially hydrophilic areas (Figure 3.1g), could create ideal nucleate boiling surfaces.

In general, there are four typical types of boiling surfaces as schematically shown in Figure 4a. The type I boiling surfaces with superhydrophilic cavities, can substantially reduce superheat, delay the transition boiling, and hence enhance HTC as guided by the nucleate boiling theory [90], but they greatly suffered from flooding. Additionally, the type II boiling surfaces with superhydrophobic cavities, can accelerate bubble departure processes, but result in extremely high superheat. According to the most recent study [91],

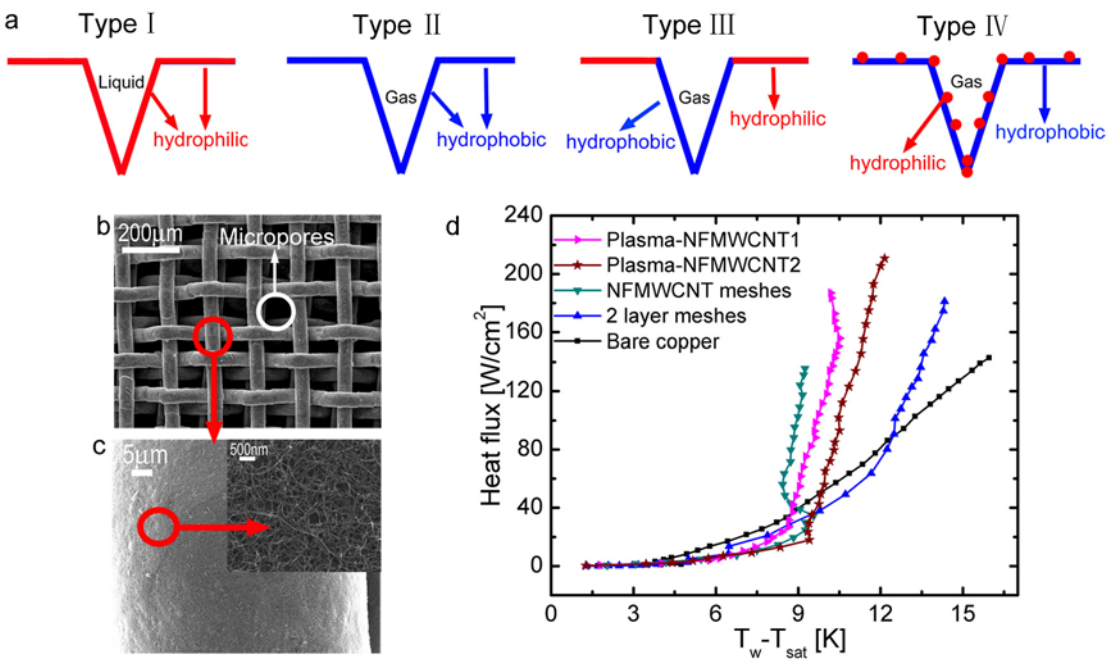

Figure 3.4 Cavity types and characterization of nucleate boiling on supernucleating interfaces. (a) Four types of cavities for nucleate boiling. (b) Two-layer copper meshes sintered on smooth copper. (c) FMWCNTs coated mesh wires. (d) Pool boiling curves, where FMWCNT meshes denote "regular FMWCNT coated two-layer meshes″; Plasma-FMWCNT1 – "intermediately functionalized FMWCNT coated two-layer meshes (8 min plasma treatment)″; and Plasma-FMWCNT2 – "deeply functionalized FMWCNTs coated two-layer meshes (15 minutes plasma treatment)″.

the type III boiling surfaces with superhydrophobic-superhydrophilic surfaces are ideal for nucleate boiling by taking advantages of both hydrophilic and hydrophobic properties. However, it is challenging to fabricate type III boiling surfaces by traditional micro/nano fabrication techniques [100]. In this study, the type IV boiling surfaces (right in Figure 3.4a), which were created by the novel FMWCNTs, intrinsically include a large amount of submicro/nanoscale interconnected cavities with unique hydrophobic- hydrophilic composite wettability.

An experimental pool boiling study was performed to evaluate type IV boiling surfaces. In order to take full advantages of the supernucleating interfaces, the mixture of Nafion and FMWCNT (NFMWCNT) was coated on two-layer copper mesh screens to

form hierarchical structures. The hierarchical structures contained microscale pores (Figure 3.4b) and nanopores (Figure 3.4c) created by copper meshes and NFMWCNT coatings, respectively. Microscale pores were designed to reduce the liquid flow resistance. In total, five samples were experimentally studied (refer to the Supplement Information). Flat copper surfaces were used to calibrate the test apparatus, and two-layer sintered copper woven mesh screens were used as the baseline. Three two-layer mesh screens coated with approximately 800 nm thick NFMWCNTs were tested to determine the effects of the hydrophobic-hydrophilic composite interfaces on nucleate boiling.

From the five boiling curves presented in Figure 3.4d, the overall nucleate boiling HTC on NFMWCNT coatings with and without oxygen plasma treatments has been significantly enhanced, compared to the bare two-layer copper mesh screens. However, such an enhancement was found to decrease with an increasing amount of hydrophilic groups. Specifically, for a given heat flux 135 W/cm^2, the HTC on the regular NFMWCNT coated sample was dramatically enhanced by 46.5%, but the enhancement was reduced to approximately 32.7% and 20.8% on two plasma treated samples, i.e., plasma-NFMWCNT 1 and 2, respectively. Additionally, CHF was significantly reduced from 181.1 to 135.5 W/cm^2 on the regular NFMWCNT coated sample, because the amount of functional groups on the regular NFMWCNTs was limited and degraded the local wettability and, hence, the liquid supply, as indicated in Figure 3.1e. This observation is consistent with two oxygen plasma-treated NFMWCNTs coatings, where CHFs were found to increase from 181.1 W/cm^2 to 187.2 W/cm^2 and 210.5 W/cm^2, respectively. It was experimentally validated that more hydrophilic functional groups lead to the improvement of local liquid supply and, therefore, the delay of transition

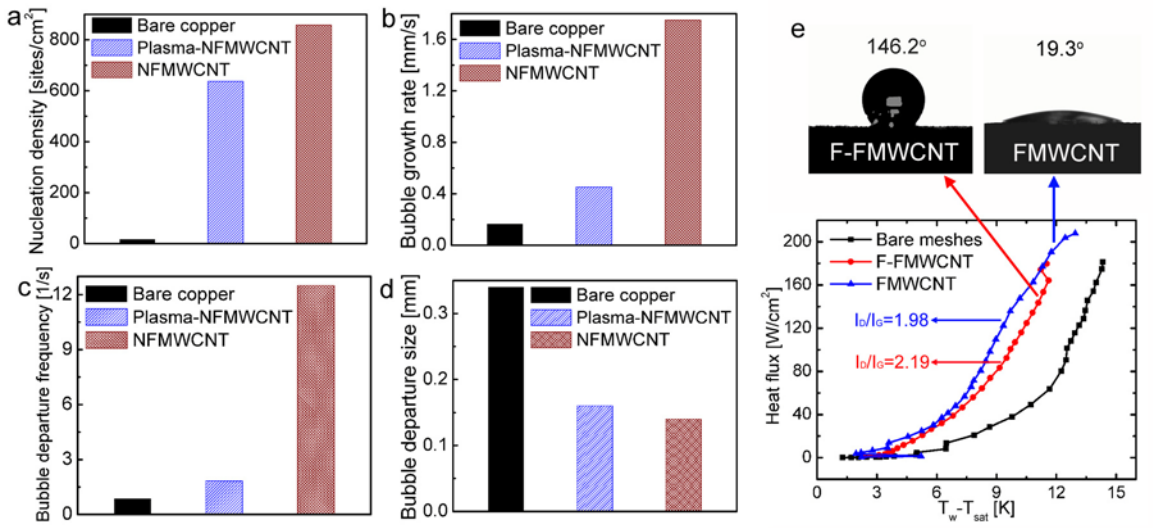

Figure 3.5 Bubble dynamics. (a) Comparison of the nucleation site density. (b) Comparison of the bubble growth rate. (c) Comparison of the bubble departure frequency. (d) Comparison of the average bubble departure size. (e) The effects of hydrophilicity and defect density on boiling heat transfer.

boiling. The onset of nucleate boiling (Figure 3.4d) on regular NFMWCNTs or plasma-treated NFMWCNTs was significantly delayed compared with the bare meshes. That could be caused by the reduced cavity opening size formed by NFMWCNTs, as indicated by nucleate boiling theory [90].

3.6 ENHANCEMENT MECHANISM

To mechanistically understand the enhanced nucleate boiling on NFMWCNT coatings, a visualization study was performed to understand the bubble dynamics on three flat substrates: bare copper, NFMWCNT coated copper, and oxygen plasma treated NFMWCNT coated copper at a given super heat, $\Delta T = 9 \pm 0.5\ ^{o}C$. The dramatic enhancement results of the NFMWCNTs were shown in the significant increase of active nucleation site density, bubble growth rate, and bubble departure frequency with the hydrophobic-hydrophilic composite cavities (Figure 3.5). The active nucleation site density on NFMWCNT coatings with and without oxygen plasma treatments was found

to be at least one order of magnitude higher than that on the bare copper substrate. The primary reasons could be in two-folds during the entire nucleate boiling process. The first, the total surface area was significantly augmented becuase of the NFWMCNT coatings. The second, the active nucleation site density was dramatically enhanced because of the prevention of cavities (formed by NFWMCNTs) from flooding due to their hydrophobic property. The highest nucleation site density was on the regular NFMWCNT coatings (Figure 3.5a). Bubble growth rate on the NFMWCNT coatings with and without oxygen plasma treatments (Figure 3.5b) was also significantly higher than that on the bare copper surface, which indicated that the evaporation in the microlayer was primarily enhanced by the hydrophilic groups. However, having a fewer number of the less hydrophilic groups resulted in a higher evaporating rate on the microlayer according to the visualization study. This could be caused by the decreased local drag resulting from fewer hydrophilic groups, which would enhance the water supply to the nanopores or cavities underneath. Additionally, bubble departure frequency from NFMWCNT coatings was higher (Figure 3.5c) and the average bubble departure diameter was smaller (Figure 3.5d) compared with those on the bare copper interface. The reason can be a combined effect of the reduced anchoring surface tension force on hydrophobic-hydrophilic interfaces and the increased inertia force resulting from the bubble growth due to the enhanced evaporation in the microlayer.

The slightly functionalized NFMWCNT interfaces performed even better in terms of bubble generation, growth and departure than the oxygen plasma treated NFMWCNT interfaces. This observation confirms that hydrophobic cavities are superior in promoting the bubble departure processes, and hence, in enhancing the HTC, while hydrophilic

surfaces are best for improving the local wettability and therefore delaying the transition boiling, i.e., enhancing CHF. This study experimentally demonstrates that the enhancements of HTC and CHF can be achieved by inducing hydrophobic-hydrophilic composite wettability, which can be tuned by varying the concentration of hydrophilic functional groups.

To further distinguish the effects of hydrophilicity and defect density on boiling heat transfer enhancement, FMWCNT coatings with and without fluoridations were studied. FMWCNT was treated by fluorine to achieve hydrophobic fluorinated FMWCNT (F-FMWCNT), where more defect areas were introduced and a large amount of hydrophobic C_2F functional groups were created [119-120]. The completely hydrophobic F-FMWCNT and partially hydrophilic FMWCNT were coated on the flat copper substrates without any additives. The contact angles were measured at 146.2^o and 19.3^o, respectively (Figure 3.5e). Boiling heat transfer rate on the F-FMWCNT coatings was found to be lower than that on the FMWCNT coatings. Additionally, the Raman spectroscopy examines that the F-FMWCNT has a higher defect density than the FMWCNT (indicated by the higher I_D/I_G ratio as shown in Figure 3.5e). Therefore, the enhancement of boiling heat transfer is primarily caused by the introduced hydrophilicity instead of the defect density in the CNT enabled hydrophobic-hydrophilic interfaces.

In summary, interfaces with hydrophobic-hydrophilic composite wettabilities were synthesized from the functionalized MWCNTs by partially oxidizing pristine MWCNT surfaces to form hydrophilic carboxylic and hydroxylic functional groups on the defect sites of MWCNTs. Amphiphilic Nafion was added to strengthen the bonding of the FMWCNT coatings and to introduce additional hydrophobic functional groups (-

CF_2-) and hydrophilic sulfuric acid groups (-SO_3H). The distribution and concentration of hydrophilic groups were approximately indicated by platinum nano-particles. The apparent contact angle of the interface was shown to be conveniently tuned in a large range by varying the concentration of the intrinsically hydrophilic functional groups. The present nano-engineered interface, which composed of numerous submicro/nanoscale interconnected cavities with partially hydrophobic and partially hydrophilic wettability, was experimentally demonstrated to be superior to enhance nucleate boiling. This is because the hydrophobic-hydrophilic interfaces effectively enhance nucleation density, bubble growth rate and bubble departure frequency, and thus considerably improve nucleate boiling. Hydrophobic F-FMWCNTs with higher defect densities were shown to perform worse than the hydrophilic FMWCNTs in boiling heat transfer. This indicated that the nucleate boiling was primarily enhanced by the introduced hydrophilicity, instead of the defect density in the CNT enabled hydrophobic-hydrophilic interfaces. Moreover, this nano-engineered interface can potentially be used to enhance transport phenomena at micro/nano scale, such as transporting liquid without loss [99], reducing friction [97], and manipulating droplet movement [94].

CHAPTER 4

MICROMEMBRANE-ENHANCED CAPILLARY EVAPORATION

Micromembrane-enhanced evaporating surfaces were developed to enhance capillary evaporation *HTC* and *CHF*. Micromembranes made of sintered single-layer copper mesh screen were diffusion bonded on microchannels to effectively promote capillary pressure and reduce flow resistance. Compared with mono-porous evaporating surfaces such as microchannels and copper woven mesh laminates in the same thickness under the similar working conditions, *CHF* was substantially increased by 83% and 198%, respectively, because of the separation of the capillary pressure generation and fluid transport process that was enabled by the micromembrane. The major features such as *"M"*-shaped capillary evaporation heat transfer curves and the associated heat transfer regions were identified. Oscillating flows induced by the bubble growth and collapse as well as the capillary flows induced by the receding menisci were observed and believed to play imperative roles in enhancing the heat transfer by inducing advections and improving evaporation and nucleate boiling.

4.1 INTRODUCTION OF CAPILLARY EVAPORATION

Capillary evaporation [31] is one of the most efficient heat transfer modes and has been widely used in heat exchangers [32] and heat pipes [33-35]. Evaporators with high *HTC* and *CHF* are highly desirable for compact heat exchangers for high heat flux applications [36-37]. Most of porous coatings used in enhancing capillary evaporation

are usually mono-porous structures [39]. For example, sintered particles and powders were developed to substantially enhance thin film evaporation *HTC* [39-40]. The effects of porosity, wick thickness and other factors on the optimal design of the wicking structures were also examined [39-40]. Copper woven mesh laminates [41-44] were extensively studied to enhance the capillary evaporation *HTC* due to the augmented surface areas and increased capillary forces. However, the flow resistances in these microscale mono-porous structures remain high, resulting in low *CHFs* due to the liquid supply crisis. Micro-grooves [45-46] or channels [47] were superior for liquid supply because of the attributed low flow resistance, but the capillary forces induced by the disjoining pressure differences in grooves [46] were still too low to reach high *CHFs*. This brief review shows that both the microscale mono-porous structures (such as sintered meshes or particles/powders) and micro-grooves or channels cannot meet the needs of high heat flux applications. To solve this dilemma, various types of bi-porous surfaces were proposed and developed [35, 48-52]. Semenic et al. [49, 51] found that biporous surface of sintered powders performed better than the mono-porous copper wicks because the working fluid can be supplied to the hot spots through micropores inside the clusters even though the voids were filled with vapor. Cao et al. [53] reported that when a mono-dispersed wick was replaced by bi-dispersed wicks with the same small pore diameter, both *HTC* and *CHF* were increased significantly. Cai et al. [36] studied the heat transfer performance on the carbon nanotube bi-porous structures, which consisted of carbon nanotube (*CNT*) array separated by microchannels. The nanoscale pores in the *CNT* bi-porous structure provided ultrahigh capillary pressure and augmented surface areas, which significantly reduced the menisci radii and increased thin-film

evaporation area and evaporation efficiency. Ćoso et al. [54] examined a type of bi-porous media consisting of microscale pin fins periodically separated by microchannels to simultaneously increase the heat dissipation capacity as well as the *HTC* of the evaporator wick. Some of the bi-porous wicks have also been integrated in heat pipes [50, 55-57] to decrease the thermal resistance and increase working heat fluxes. Heat pipe performance was found to be greatly enhanced by applying modulated wick because of enhanced axial capillary liquid flows and extra evaporation surface area resulting from the cross-sectional area [35]. In these reported bi-porous structures, the main fluid passages were still through the micro or nanoscale mono-porous structures (such as microscale powders or *CNTs*). As a result, the overall liquid flow resistances still remain high.

On the other hand, the oscillating flow significantly increases *HTC* and *CHF* in closed mini/micro-channels as can be found in oscillating heat pipes [47, 121]. However, the oscillating capillary evaporation in unconfined or open microchannels was not reported.

The objective of this study is to develop a new type of micromembrane-enhanced evaporating surfaces that are capable of both generating high capillary pressure and managing flow resistances. The effects on capillary evaporation were systematically examined. These effects include the separation of liquid supply and capillarity generation as well as the induced oscillating flows in unconfined micromembrane-enhanced evaporating surfaces.

4.2 DESIGN OF MICROMEMBRANE-ENHANCED EVAPORATING SURFACES

During the capillary evaporation, the counter interactions of flow resistance and

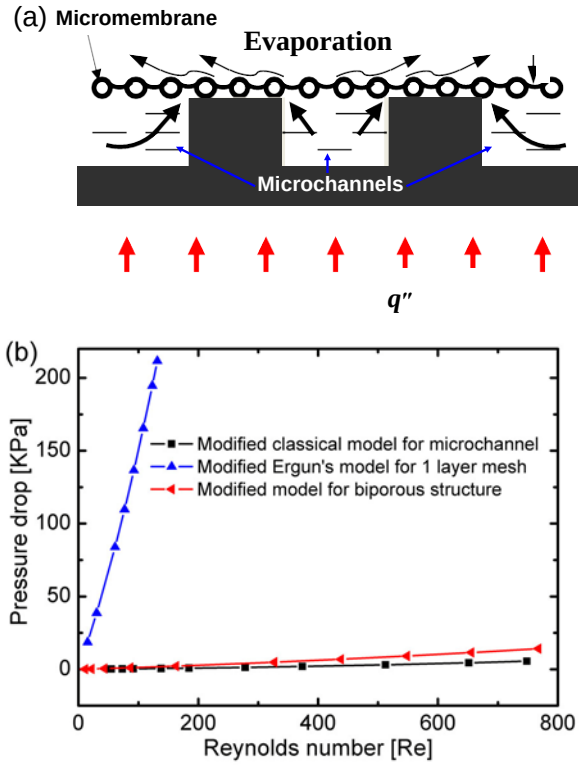

Figure 4.1 (a) Design of micromembrane-enhanced evaporating surfaces. (b) Comparisons of flow resistances between meshes, microchannels and the micromembrane-enhanced evaporating surfaces.

capillary force determine the overall liquid supply and thus, the *CHF*. Fine copper woven meshes with microscale pore size can generate high capillary pressure, but the associated flow resistance through the in-plane direction was significantly high. Micro-grooves [45-46] or channels [47] were superior for liquid supply because of the low flow resistance, but with limited capillarity [46]. The combination of the advantages of single layer meshes and microchannels could lead to a new type of capillary evaporating surfaces with high capillary pressure and low flow resistance, which would consequently result in much higher *CHF* than each individual (Figure 4.1a). The membrane with microscale pores was developed to generate high capillary pressure and augment heat transfer area. Smooth microchannels were designed as the primary fluid passages to reduce flow

resistance. Moreover, the micromembranes would greatly enhance thin film evaporation because of the augmented area and high resistance to surface flooding using capillarity.

A theoretical model was developed to verify the design. Due to the unavailability of two-phase models for single layer mesh screens, the single-phase flow resistances through microchannels and single layer mesh (in-plane direction) were estimated. A modified Ergun equation for the porous media [122] was employed in this study to estimate the flow resistance through sintered woven meshes.

$$\frac{\Delta p}{L} = \beta \frac{\mu(1-\varepsilon)^2 \upsilon_s}{D_p{}^2 \varepsilon^3} + \gamma \frac{1-\varepsilon}{\varepsilon^3} \frac{\rho \upsilon_s{}^2}{D_p}$$

(1) where, Δp is pressure drop; L is the length along the macroscopic pressure gradient in porous media; v_s is the average velocity estimated from $v_s = Q/A$ (Q is flow rate through a cross-sectional area A); μ is the absolute viscosity offluids; ε is the volumetric porosity; D_p is the equivalent spherical diameter of porous media; and ρ is the fluid density. Here, the β and γ vary with different porous media [44] and were modified for the one layer woven screen meshes as β = 15940 and γ = 12 according to this experimental study using the method in Ref. 106. The equivalent diameter of particles for a mesh is defined as, $D_p = 6/S_v$ [44], where, S_v is defined as the surface area per unit volume of solid phase. The volumetric porosity of the mesh [123] is given by

$$\varepsilon = 1 - \frac{\pi d M \sqrt{1 + M^2 d^2}}{4 C_f} \tag{2}$$

where, d is the diameter of the mesh; M is mesh number; C_f is compression factor and equal to 0.9 for two-layer meshes.

The single-phase flow resistance through a smooth, rectangular channel in the laminar flow regime can be estimated by Darcy-Weisbach equation [124]:

$$\Delta p = \frac{1}{2}\rho v^2 \frac{L_0}{D_h} f, \ \ where \ \ f \cdot \mathrm{Re} = 57 \tag{3}$$

where, Δp is the pressure drop through the channel; v is fluid velocity; L_0 is channel length; D_h is hydrodynamic diameter; f is the Darcy friction factor and Re is Reynolds number.

As shown in Figure 4.1b, the magnitude of flow resistance in the single layer mesh was more than four orders higher than that through the microchannels. Flow resistance on the micromembrane-enhanced evaporating surfaces was estimated to be only a small fraction of that in the single layer meshes at the same Reynolds number and slightly higher than the in microchannels as shown in Figure 4.1b.

Equally important, capillary force generated from the micromembrane can be significantly increased and was estimated to be approximately two times higher than that generated on the microchannels by comparing the minimum meniscus radius [125] when the working fluid and substrate materials are identical. This indicates that the membrane-enhanced evaporating surfaces developed in this study could achieve high *CHF* with significantly enhanced *HTC* by increasing the capillary forces, augmenting the surface areas and reducing the flow resistance.

4.3 EXPERIMENTAL APPARATUS AND DATA REDUCTION

Fine sintered copper woven meshes were employed as the primary evaporating membranes because of their superior thermal conductivity, high permeability and large surface areas [13, 123, 126]. Copper woven meshes with mesh number of 1509 m^{-1} (145 $inch^{-1}$) and wire diameter of 56 μm (made by Belleville Wire Cloth, as shown in Figure 4.2a, b and c) were attached on the microchannels by a diffusion bonding technique [13, 127] to minimize the contact thermal resistance [123]. Samples as shown in Figure 4.2a

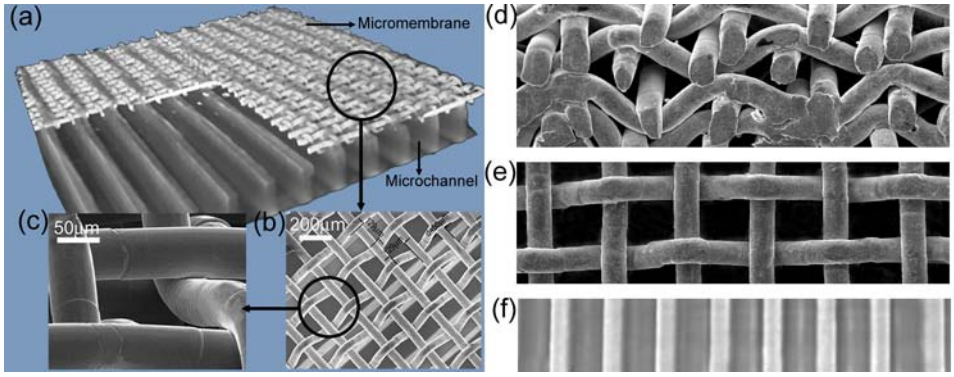

Figure 4.2 The micromembrane-enhanced evaporating surfaces developed in this study. (a) Three dimensional (3D) Micro-XCT image of the micromembrane-enhanced evaporating surface. (b) Top view of the micromembrane-enhanced evaporating surface. (c) Sharp corners formed by individual wires. (d) Sintered four-layer copper woven mesh laminates. (e) Single-layer mesh. (f) 3D Micro-XCT image of microchannels.

and b were sintered in a high temperature furnace at 1000 ^{o}C in a hydrogen (H_2) atmosphere. Four-layer mesh laminates were made by sintering four layers of meshes with diffusion bonding technique (Figure 4.2d). In addition, we also studied the performances of single-layer mesh (Figure 4.2e) and microchannels (Figure 4.2f) as baselines in this study.

4.3.1 EXPERIMENTAL APPARATUS

Experimental study was conducted in a closed system. The $10 \times 15 \times 15$ cm^3 test chamber was made from aluminum as shown in Figure 4.3. One side of the chamber was covered by a piece of quartz glass as a visualization window. The other side was designed for sample installation. External lighting was provided for visualization studies. Four cartridge heaters were mounted at the four corners of the aluminum chamber to assure saturated working conditions (Figure 4.3). A proportional-integral-derivative (*PID*) temperature controller was used to accurately control the water temperature between 99.9 ± 0.2 ^{o}C and 100.1 ± 0.2 ^{o}C. Highly purified water was degassed through boiling for more than two hours at approximately 100.0 ± 0.2 ^{o}C before tests. A built-in compact condenser

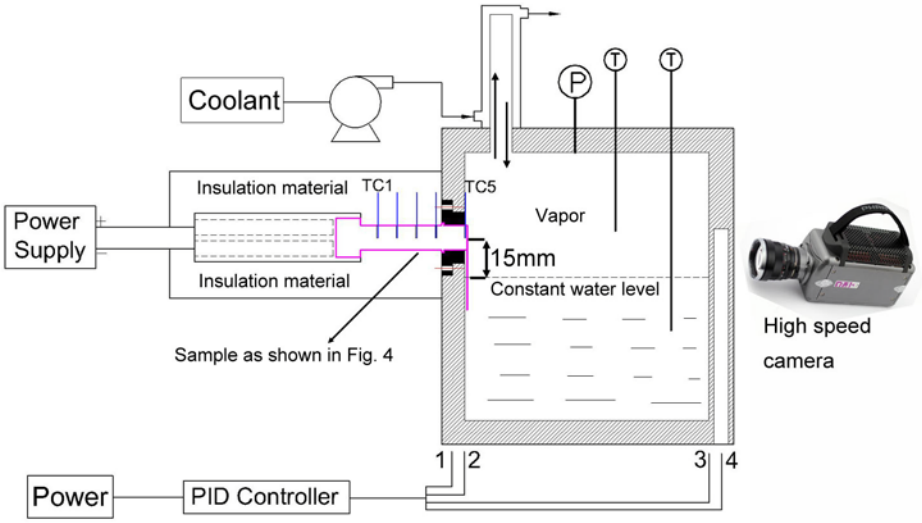

Figure 4.3 Experimental setup for the capillary evaporation in the vertical direction. Four cartridge heaters are shown as 1, 2, 3 and 4. Five thermocouples (TC) are shown as TC1 to TC5.

was designed to keep a constant water level by timely recycling the condensate. The vapor pressure and temperature inside the chamber were monitored by a pressure gauge and two *T*-type thermocouples, respectively (Figure 4.3). All tests were conducted with samples positioned in the vertical direction and with an approximately 15 *mm* distance from the center of heating area to the water level (Figure 4.3), which aimed to minimize the impacts of pool boiling.

The visualization system consisted of a high-speed camera (*Phantom V 7.3*), an infinity *K2/SC* long distance micro single port main body (*VRI-INFINITY-K2SC*), a *CF-2* objective (*VRI-MICRO-990214*), and a *NIKON T2* adapter (*VRI-MICRO-770568*). The fluid flow and bubble dynamics were captured by the high speed camera. The videos were taken at 3000 frames per second (*fps*) and replayed at 45 *fps* to show the whole oscillating cycles. The visualization setup was shown in Figure 4.3.

As shown in Figure 4.4a, the sample assembly consists of two component: a heating block and a thermocouple (*TC*) block with evaporating surfaces. The 25.4 *mm* (1

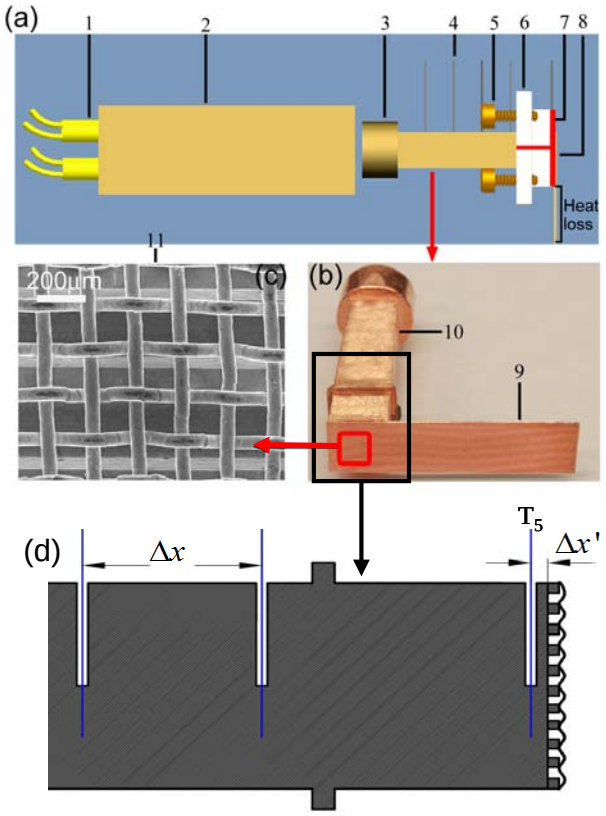

Figure 4.4 Schematic of the test sample assembly and the real sample images. (a) 1. Cartridge heater, 2. Copper heating block, 3. 1 cm × 1 cm square copper block with holes for thermocouple (*TC* block) 4. K type thermocouples, 5. Screw, 6. G-7 fiberglass, 7. High temperature *RTV* silicone, 8. micromembrane-enhanced evaporating surface, (b) 9. Photo of the micromembrane-enhanced evaporating surface, 10. Copper *TC* block, (c) SEM image of the micromembrane-enhanced evaporating surface. (d) Thermocouple arrangement and parameters for data reduction.

inch) squared copper heating block was made from copper *Alloy 101* with four heater ports in one end. Heat was provided by four 50.8 *mm* (2 *inches*) long and 6.35 mm (1/4 *inch*) in the diameter cartridge heaters (250 *W*) through an alternative current (*AC*) power supply. The *TC* block was attached on the other end of the heating block. Thermal grease was applied to reduce the contact thermal resistance between the heating and *TC* blocks, which was then insulated by *G*-7 Fiberglass to ensure one dimensional (*1D*) heat flux input. Micromembrane-enhanced structure was sintered on the *TC* block (Figure 4.4b and c) to minimize contact thermal resistance. Five *K* type thermocouples with 0.51 *mm* (0.02

inch) junction in diameter were used to measure the axial temperature distribution, which was then used to estimate the linearity of temperature profile (Figure 4.4a) and hence the approximately *1D* input heat flux. High temperature *RTV* silicone® was used to achieve mechanical sealing. Only the evaporating surfaces were exposed to the saturated vapor. The heating elements were well insulated by high temperature Nelson Firestop Ceramic Fibers to applying high heat fluxes.

4.3.2 DATA REDUCTION

Data were reduced and categorized into the parameters from Eqs. 4 to 6.

$$q'' = k\frac{\Delta T}{\Delta x} \tag{4}$$

$$T_w = T_5 - q''\frac{\Delta x'}{k} \tag{5}$$

$$h = \frac{q''}{T_w - T_{sat}} \tag{6}$$

where, q'' is the input heat flux, k is the thermal conductivity of copper; ΔT is the temperature difference between the two thermocouples; Δx is the distance between two thermocouples as shown in Figure 4.4d; T_w is the estimated temperature of the surface; T_5 is the temperature of the thermocouple *TC* #5; $\Delta x'$ is the distance from *TC* #5 to the evaporating surface; T_{sat} is the saturated water temperature; and h is the evaporation *HTC*.

Uncertainties of the temperature measurements and the length are ± 0.5 *K* for K type thermocouple (± 0.2 *K* for T type thermocouple) and 0.01 *mm*, respectively. Uncertainty propagations with 95% confidence level for the computed results in most of the ranges were estimated by Kline and McClintock method [77]. The uncertainties of heat flux, *HTC*, and superheat were ± 3.2 W/cm^2, ± 1.2 $W/(cm^2 \cdot K)$, and ± 0.8 °*C*,

respectively. Heat loss due to the fin effect was estimated to be less than 4% (Figure 4.4a).

4.4 RESULTS AND DISCUSSION

In this study, four types of evaporating surfaces with identical heating areas (1 × 1 cm^2) were experimentally investigated. These include copper microchannels (channel height and width: 250 μm, channel wall width: 250 μm), single layer copper mesh screen (thickness: 80 μm), four-layer sintered copper mesh screens (thickness: 320 μm) and the micromembrane-enhanced evaporating surfaces (total thickness of sintered microchannels and mesh: 320 μm). Dimensions of all evaporating surfaces are specified in Table 4.1.

4.4.1 CAPILLARY EVAPORATION CURVES

Figure 4.5a shows the HTC-heat flux curves for all the tested samples. Four-layer mesh screens, which have an equal thickness with the micromembrane-enhanced evaporating surfaces, showed higher *HTC* in the operating heat flux range. *HTC* on four-layer mesh screens reached a peak value of 23.1 $W/(cm^2 \cdot K)$ at the heat flux of 17.0 W/cm^2 and then kept dropping. Such a high *HTC* should result from a combination of the enhanced thin film evaporation and nucleate boiling on the large surface areas. However, the high *HTC* on four-layer mesh screens could not sustain and decreased quickly with the increasing heat flux as shown in Figure 4.5a. This was primarily caused by the increasing drying areas due to the high flow resistance. For the same reason, *HTC* on the single-layer copper mesh dropped even more sharply because single-layer mesh stored less water initially and had a significantly higher flow resistance than four-layer meshes.

Microchannels reached a CHF of 83.1 W/cm^2, but the capillary forces generated in microchannels could not maintain the liquid supply for high heat flux conditions.

As shown in Figure 4.5a and b, two micromembrane-enhanced evaporating

Table 4.1 Sample Specifics

Samples	**Parameters**		
1 layer mesh	Thickness: 0.08 mm	Wire diameter: 0.56 mm	Porosity: 0.737
4 layer meshes	Thickness: 0.32 mm	Wire diameter: 0.56 mm	Porosity: 0.693
Microchannel	Height: 0.25 mm	Width: 0.25 mm	Pillar width: 0.25 mm
Micromembrane-enhanced evaporating surfaces	Thickness: 0.32 mm	Width: 10 mm	Length: 60 mm

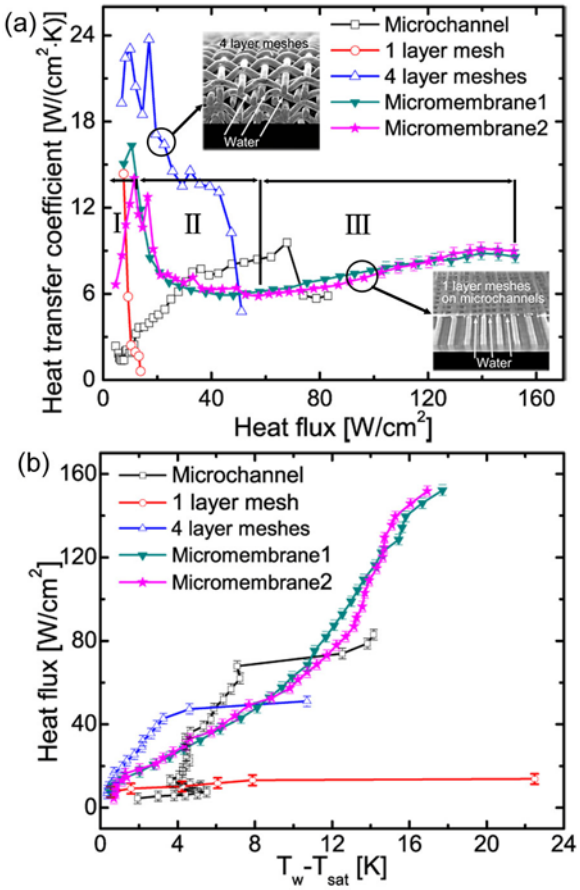

Figure 4.5 Evaporation curves and the proposed heat transfer regions. (a) Capillary evaporation heat transfer curves on the microchannels, single layer mesh, four-layer meshes, and micromembrane-enhanced evaporating surfaces. Heat transfer region I (0-

11.2 W/cm^2), region II (11.2-57.2 W/cm^2), and region III (57.2-152.2 W/cm^2). (b) q''-ΔT curves.

surfaces show a good repeatability on two individual samples. The capillary evaporation *HTC* increased with increasing input heat flux in the low heat flux region and decreased after reaching the first peak value. Then *HTC* started to increase after approaching the valley and reached the second peak value (Figure 4.5a). Finally *HTC* decreased a little bit due to the partial dryout. The whole curve exhibits an "*M*" shape. It shall be noted that the first peak *HTC*, 14.1 *W/ (cm^2·K)*, on the micromembrane-enhanced evaporating surfaces was observed at a heat flux of 11.2 *W/cm^2*. However, *HTC* decreased gradually to 5.9 *W/ (cm^2·K)* and then started to increase again with the increasing heat flux between the heat fluxes of 11.2 and 57.2 *W/cm^2*. In the high heat flux region, the peak *HTC*, 9.1 *W/ (cm^2·K)*, was achieved at a heat flux of 140.4 *W/cm^2* (Figure 4.5a) with a superheat of 16.0 *^{o}C* (Figure 4.5b). The overall *HTC* curves on the micromembrane-enhanced evaporating surfaces showed two peaks, which were significantly different from reported results and curves of the other three interfaces.

The *HTC* on the micromembrane-enhanced evaporating surfaces was superior to the microchannels and single-layer mesh when input heat fluxes were less than 37 *W/cm^2* (Figure 4.5a). The primary mechanism behind the enhanced *HTC* on the micromembrane-enhanced evaporating surfaces in the low heat flux regime is the enhanced nucleate boiling and advection induced by oscillating flow. However, microchannels showed better evaporating performance than the micromembrane-enhanced evaporating surfaces when the working heat flux exceeded 30.3 *W/cm^2* due to the fully activated flow oscillations in microchannels.

CHF on the developed micromembrane-enhanced evaporating surfaces was substantially enhanced to 151.7 and 152.2 W/cm^2 on the two individual samples. Compared to microchannels, four-layer mesh screens, and single-layer mesh screen, *CHF* was enhanced approximately 83%, 198%, and 1000%, respectively. The dramatic enhancement in *CHF* primarily resulted from the separation of the evaporation and liquid transport processes that was enabled by the micromembrane. As a result, capillary force was increased by fine meshes and flow resistance was reduced by microchannels.

4.4.2 CAPILLARY EVAPORATION ON MICROMEMBRANE-ENHANCED EVAPORATING SURFACES

According to the heat transfer characteristics and visualization study, as shown in Figure 4.5a, the whole heat transfer process can be divided into three regions. Region I (Figure 4.5a and 4.6a) was dominant by the advections induced by oscillating capillary flows and by the nucleate boiling in the microchannels since the microchannels were nearly flooded [3]. It should be noted that in the micromembrane covered microchannels, the oscillating flows and the bubbles were not confined. Although the bubbles were not able to detach due to the absence of buoyancy force, these bubbles could keep growing until collapsed. The visible bubbles and menisci distribution in the region I are shown in Figure 4.6b and c. In region I, the micromembrane (i.e., mesh screen) was well wetted, but nucleate boiling was not fully developed on micromeshes due to the relative low superheat (less than 0.82 $^{\circ}C$ on the bottom surface of microchannels as calculated). The thin film evaporation was also weak due to the flooded surfaces in region I (Figure 4.6a).

To understand the oscillation mechanism on the micromembrane-enhanced evaporating surfaces, the schematic liquid and vapor distribution in this region was

proposed in Figure 4.6. In region I, the micromembrane-enhanced evaporating surfaces, which include microchannels and micromembranes, should be saturated (or flooded) with water initially (Figure 4.6d). The liquid columns inside microchannels were separated by the growing bubbles periodically, which resulted in the periodic change of the meniscus curvature primarily in microchannels (Figure 4.6e). As a result, the upper liquid columns

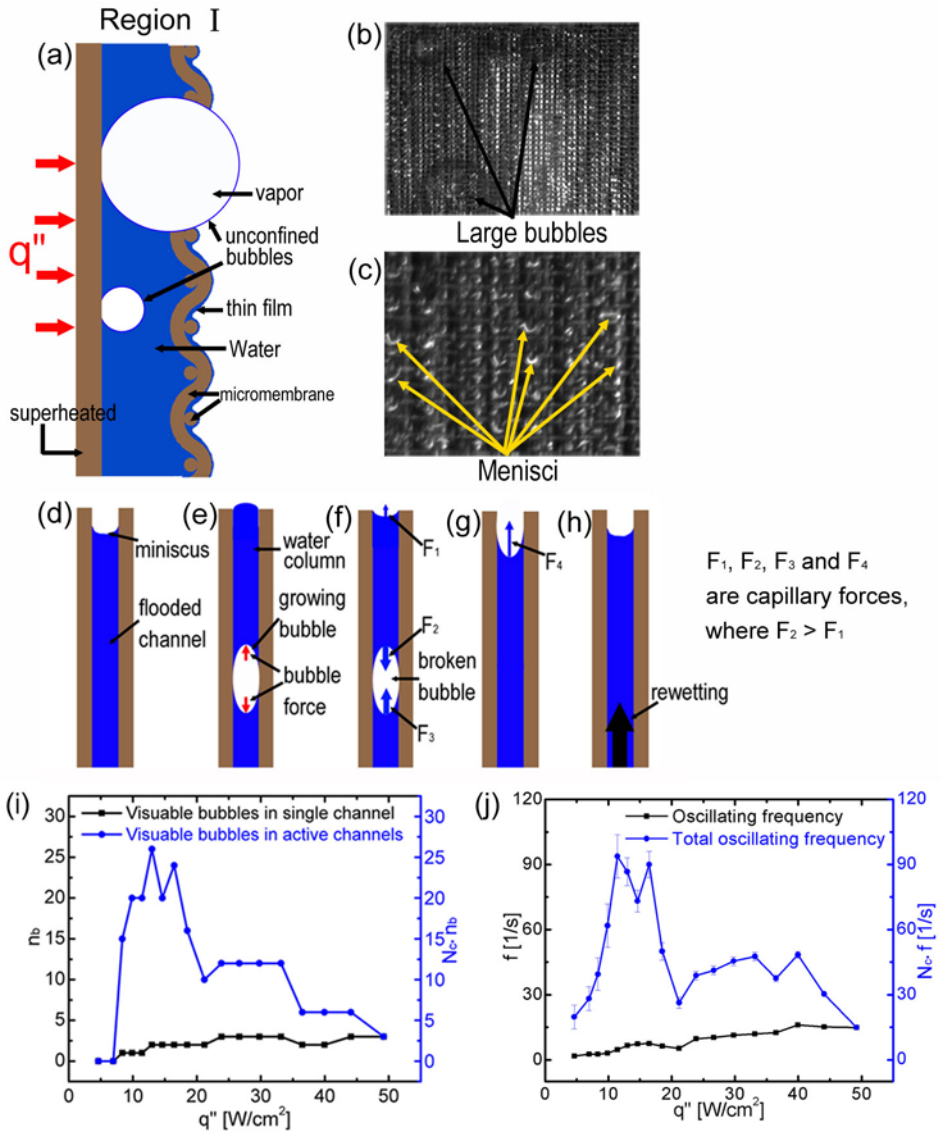

Figure 4.6 Schematic of fluid flow on the micromembrane-enhanced evaporating surfaces in region I. (a) Proposed fluid distribution in heat transfer region. (b, c) Bubble and meniscus distributions on the surfaces at the heat flux of 9.0 W/cm^2, respectively. (d-h) Hypothesized interactions between fluid and vapor inside microchannels. (i) The number of visible bubbles in a single channel, n_b, and total number of visible bubbles in active

channels, $N_c \cdot n_b$, in the low heat flux region. (j) Oscillating frequency in a single channel, f, and the total frequency in the channel array, i.e., the product of active channel number and the frequency of a single channel, $N_c \cdot f$, in the low heat flux region.

tended to move downwards due to the net capillary force (F_2-F_1) generated on the caps of the upper liquid columns. Simultaneously, the lower liquid columns were pumped up by capillary force (Figure 4.6f). The liquid columns with motions in the opposite directions ended up with a merging in a microchannel. Then, the merged liquid columns were pumped up by the capillary force generated on the meniscus located on the top ends of microchannels. The incompletely wetted microchannels were then fully rewetted by the working fluid at a velocity of more than 10 m/s as measured (Figure 4.6h). This rewetting process is similar to the multilayer liquid spreading as mentioned in Xiao's work [128]. This periodic process resulted in oscillating capillary flows and hence enhanced *HTC* during capillary evaporation in vertical direction in region I, which is radically different from the oscillating flows observed in the confined channels and closed chambers [121, 129-130]. The liquid droplets were observed to flash out of the microchannels from the top openings at the low heat flux region, which further indicated oscillating fluid motions on the micromembrane-enhanced evaporating surfaces. Nucleate boiling occurred primarily on the microchannel walls because the surface temperature on the microchannel wall was higher than that on the membrane. A higher superheat was required to initiate nucleate boiling on membrane according to the nucleate boiling theory [9, 83]. As illustrated in Figs. 6i and j, in a single microchannel, the oscillating frequency increased because the nucleate boiling was intensified and the menisci receded more rapidly due to the increased evaporating rate. However, it was also observed that not all the channels were activated because of the variations in the roughness and wettability. Hence, the

capillary flows were governed by the boiling and menisci inside these active microchannels in region I.

Region II (Figure 4.7a) is a transition heat transfer region, where the heat transfer should be dominated by thin film evaporation. When the heat flux exceeded 11.2 W/cm^2, the phase change rate was getting stronger and the liquid supply through capillary

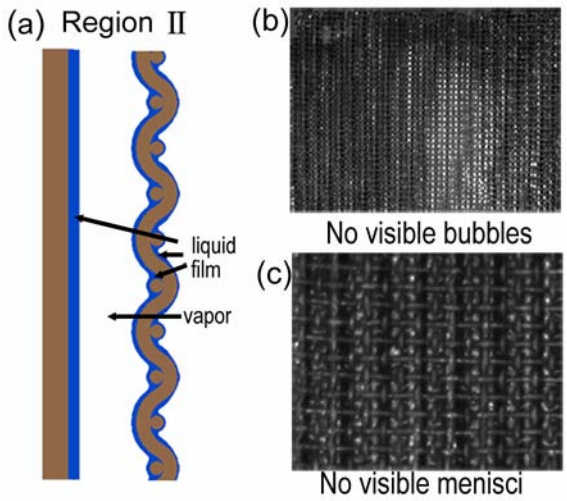

Figure 4.7 Liquid distributions in region II. (a) Hypothesized liquid distribution inside the structure. (b, c) Bubble and meniscus distributions on the surfaces at the heat flux of 40.4 W/cm^2, respectively.

pressure generated in microchannels was not sufficient in some of the microchannels. As a result, some microchannels started to be partially dry and the oscillating liquid flows were gradually suspended in these microchannels. The primary reason that results in this transition region could be the transformation of the dominant capillary force from microchannels to micromembranes. This speculation could be evidenced in Figure 4.7b and c [3], where visible bubbles were not observed. When the heat flux approached to 57.2 W/cm^2, only one microchannel was observed to be active with fluid oscillations. Accordingly, *HTC* dropped with the increasing number of non-active channels in this transition regime, as thin film evaporation started to prevail. As shown in Figure 4.5a, the

shape of the capillary evaporation heat transfer curves in regions I and II was well predicted by the trend of total frequency, which was defined by the product of the oscillatory frequency, f, and the active channel numbers N_c, as a function of input heat flux (Figure 4.6i and j).

Region III (Figure 4.8) should be dominated by the thin film evaporation and

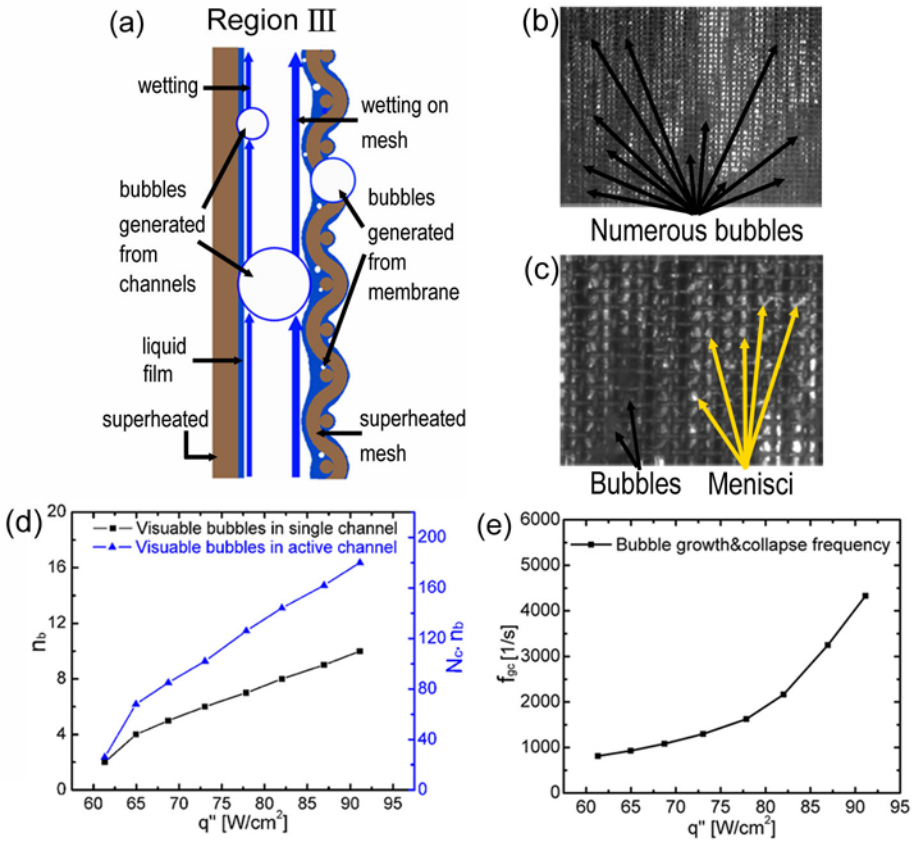

Figure 4.8 Schematic of fluid flow on the micromembrane-enhanced evaporating surfaces in region III. (a) Hypothesized fluid low and liquid distributions inside the structure. (b, c) Bubble and meniscus distributions on the surfaces at the heat flux of 61.4 W/cm^2, respectively. (d) The number of visible bubbles in a single channel, n_b, and total number of visible bubbles in active channels, $N_c \cdot n_b$, in the high heat flux region. (d) Bubble growth and collapse frequency, f_{gc}, in the high heat flux region.

nucleate boiling in microchannels as well as on the micromeshes. Figure 4.8a, b and c show that the menisci were inherently interacting with bubble dynamics [3]. When the superheat on meshes was getting higher than the onset of the nucleate boiling with

increasing heat fluxes, bubbles started to nucleate on mesh wires (Figure 4.8a). Liquid oscillations were retarded during the bubble expansion, while strong liquid pulls were observed during the menisci receding into the sharp corners formed by individual wires when bubbles collapsed [3]. Thus, the liquid motions were significantly intensified by the induced wetting and dewetting [131] processes. Consequently, the fluid flows were resumed by the receding menisci in region III (Figure 4.8b and c), where nucleate boiling occurred on the flooded microchannel walls, while thin film evaporation primarily occurred on the micromeshes. As shown in Figure 4.8d, the bubble number increased continuously with increasing heat fluxes. It was challenging to visualize individual bubbles when the heat flux exceeded 100 W/cm^2. The microchannels could not be fully saturated with working fluid due to the high velocity of vapor flow in the high heat flux region. The frequency of bubble growth and collapse as well as the menisci receding on the mesh screens would determine the frequency of local liquid wetting and dewetting processes, which are different from the liquid motions in region I. The frequency of wetting and dewetting, which was found to be closely associated with the bubble growth and collapse, increased with increasing heat fluxes as shown in Figure 4.8d. The copper meshes provide larger surface areas and more nucleate sites for heat transfer. The peak *HTC* in the region III was measured at 9.1 *W/ (cm^2·K)*, which is approximately 50% lower than the peak value (14.1 *W/ (cm^2·K)*) in the region I. The reason could be that the additional thermal resistance resulting from the vapor core that started to form in microchannels in the region II and further develop in region III. The assumption of the existence of vapor core inside microchannels (Figure 4.8a) can be validated by the fact

that liquid droplet splash from the top opening of the microchannels in region I, but was not observed in regions II and III [3].

4.5 SUMMARY OF THE MICROMEMBRANE-ENHANCED EVAPORATING SURFACES

In summary, significantly high *HTC* and *CHF* were achieved using the micromembrane-enhanced evaporating surfaces that were developed in this study. The separation of capillary pressure generation and water transport processes enabled by the micromembrane should be favorable to supply liquid. *CHF* on the developed micromembrane-enhanced evaporating surfaces was substantially enhanced to 152.2 W/cm^2. Compared to microchannels, four-layer mesh screens, and single-layer mesh screen, *CHF* was enhanced approximately 83%, 198%, and 1000%, respectively. The increased capillary forces on micromeshes and the reduced flow resistance using microchannels should be the primary reasons for the dramatically increased *CHF*. The generation of capillary forces on the newly developed interfaces was governed by the liquid evaporative rate, bubble growth and collapse and receding menisci, which were not continuous or constant. Oscillating flows were observed in the low heat flux region and HTC was increased by the induced advection. Thin film evaporation and nucleate boiling were improved by the enhanced nucleation site density and augmented surface areas through the use of micromembrane that was made of sintered single-layer micromesh, resulting in the enhanced capillary evaporation *HTC* in the high heat flux region.

CHAPTER 5

ENHANCED CAPILLARY EVAPORATION ON MICROMEMBRANE-ENHANCED HYBRID WICKS WITH ATOMIC LAYER DEPOSITED SILICA

Substantial enhancement of capillary evaporation in water was reported on the micromembrane-enhanced hybrid wicks with intrinsically superhydrophilic silica (SiO_2) coatings. Compared with bare micromembrane-enhanced hybrid wicks, evaporation heat transfer coefficient was improved from 9.1 $W/(cm^2 \cdot K)$ to 14.2 $W/(cm^2 \cdot K)$ at a heat flux of 139.3 W/cm^2, i.e., a 56% enhancement after coating a nano-thick layer of Atomic Layer Deposited (ALD) SiO_2. Different from Wenzel's effect, conformal ALD SiO_2 coatings can achieve intrinsic superhydrophilicity without significantly modifying surface roughness. The superwetting property could substantially enhance thin film evaporation by augmenting the liquid film areas and reducing film thickness, resulting in significantly enhanced evaporation. However, ALD SiO_2 coatings increased both capillary pressure and viscous drag. As a result, the critical heat flux was not enhanced in this study.

5.1 INTRODUCTION OF ENHANCED CAPILLARY EVAPORATION

Guided by Wenzel′s effect [132], the apparent contact angles can be dramatically reduced by increasing surface roughness on hydrophilic surfaces. As a result, engineered surfaces with microscale [13], nanoscale [9], patterned [17] and hierarchical [133] structures have been employed to enhance boiling and evaporation. However, it is rather challenging to distinguish the effects of augmented surface roughness and the effect intrinsic wettability on heat transfer performance. To study the effect of interfacial

wettability, Takata et al. [69] investigated the effects of surface wettability on boiling and evaporation heat transfer using sputtering coated TiO_2 on plain surfaces, yielding the enhancement on both HTC and CHF. Nonetheless, the sputtering method introduced additional surface roughness and the superhydrophilicity was not reliable and needed to be maintained by UV light. Most recently, Feng et al. [73] reported approximately 200% of CHF enhancement in pool boiling using atomic layer deposited (ALD) alumina coatings which provide superwetting and rewetting on the "hot spot". In previous studies, CHF was enhanced on the plain surfaces [69, 73] (i.e. plain copper or Pt wire), where liquid supply was governed by the bubble dynamics. Nonetheless, superhydrophilic porous structures, where fluid flow was primarily governed by the capillary pressure, have not been studied due to the difficulty in depositing conformal coatings on high aspect ratio surfaces. In this study, enhanced evaporation on intrinsically superhydrophilic micromembrane-enhanced hybrid wicks, where liquid supply should be determined by capillary flows, were obtained by coating ALD SiO_2 on micromeshes.

SiO_2 was selected in this study because of its superior hydrophilic properties and chemical stabilities in water [68, 71]. The hydrophilicity of ALD SiO_2 coatings results from the high affinity silanol (Si-OH) groups on the surface [68, 71, 134-135]. The nano-thick ALD SiO_2 coating is able to induce superhydrophilicity with surface roughness changing in the order of 10 nm. Compared to Metal-Organic Chemical Vapor Deposition (MOCVD)[136], Plasma Enhanced Chemical Vapor Deposition (PECVD) [136], Radio Frequency (RF) magnetron spattering [69] and solution based techniques [137], ALD technique has a unique capability to deposit highly conformal nano-thick films on high aspect-ratio structures [138-139]. Equally important, because of the sequential self-

terminating gas-solid reactions, strong bonding between the coatings and the substrate can be achieved by ALD technique [134]. Additionally, surface morphology and chemical property control are essential for long term operations in industrial applications [140]. ALD coatings can serve as corrosion protection layers of heat transfer surfaces [76] because copper corrosion and dissolution often imposes limitations on heat transfer performance of heat exchangers for long-term operations [140-141].

Conformal nanometer-thick SiO_2 coatings can maintain the surface morphologies, making it possible to study the effect of intrinsic wettability on heat transfer. This work aims to study the effect of ALD SiO_2 coatings on evaporation heat transfer on micromembrane-enhanced hybrid wicks.

5.2 DESIGN AND ALD DEPOSITION

5.2.1 DESIGN OF MICROMEMBRANE-ENHANCED HYBRID WICKS

This type of evaporating surfaces consist of a microscale membrane made from one-layer copper woven meshes and a microchannel array beneath [142]. Copper woven meshes (made by Belleville Wire Cloth) with a mesh number of 1509 m^{-1} (145 $inch^{-1}$) and a wire diameter of 56 μm were attached on the microchannels by diffusion bonding technique [127] to minimize the contact thermal resistance [123]. The evaporation surfaces were sintered on a 1×1 cm^2 square copper block (Figure 5.1). All tests were conducted with samples positioned in the vertical direction and with an approximately 15 *mm* distance from the center of heating area to the water level to minimize the impacts of pool boiling [142].The design and structures of the micromembrane-enhanced hybrid wicks were detailed in Ref.[142].

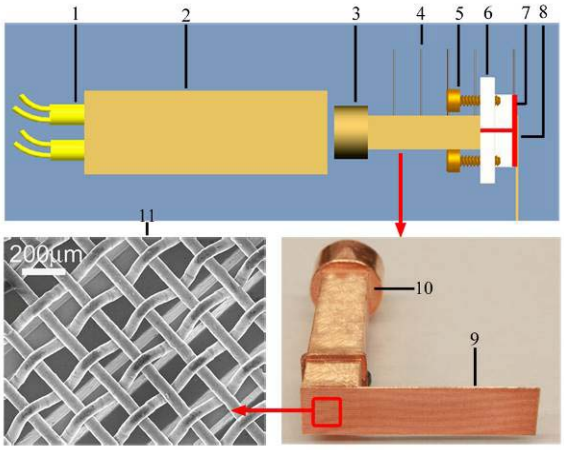

Figure 5.1 Schematic of the test sample assembly and images of the real sample. 1, 120V 250W 1/4" diameter × 2" long cartridge heater; 2, 1" copper heating block with 4 holes on the left side and 1 hole on the right side; 3, 1 cm × 1 cm square copper block with five holes for thermocouples; 4, 0.02″ diameter × 6″ long K type thermocouple; 5, Screw; 6, G-7 fiberglass; 7, High temperature RTV silicone; 8, 10 mm wide × 0.8 mm thick × 50 mm long hybrid wicks; 9, Photo of the hybrid wicks; 10, Photo of the square copper block; 11, SEM image of the hybrid structure.

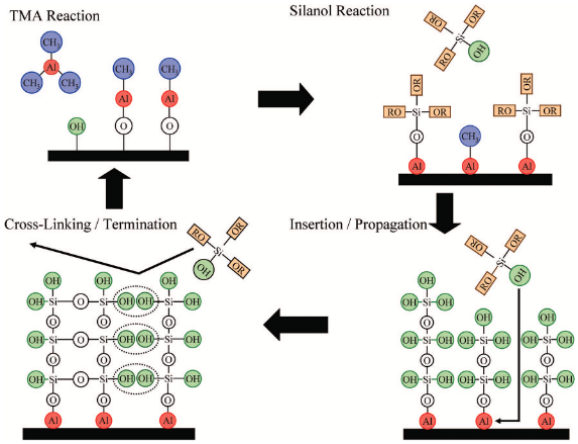

Figure 5.2 Main steps in the growth mechanism of rapid ALD SiO_2 [81].

5.2.2 ALD DEPOSITION OF SILICA

Atomic layer deposition is a self-limiting (the amount of film material deposited in each reaction cycle is constant), sequential surface chemistry that deposits conformal thin-films of materials onto substrates [138]. 12 nm-thick ALD SiO_2 was deposited on the evaporating surfaces that were developed in previous study [142]. ALD was carried at

150 °C in a viscous-flow, hot-wall type ALD reactor [78]. The reactor was operated in a static mode for conformal growth of oxides on the micromembrane-enhanced hybrid wicks with a high aspect-ratio. Ultra-high purity N_2 was used as a carrier gas. Prior to SiO_2 deposition, ALD alumina (Al_2O_3) was pre-deposited as a seed layer in order to facilitate the SiO_2 nucleation and growth and hence to ensure the conformality of the SiO_2 films. The trimethylaluminum (TMA) and water chemistry was used for ALD Al_2O_3 [79], while the ALD SiO_2 was deposited in so-called "rapid″ mode using tris (tert-pentoxy) silanol [81] (Figure 5.2). The chemistries used for ALD were well studied and shown to yield high quality films [79-81]. The number of deposition cycles of ALD Al_2O_3 coatings was approximately 80 at a typical growth rate of 0.1 nm /cycle. After 80 cycles of Al_2O_3 coating, one cycle of ALD SiO_2 was coated at an approximate growth rate of 12 nm /cycle. Therefore, the thicknesses of ALD Al_2O_3 and ALD SiO_2 films were 8 nm and 12 nm, respectively. The total thickness of the ALD Al_2O_3 and SiO_2 coatings was approximately 20 nm. To study the effect of plasma cleaning, bare hybrid wicks were cleaned by oxygen plasma for 60 seconds to create hydrophilic copper oxide [143].

During the evaporation on the ALD SiO_2 coated micromembrane-enhanced hybrid wicks, the only driving force for fluid supply was capillary pressure generated by the micromembrane. The one dimensional (1D) input heat flux was supplied by the copper heating block through the four cartridge heaters and estimated from Fourier's law from the measured temperature gradient and the given thermal conductivity of copper. The capillary evaporation were also visualized by a high-speed camera (Phantom V 7.3) with an infinity K2/SC long distance micro single port main body, a CF-2 objective, and a NIKON T2 adapter [144].

5.3 CHARACTERIZATION OF THE ALD SiO_2 COATED INTERFACE

Surface morphologies of the ALD SiO_2 coated micromembrane were characterized by atomic force microscopy (AFM) as shown in Figure 5.3. The root mean square (RMS) roughness, R_q, was used to characterize the surface roughness. $R_q = \sqrt{\frac{1}{MN}\sum_{i=1}^{M}\sum_{j=1}^{N}(Z_{i,j} - Z)^2}$, where R_q is the RMS roughness; M, N are the total sampling times in the length and width direction; i, j are the sampling times; $Z_{i,j}$ is the sampling height; Z is the average height. The RMS roughness on a plain copper surface was 1.2 nm and increased to 2.9 nm after the nano-thick ALD coatings. This indicated that the change of the surface roughness resulted from ALD SiO_2 coatings was minor and hence, the impact of augmented heat transfer areas is negligible. As shown in Figure 5.3a and b, the three dimensional (3D) AFM images well illustrated the conformality of the ALD coatings.

The static contact angle measured with a 5 μL of highly purified water droplet was employed to characterize the hydrophilicity of the ALD coatings. Before the measurement, the samples were cleaned by plasma for 15 seconds with the oxygen flow rate at 6 mL/min to remove carbon contaminations. The contact angle on the ALD SiO_2 coated plain surface was reduced from 49.6^o (Figure 5.3c) to 4.7^o (Figure 5.3d), i.e., intrinsically superhydrophilic. The apparent contact angle on the ALD SiO_2 coated hybrid wick was measured at nearly 0^o because of the Wenzel′s effect [132] (Figure 5.3e).

5.4 TWO DIMENSIONAL MODEL OF TEMPERATURE DISTRIBUTION

Because of the symmetry lines (Figure 5.4a), only one unit of hybrid wick has been chosen to be simulated (conduction heat transfer). As it is depicted in Figure 5.4b, dark gray area represents the micro-channels and light gray represent combination of fluid and mesh. In order to simplify mesh and fluid, a T-shape has been taken out (Figure

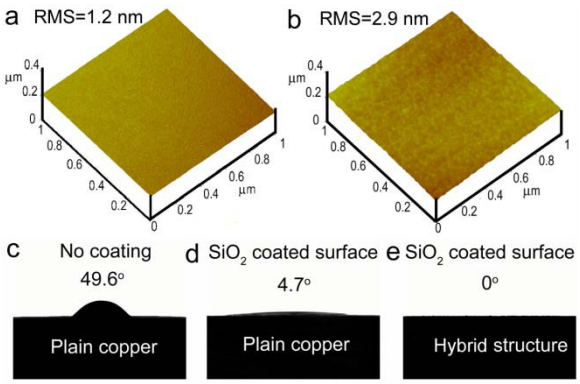

Figure 5.3 Characterization of the ALD SiO_2 coating. (a) 3-D AFM image of bare copper mesh. (b) 3-D AFM image of the conformal SiO_2 ALD coated copper mesh. (c) Contact angle on bare copper sheet. (d) Contact angle on ALD coated copper sheet. (e) Contact angle on ALD coated hybrid structure.

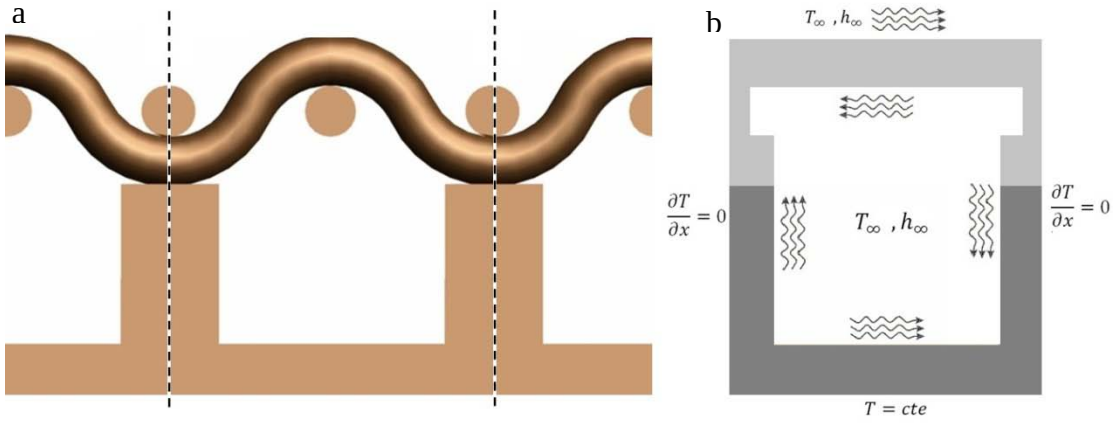

Figure 5.4 Boundary layer and assumption. (a) One unit of hybrid mesh in the neighborhood of others (b) Model and boundary conditions used for simulation

5.4b) and replaced by fluid, being said, thermal properties for this area (light gray) are averaged values based on thermal properties of mesh and fluid. Also, boundary conditions have been illustrated in the Figure 5.4b. Please note that constant temperature at the bottom and h_∞ are calculated based on this paper's experimental results and T_∞ is the saturation temperature.

5.5 ENHANCED CAPILLARY EVAPORATION

In this experimental study, three types of micromembrane-enhanced hybrid wicks, i.e., bare, ALD SiO_2 coated and plasma-CuO coated surfaces were evaluated. Compared with hybrid wicks without coating, as shown in Figure 5.2a and b, ALD SiO_2 coatings did not enhance evaporative CHF, i.e., from 151.7 *W/cm*^{2} to 151.9 *W/cm*^{2}. However, HTC was significantly improved after applying ALD SiO_2 coatings, for example, from 9.1 *W/(cm*^{2}*·K)* to 14.2 *W/(cm*^{2}*·K)* at a heat flux of 139.3 *W/cm*^{2}, which is a 56% enhancement (Figure 5.5a). The plasma generated copper oxides were also examined to study the heat transfer enhancement. However, copper oxide obtained in the plasma cleaning process was not sustainable. The superhydrophilicity enabled by CuO faded quickly because the

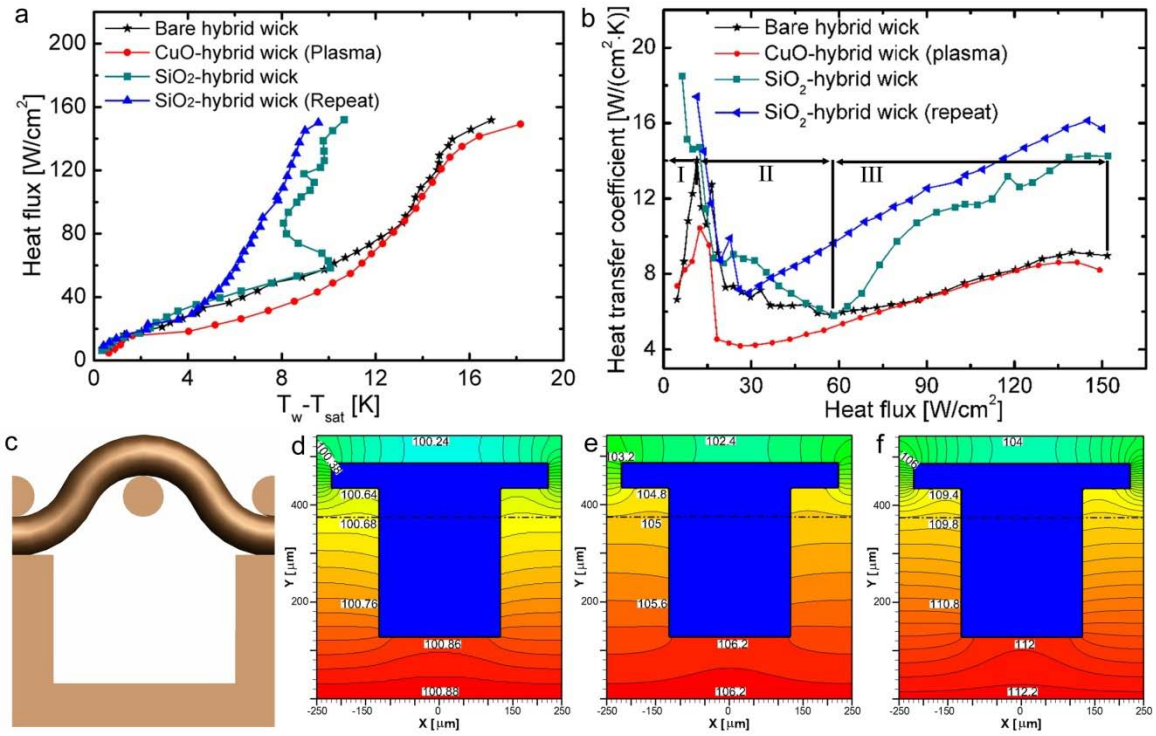

Figure 5.5 Evaporating heat transfer curves on micromembrane-enhanced hybrid wicks with various surface treatments. (a) ΔT-q" curves. (b) q"-h curves. (c) Schematic view of the hybrid wick. (d) Temperature distribution at a heat flux of 9.0 W/cm^2 in region I. (e) Temperature distribution at a heat flux of 40.4 W/cm^2 in region II. (f) Temperature distribution at a heat flux of 61.4 W/cm^2 in region III. The unit of temperature is ^{o}C for d, e and f.

plasma treatment can only oxidize the surface wire of copper meshes. The evaporating HTC was not enhanced by plasma induced copper oxides in high heat flux regime (Figure 5.5a). A repeat test was conducted to confirm the HTC enhancement as shown in Figure 5.5a. This demonstrated that the capillary evaporation HTC can be significantly enhanced by ALD SiO_2, instead of the plasma induced CuO.

5.6 EVAPORATION ENHANCEMENT MECHANISM

According to our previous study, the evaporation process on the bare micromembrane-enhanced hybrid wicks can be divided into three regions [144] (Figure 5.5b). Region I is dominated by the oscillating flows and nucleate boiling inside microchannels. Region II is governed by the thin film evaporation on both microchannels and micromembrane. Region III is determined by nucleate boiling and thin film evaporation on both microchannels and micromembrane.

In this study, a two-dimensional (2D) model was developed to study temperature distribution in the cross section of the evaporating structures as shown in Figure 5.5c, d, e and f (Refer to supplementary information for boundary conditions and assumptions) to further reveal the heat transfer mechanism,. In region I, nucleate boiling was primarily initiated on the bottom walls of microchannels because the sufficient superheat (i.e., 100.86 ^{o}C as shown in Figure 5.5d). In region II, the temperature on side walls reached 104.8 ^{o}C (Figure 5.5e), high enough to trigger nucleate boiling. However, the heat transfer was still dominated by thin film evaporation because of the insufficient liquid supply during the transition of the capillary force from the microchannels to micromembrane [144]. Additionally, the required superheat to nucleate bubbles on micromembrane with relatively larger cavities should be higher than that on

microchannels as guided by Hsu's model [145] (Figure 5.5e). In region III, the temperature on micromembrane reached 109.4 ^{o}C (Figure 5.5f) and the liquid supply was sufficient after the oscillating flows resumed [144]. As a result, the nucleate boiling can occur in microchannels and on micromembrane [146]. Thin film evaporation should be dominated on the superhydrophilic micromembrane during the entire heat transfer process according to visualization study.

As shown in Figure 5.5b, in region I, the evaporation curve on the ALD SiO_2 coated hybrid wicks shared a similar shape from that on the bare hybrid wicks, i.e., the overall HTC decreased with the increasing heat flux, resulting from the additional thermal resistance introduced by the vapor core formed inside microchannels. Although bare micromembrane was not fully saturated in region I, the superhydrophilic ALD SiO_2 coated hybrid wicks appeared to be fully saturated with liquid as visualized (Figure 5.6a and e). This can also be validated in Figure 5.6i, j, k and l. The static wetting height in microchannels is described as: $h=(2\gamma\cos\theta)/(\rho g R)$, where h is the static capillary length, γ is the surface tension of water, θ is the contact angle, ρ is liquid density and R is the half width of the microchannel. Since the contact angle was reduced from 49.6^{o} to 4.7^{o}, h_2 should be larger than h_1 (Figure 5.6i, j), where h_1 and h_2 are the capillary heights in bare and ALD SiO_2 coated tubes, respectively. The frequency of the oscillating flows, which was induced by multilayer liquid wetting as indicated in Xiao's model [147], would increase (Figure 5.7a) and result in strong advections. Thus, the HTC on ALD SiO_2 coated hybrid wicks was significantly enhanced in the low heat flux region, which was consistent to the observation in previous study [69].

Region II is a transition region [144] where the oscillating liquid spreading and wetting process temporarily suspended. In this region, the sidewall temperature increases with the increasing heat flux and became superheated (Figure 5.5e). Consequently, bubbles started to nucleate on the microchannel sidewalls. The substantially enhanced nucleate boiling eventually led to the global liquid supply crisis in microchannels. As a result, the capillary flows were suspended in Region II. The heat transfer in Region II was dominated by nucleate boiling inside microchannels and thin film evaporation on the meshes. The averaged HTC on ALD SiO_2 coated surfaces in region II were approximately 15% higher than that on the bare ones. According to visualization study, at the heat flux of 40.4 W/cm^2, the ALD SiO_2 coated sample was fully wetted (Figure 5.6b) while the bare sample was partially dryout (Figure 5.6f). This observation indicated that HTC in region II was primarily increased by enhanced thin film evaporation because of the improved wetting conditions (Figure 5.6b and f).

In Region III, the copper meshes were sufficiently superheated (Figure 5.5f) and capillary evaporation occurred on micromembrane, which caused menisci receding and rewetting in the sharp corners. This could induce oscillating capillary flows. Therefore, the dynamic capillary forces induced by menisci receding transformed from microchannels to micromembrane. Hence, the liquid supply was resumed. The superhydrophilic ALD SiO_2 coatings substantially enhanced thin film evaporation in this region (Figure 5.5b). This observation was consistent with a recent study at which ALD alumina (Al_2O_3) coated platinum (Pt) wire was used to enhance pool boiling heat transfer because of the superwetting property [30]. The superwetting property of the ALD SiO_2 coatings contributed to the local wetting and rewetting of the copper wires (Figure 5.d

and m). Hence, the thin liquid film can sustain and result in a significant improvement of evaporative heat transfer (Figure 5.6c and g). As shown in Figure 5.6d and h, partial dryout or so called "hot spot" occurred on the bare mesh wires was not observed on the ALD SiO_2 coated micromembrane because wetting areas can be sustained by the fast

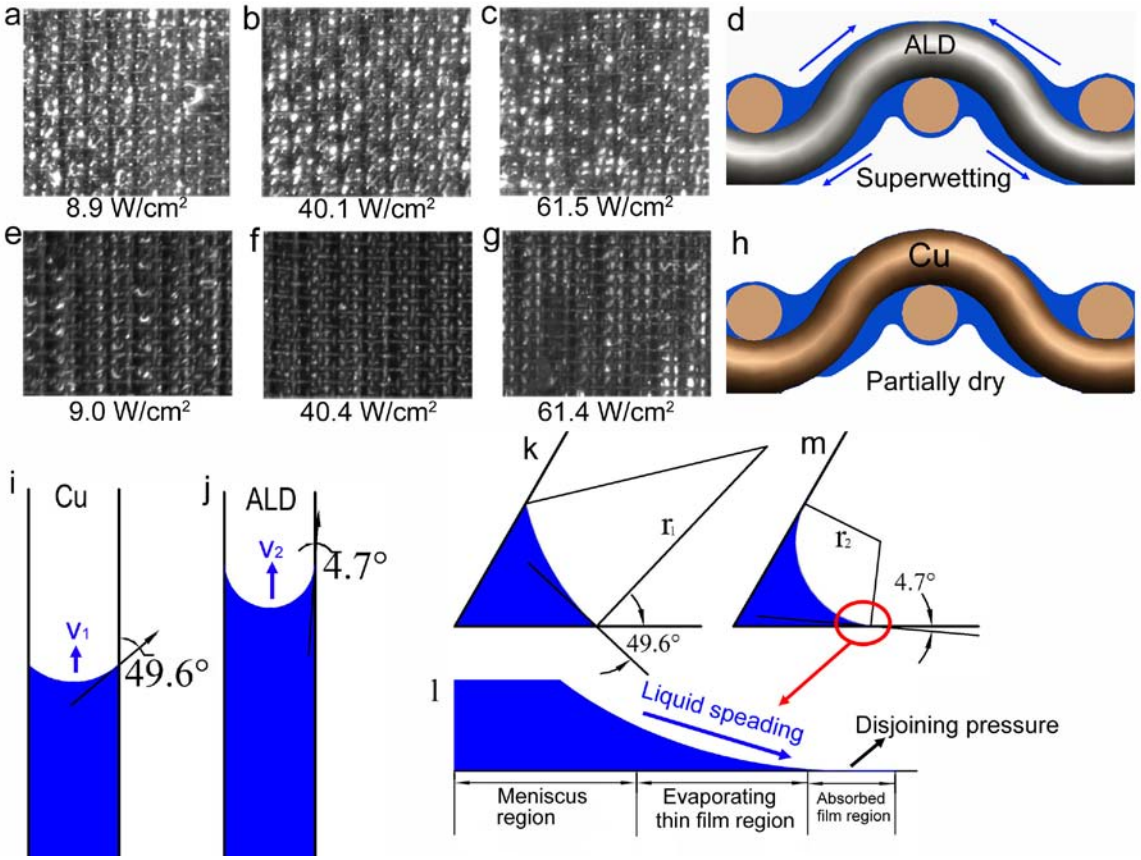

Figure 5.6 The superwetting property enabled by ALD SiO_2 coatings. (a-c) Liquid distributions on the ALD SiO_2 coated micromembrane-enhanced hybrid wicks at heat fluxes of 8.9, 40.1 and 61.5 W/cm^2. (d) Schematic diagrams of liquid distribution on the ALD SiO_2 coated micromembrane-enhanced hybrid wicks. (e-g) Liquid distribution on the bare micromembrane-enhanced hybrid wicks at heat fluxes of 9.0, 40.4 and 61.4 W/cm^2. (h) Schematic diagrams of liquid distributions on the bare micromembrane-enhanced hybrid wicks. (i) Capillarity in a bare Cu microchannel. (j) Capillarity in an ALD SiO_2 coated microchannel. (k) Cross-section of meniscus on a bare copper corner. (l) Liquid film distribution on ALD SiO_2 coated interfaces. (m) Cross-section of meniscus on an ALD SiO_2 coated corner.

liquid spreading processes (Figure 5.6m). This can also be validated by the Washburn′s law [148-149] that describes the dynamic wetting process. The penetrated distance, L, is described as: $L=(R\sigma\cdot cos\theta/(2\mu))^{1/2}\, t^{1/2}$, where R is the half width of microchannels; σ is the liquid surface tension; θ is the contact angle; μ is the liquid dynamic viscosity; and t is the penetrating time. This equation verifies that at a constant time the intrinsically superhydrophilic structure can achieve a longer liquid spreading length. This also indicates the velocity of liquid supply, v_2, in the superhydrophilic microchannels is higher than the liquid velocity, v_1, in bare microchannels. Thus, wetting areas can be augmented and maintained by applying conformal superhydrophilic ALD SiO_2 coatings (as shown in Figure 5.6a, b and c) in the dynamic wetting process. The effective evaporating heat transfer areas are substantially increased by superhydrophilic ALD SiO_2 coatings.

In addition, the local liquid distributions were improved by the intrinsically superhydrophilic ALD SiO_2 coatings (Figure 5.6k and m). Disjoining pressure results in a pressure gradient and provides the primary driving force to spread the local liquid film. The superhydrophilic interface yields a smaller film pressure gradient and larger friction drag [150], resulting in a thinner liquid film in the evaporating process. Thus, the local thin film evaporation can be enhanced by improving the wettability as predicted by a theoretical model [151].

In previous study, visualization studies illustrated that only a part of microchannels was fully wetted or activated on the bare micromembrane-enhanced hybrid wicks [144]. As shown in Figure 5.7a, the frequency of oscillating flows on the ALD SiO_2 coated evaporating surfaces was approximately one order of magnitude greater than that of the bare structures in the low heat flux region. The number of visible

bubbles in the low heat flux region was also increased by the superhydrophilic coatings due to the enhanced surface wettability (Figure 5.7b). The increased frequency of bubble growth and collapse (Figure 5.7c) could be caused by the enhanced thin film evaporation on the microlayer underneath the bubbles, resulting in a high bubble growth rate [152]. However, the bubble growth and collapse phenomena were different from those in pool

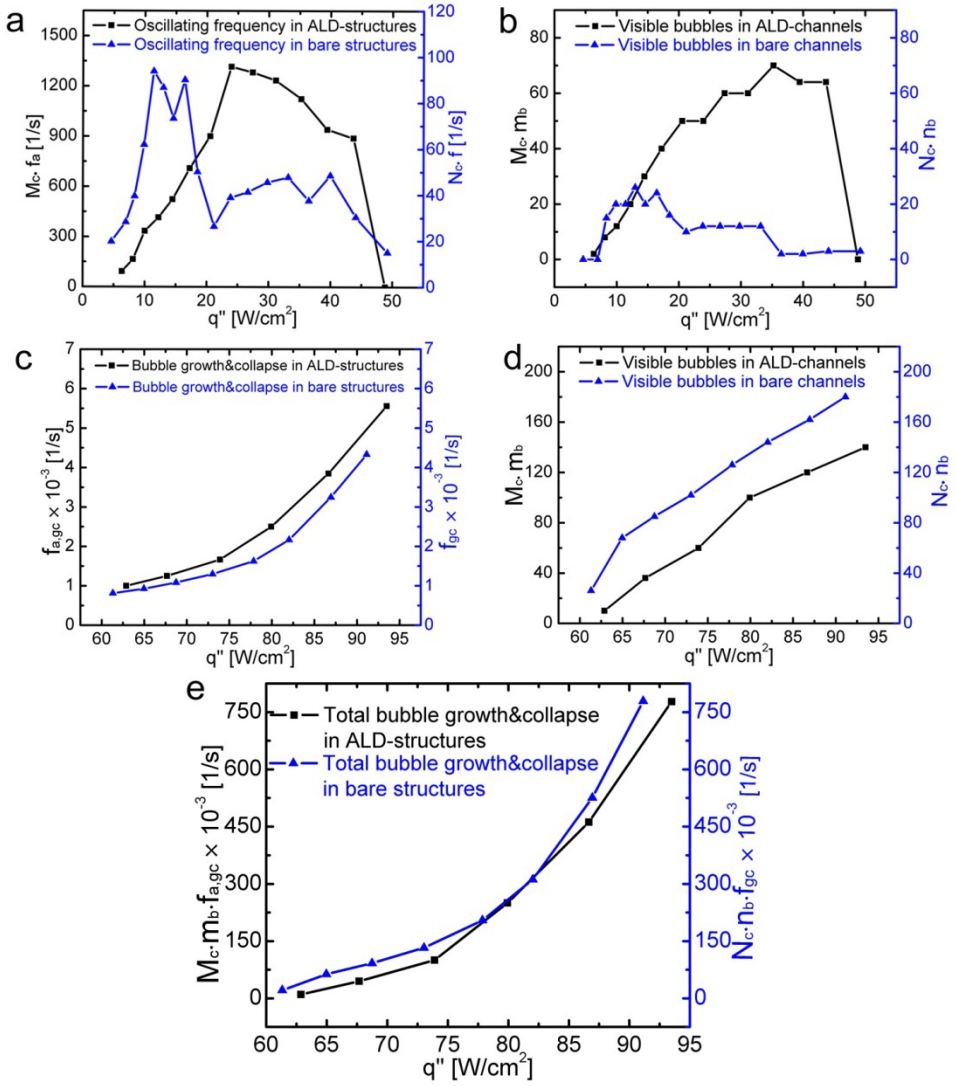

Figure 5.7 Comparisons of oscillating flows on the ALD SiO_2 coated and bare hybrid wicks (a) The total oscillating frequency, $M_c \cdot f_a$, on the ALD SiO_2 coated micromembrane-enhanced hybrid wicks; M_c is the number of active channels; and f_a is the frequency of fluid flow in a single active channel. $N_c \cdot f$ is for the bare structure. (b) The total number of visible bubbles in active channels, $M_c \cdot m_b$. M_c is the number of

visible bubbles in a single active channel; and m_b is the number of active channels. $N_c \cdot n_b$ is for the bare structure. (c) Bubble growth and collapse frequency, $f_{a,gc}$. f_{gc} is for the bare structure. (d) The total number of visible bubbles in active channels, $M_c \cdot m_b$, in the high heat flux region. $N_c \cdot n_b$ is for the bare structure. (e) Total bubble growth and collapse frequency, $M_c \cdot m_b \cdot f_{a,gc}$ is for ALD coated structure, $N_c \cdot n_b \cdot f_{gc}$ is for the bare structure.

boiling investigation because of the absence of buoyancy force [152]. Although the ALD SiO_2 coated surfaces were superwetted in the high heat flux region, the number of visible bubbles was reduced (Figure 5.7d) since some of the superhydrophilic cavities were inactive because of flooding [91, 146]. The total bubble growth and collapse frequency was nearly identical on the bare and ALD coated evaporating surfaces (Figure 5.7e), implying that the HTC enhancement primarily resulted from the improved thin film evaporation and advections, instead of nucleate boiling.

The enhanced HTC ascribed to the improved local wetting. However, CHF of capillary evaporation was not enhanced by the ALD SiO_2 coatings as shown in Figure 5.6a. CHF is generally determined by the global liquid supply, which is governed by the capillary pressure generated by micromeshes and flow resistance through microchannels. When evaporation was approaching CHF conditions, thin film evaporation occurred primarily on micromembrane and the liquid film was maintained by liquid spreading. Nucleate boiling was occurred on the flooded microchannel walls with the high frequency bubble growth and collapse process. Global liquid flowed through the microchannels at the flow velocity v, and $v=q''/\rho h_{fg}$, where q'' is the heat flux; ρ is saturated liquid density; and h_{fg} is the liquid latent heat. The major forces that determine fluid flows are capillary pressure (Δp) and viscous drag ($\Delta p'$). Capillary pressure is determined by the meniscus according to Young-Laplace equation: $\Delta p=2\sigma/r$, where Δp is capillary pressure, σ is surface tension and r is the principal radius of curvature. The

decreasing contact angle could result in a reduced meniscus in a conformal sharp corner [151], that is, $r_1 < r_2$ as shown in Figure 5.3k and m, where r_1 and r_2 are the radii of curvature for bare and ALD SiO_2 coated interfaces. Herein, conformal superhydrophilic ALD SiO_2 coatings could yield higher capillary pressure than the bare surfaces. However, superhydrophilic coatings also result in higher viscous drag as reported by Wu and Cheng [153]. Also, the increased fluid velocity in the microchannels may result in higher flow resistance on the superhydrophilic surfaces as indicated by the pressure drop in microchannels: $\Delta p' = \frac{1}{2} f \rho v^2 L_0 / D_h$, where $\Delta p'$ is the pressure drop through the channel; v is the fluid velocity; L_0 is the flow length; D_h is the hydrodynamic diameter; and f is the friction factor. Therefore, both capillary force and viscous drag were increased by applying conformal superhydrophilic ALD SiO_2 coatings. Therefore, CHF was not enhanced in this study.

5.7 SUMMARY OF THE MICROMEMBRANE-ENHANCED HYBRID WICKS

Intrinsically superhydrophilic ALD SiO_2 coatings with a nanoscale modification on surface roughness can significantly increase the HTC by 56% during the capillary evaporation process. The enhancement results from the induced advections in the low heat flux region and enhanced thin film evaporation in the high heat flux region, respectively. CHF, which was governed by the global liquid supply, i.e., by the capillary pressure and viscous drag in the dynamic process, was not enhanced since the conformal superhydrophilic ALD SiO_2 coatings increased both the capillary pressure and viscous drag in this study.

CHAPTER 6

TRANSPORT PHENOMENA ON NANOENGINEERED HYDROPHOBIC-HYDROPHILIC INTERFACES

Solid-liquid interfacial characteristics such as wettability, surface roughness and the presence of micro/nano bubbles are significant to the heat and mass transports. Hydrophilic interface is superior to maintaining the surface wetting for enhanced thin film evaporation [146]. Smooth hydrophobic interface is able to reduce the friction drag due to the induced slippage [154-155]. Nanotextured hydrophobic structures inevitably track micro/nano bubbles, which can enhance nucleate boiling [145] by augmenting nucleation site density and enable drag reduction by inducing shear-free boundary conditions [156]. Nanoengineered porous interfaces with partially hydrophilic and partially hydrophobic areas were expected to improve the partial wetting and track nanobubbles, resulting in enhanced heat transfer and reduced friction drag.

6.1 INTRODUCTION

Carbon nanotubes (CNTs) [157] have been used to enhance two phase heat and mass transport, e.g. pool boiling [158-160], flow boiling [161-162], evaporation [163-164] and nanofluids [165-167]. However, the enhancement was retarded by the intrinsic superhydrophobicity of pristine carbon nanotubes. McHale and Garimella [23] deposited copper on the multiwall carbon nanotubes (MWCNTs) and tuned the hydrophobicity to hydrophilicity yielding heat transfer enhancement. In this study, partially hydrophobic

and partially hydrophilic MWCNTs were synthesized from functionalized multiwall carbon nanotubes (FMWCNTs) by inducing hydrophilic functional groups on the defect areas of pristine MWCNTs. This nanoengineered hydrophobic-hydrophilic interface exhibited the advantages of both hydrophobic and hydrophilic characteristics, resulting in superior properties in advancing heat and mass transports.

The ideal porous interface to enhance capillary evaporation should be able to provide a low flow resistance and a simultaneous high capillary force for liquid supply [54, 142]. Superhydrophobic interface is able to reduce the flow resistance [168], nonetheless, it can not provide sufficient capillary driving force due to the small surface energy. Superhydrophilic surface is superior to generating high capillary pressure [169] while the associated flow resistance is relatively high [94, 169]. A composite interface with cool hydrophilic areas and hot hydrophobic areas is able to accelerate the droplet flow with the aid of Marangoni flow [94-95]. This is significantly helpful for the local liquid supply in the evaporation process since the temperature of hydrophilic areas is lower than that of the hydrophobic areas. Furthermore, fluid oscillations induced by the periodic bubble growth and collapse significantly affect the liquid supply and nucleate boiling. It has been demonstrated that carbon nanotube enabled hydrophobic-hydrophilic interfaces can increase the bubble departure frequency, decrease the bubble size augment the nucleate site density and thus enhance the nucleate boiling [146]. However, in reality micro/nanofabricatons [94, 100] are costly and challenging to make such an interface, especially on the high aspect ratio porous structure. In this study, nanoengineered partially hydrophobic and partially hydrophilic interfaces were developed to enhance the heat transfer and increase the CHF.

6.2 SYNTHESIS AND DEPOSITION

MWCNTs were oxidized in an acid reflux bath at 80 ºC for 4 hrs to generate defects and to grow hydrophilic carboxylic and hydroxylic functional groups on the surface of each MWNT. Aqua regia, a mixture of HCl (12M) and HNO_3 (16M) in 1:1 volume ratio, was used to oxidize MWNTs. The treated MWNTs were filtered out and thoroughly rinsed with DI water. A sonicator was used to disperse FMWCNTs in isopropyl alcohol to form “inks” for subsequent spray coating. 5 mg of FMWCNTs dispersed in 10 ml of isopropyl alcohol with the addition of 20 mg of a 5% Nafion™ (Dupont DE521) solution was used to form the "inks". A 700W, 20 kHz, sonic probe was used to treat the "inks" with Nafion and FMWCN (NFMWCNT) suspension for 1 hour (45 seconds - off and 15 seconds-on duty cycle) at a power level of 30%. Nafion was slowly added into the MWNT mixture while dispersing. The combination of acid reflux treatment and the use of nafion as surfactant resulted in excellent dispersion of CNT in isopropyl alcohol.

The NFMWCNT "ink" was deposited on the hybrid wicks using an ultrasonic spray coater (Sonotek Exacta-Coat). A 120 kHz spray head was used with an ink feed rate of 0.2ml/min. The ultrasonic spray head was programmed to move in a raster pattern at a distance 5 mm from the top surface of the substrate, traversing at a speed of 25 mm/sec, forming a track at the width of approximately 1.25mm. The raster pattern was repeated numerous times (coats) to building up the thickness of the coating. During spray, the substrate was heated to ~100 ºC to speed up the evaporation of the solvent.

6.3 HIERARCHICAL HYDROPHOBIC-HYDROPHILIC SURFACES

Pristine carbon nanotubes (Figure 6.1a) were oxidized in the concentrated nitric

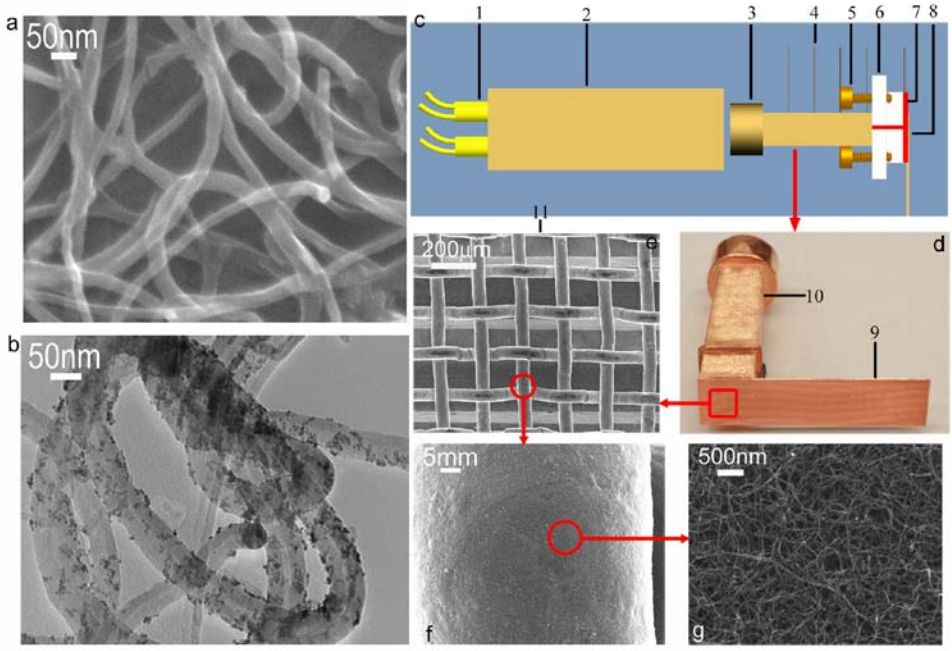

Figure 6.1 Characterization of the FMWCNTs and FMWCNT coated hybrid wicks. (a) Pristine MWCNT coatings. (b) Functionalized MWCNT coatings with P_t tracer particles. (c) Schematic of the test sample assembly. **1.** Cartridge heater, **2.** Copper heating block, **3.** 1 cm × 1 cm square copper block with holes for thermocouple (*TC* block) **4.** K type thermocouples, **5.** Screw, **6.** G-7 fiberglass, **7.** High temperature *RTV* silicone, **8.** hybrid wick, (d) **9.** Photo of the hybrid wick, **10.** Copper TC block. (e) SEM image of the hybrid wick. (f) FMWCNT coated single copper wire. (g) Nanoengineered hydrophobic-hydrophilic FMWCNT coatings.

acid (H_2NO_3) to grow functional groups. The FMWCNTs were dispersed in the isopropyl alcohol with the aid of high power ultrasonic. Amphiphilic Nafion was used to help disperse the FMWCNTs, strengthen the bonding of the FMWCNT coating to the substrate and introduce superhydrophilic functional groups ($-SO_3H$). Wettability-tunable interfaces with numerous nanoscale or submicrometer interconnected cavities were synthesized from partially hydrophobic and partially hydrophilic FMWCNTs (Figure 6.1b). Positive charged platinum ions (Pt^{4+}) were employed as tracer particles to locate the functional group distribution on the FMWCNT wires and buddles.

The nanoengineered interface made of amphiphilic nafion and FMWCNT (NFMWCNT) was developed to enhance capillary evaporation. As shown in Figure 6.1c,

four cartridge heaters integrated with a copper block were used as the heating source. A thermocouple (TC) block with 1 cm^2 cross-section area was employed to generate one-dimensional (1-D) heat flux. Five thermocouples were used to record the temperature distributions. The bi-porous structure was attached on the heating block by diffusion bonding technique (Figure 6.1d). In order to minimize the influence of pool boiling, the bi-porous structure, which consisted of single layer copper woven mesh sintered on microchannel array, was positioned in the vertical direction with a 15 mm distance from the water level to the center of heating area. The well-dispersed NFMWCNT inks were deposited on the bi-porous structure by an ultrasonic spray coater (Figure 6.1e and f). The copper mesh wires and microchannels were coated by the straw-like NFMWCNTs (Figure 6.1g). Four different types of coatings, pristine MWCNTs, FMWCNTs, NFMWCNTs and heated NFMWCNTs, were tested and compared to show the heat transfer enhancement mechanisms.

6.4 CAPILLARY EVAPORATION PERFORMANCES

Figure 2a and b show the heat transfer performances of different nanoengineered interfaces. Pristine MWCNT coatings could increase the HTC from 7.5 $W/(cm^2 \cdot K)$ to 10.5 $W/(cm^2 \cdot K)$ at the heat flux of 104.3 W/cm^2. FMWCNT, NFMWCNT and heated NFMWCNT could increase the HTC from 9.0 $W/(cm^2 \cdot K)$ to 9.6, 11.1 and 11.7 $W/(cm^2 \cdot K)$ at the heat flux 136.7 W/cm^2, respectively. Intrinsically superhydrophobic pristine MWCNTs were able to enhance the heat transfer because the copper substrate was hydrophilic, hence, liquid could be supplied by capillary force on the wetted substrates. MWCNT coatings augmented the nucleate site density and surface areas, yielding enhanced nucleate boiling. The internal bonding forces of different carbon

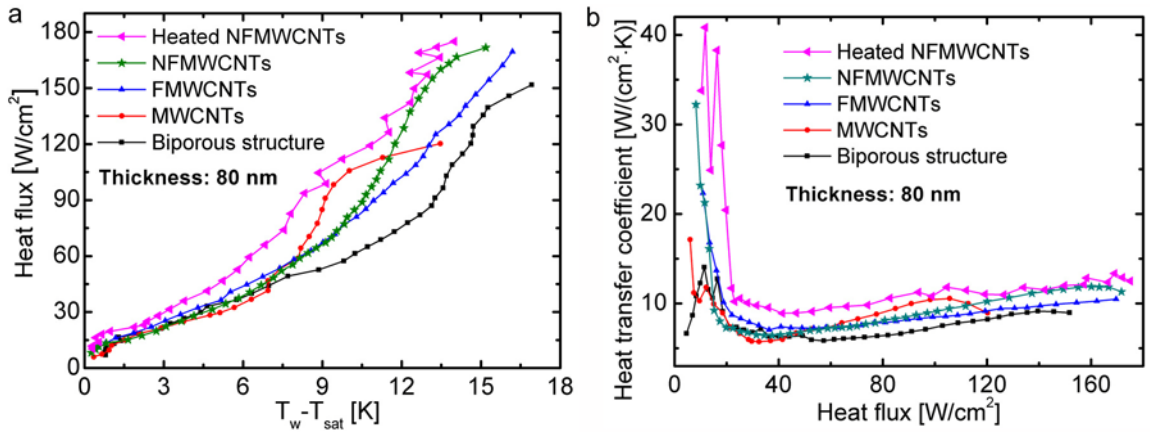

Figure 6.2 Capillary evaporation results for 80nm FMWCNT coatings. (a) ΔT-q" curves. (b) q"-h curves.

nanotube wires and the bondings between the coatings and substrates are significant since the bubble growth expansion forces were extremely high especially in the high heat flux regime. FMWCNT coatings could not be strongly attached on the substrates, hence, they might easily fall off due to the bubble growth expansion forces. Amphiphilic Nafion was able to strengthen the bonding between the FMWCNTs and substrates as well as the interactions of FMWCNT wires. Moreover, heating the FMWCNT coating at approximately 130 ^{o}C, above the glass transition temperature of Nafion for five minutes resulted in the inter-diffusion of polymer chains, which provided a greater degree of interlocking and Van der Waals interactions.

The coating thickness is also critical to the heat transfer performance. Increasing coating thickness yielded augmented nucleate site densities and surface areas, which are good for both nucleate boiling; however, the fluid flow is also hindered to enter into the bottom nanoscale cavities, resulting in thermally insulated nanoporous layer and extra thermal resistances. As shown in Figure 6.3a and b, NFMWCNTs with the thickness of 400 nm and 1600 nm were deposited and tested, respectively. The HTC enhancements were reached by 102.3% and 15.7%, respectively, at the heat flux of 151.7 W/cm^2. 400

nm coatings performed better than the 80 nm coatings since they induced more cavities and surface areas. 1600 nm coatings performed worse than 80 nm coatings because of the extra thermal resistances introduced by the porous layers. When the heat flux was less than 118.3 W/cm^2, local liquid supply was sufficient with the thickness of 1600 nm, yielding enhanced HTC due to the augmented nucleate site densities. However, when the heat flux reached higher than 118.3 W/cm^2, HTC decreased until CHF occurred. The possible reason is that the non-wetted porous layer becomes thicker, resulting in increasing thermal resistances. Nucleate boiling and evaporation occur only in top wetted structures. This indicates an optimal coating thickness exists to obtain an effective HTC enhancement.

To further investigate the HTC enhancement mechanism of the NFMWCNT coatings, conformal ALD SiO_2 coatings were deposited on the bi-porous structure to form intrinsically superhydrophilic interface [146] as a comparative study (Figure 6.3a and b). In the low heat flux region, the intrinsically superhydrophilic ALD SiO_2 and NFMWCNT coated bi-porous structures reached the HTC of 8.8 W/(cm^2·K) and 18.1 W/(cm^2·K), respectively, at the heat flux of 28.9 W/cm^2. In the high heat flux region, ALD SiO_2 coating reached a maximum HTC of 14.2 W/(cm^2·K), which was increased by 61.4% at the heat flux of 151.7 W/cm^2. Nonetheless, the enhancement was 102.3% for the 400 nm NFMWCNT coatings at the identical heat flux.

The evaporation process on the bare bi-porous structure can be divided into three regions (Figure 6.3b) [142]. Region I (0-11.2 W/cm^2) is dominated by the oscillating flow and nucleate boiling; region II (11.2-57.2 W/cm^2) is governed by the thin film evaporation and region III (57.2-152.2 W/cm^2) is determined by both nucleate boiling

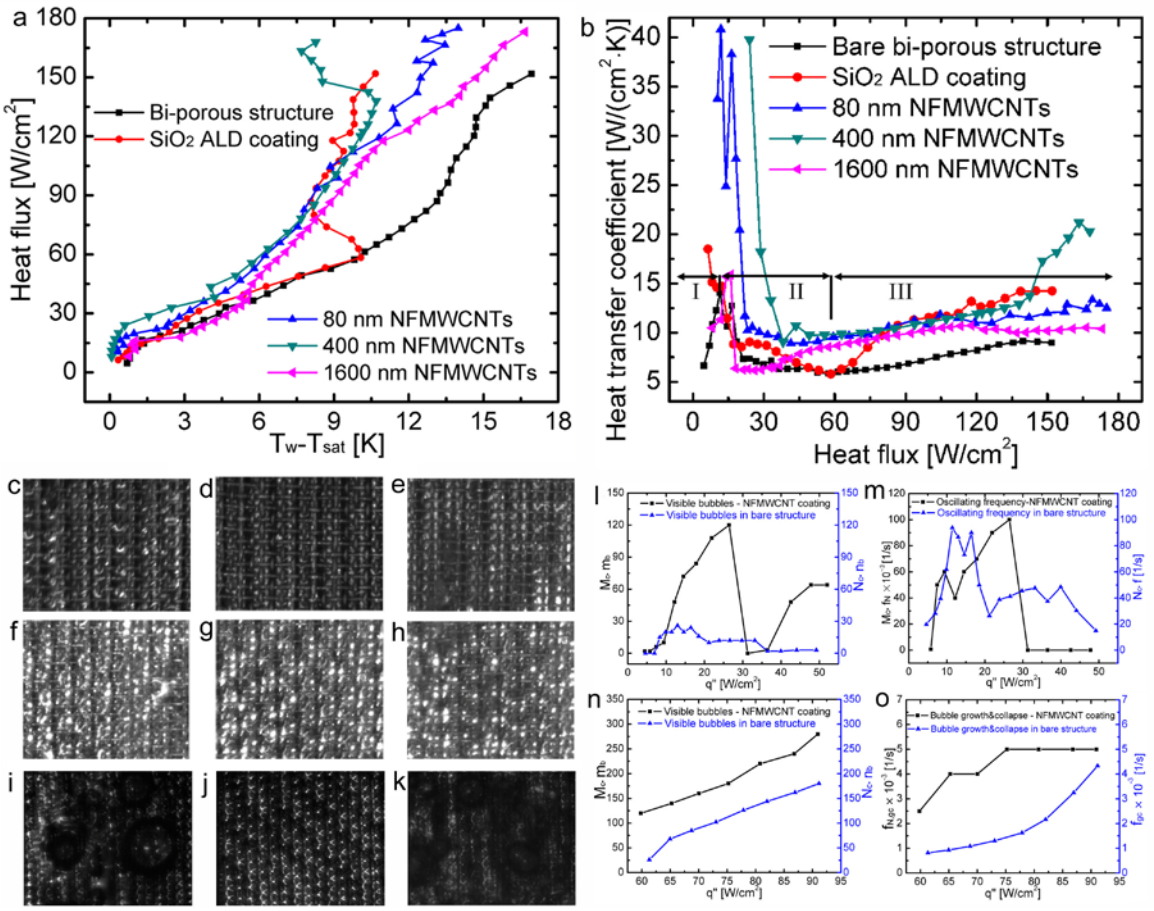

Figure 6.3 HTC enhancement mechanism. (a) ΔT-q" curves. (b) q"-h curves. (c-e) Liquid distributions in the bare wicks at the heat fluxes of 9.0, 40.4 and 61.4 W/cm^2, respectively. (f-h) Liquid distributions in the ALD SiO_2 coated hybrid wicks at the heat fluxes of 8.9, 40.1 and 61.5 W/cm^2, respectively. (i-k) Liquid distributions in the 400 nm NFMWCNT coated hybrid wicks at the heat fluxes of 9.1, 40.2 and 61.3 W/cm^2, respectively. (l) The total number of visible bubbles in active NFMWCNT coated channels, $M_c \cdot m_b$. M_c is the number of visible bubbles in a single active channel and m_b is the number of active channels. $N_c \cdot n_b$ is for the bare structure. (m) The total oscillating frequency, $M_c \cdot f_N$, in the NFMWCNT coated hybrid structures; M_c is the number of active channels and f_N is the frequency of fluid flow in a single active channel. $N_c \cdot f$ is for the bare structure. (n) The total number of visible bubbles in active channels, $M_c \cdot m_b$ in the high heat flux region. $N_c \cdot n_b$ is for bare structure. (o) Bubble growth and collapse frequency, $f_{N,gc}$. f_{gc} is for the bare structure.

and thin film evaporation. NFMWCNT coated interfaces show significantly higher HTC in region I than the bare and ALD SiO_2 coated structure. In this region, heat transfer was dominated by the nucleate boiling and oscillating flow in the unconfined bi-porous

structure. Good wetting conditions were maintained initially on both ALD SiO_2 and NFWMCNT coated bi-porous structures (Figure 6.3c, f and i), but the nanoscale porous NFMWCNTs could form a large amount of hydrophobic-hydrophilic cavities (Figure 6.1g) [146], which were ideal for nucleate boiling at the bottom wall of the microchannels. This substantially reduced the superheat of the microchannel. In addition, such nanoengineered interfaces dramatically increased the oscillating flow and advections (see Supplementary Video) since the nanoporous coatings were filled with water and form a well wetted layer for fluid flow, yielding a dramatically improved heat transfer on the single layer mesh. Hence, the overall HTC were significantly enhanced in region I. Visualization study validated that the nucleate boiling (Figure 6.3l) and oscillating frequency (Figure 6.3m) were both substantially enhanced by the nanoengineered coatings. In region II, the porous hydrophobic-hydrophilic coatings can still maintain good wetting conditions (Figure 6.3d, g and j), and thus the HTC was increased from 5.8 W/(cm^2·K) to 9.8 W/(cm^2·K) at the heat flux of 57.1 W/cm^2 due to the enhanced thin film evaporation. In region III, more nucleate sites can be initiated with the increasing superheat according to the nucleate boiling theory [83]. Maximum HTC reached 21.2 W/(cm^2·K) at the heat flux of 163.1 W/cm^2 (Figure 6.3b). It has been studied that conformal ALD SiO_2 coatings enhanced the wetting conditions and thin film evaporation [146]. 80 nm NFMWCNT coating performed worse than the ALD SiO_2 coating. Even though it provided more nucleate cavities than the conformal ALD coatings, NFMWCNT coatings took extra thermal resistances and deteriorated the thin film evaporation. However, 400 nm NFMWCNTs performed better than ALD SiO_2 coating. This is because thicker NFWMCNT coatings provide a large amount of cavities,

resulting in a significantly enhanced nucleate boiling heat transfer. Therefore, the HTC enhancement on the carbon nanotube enabled interfaces primarily resulted from the enhanced nucleate boiling in this region. Figure 6.3 n and o indicated that the nucleate site density and bubble growth and collapse frequency were both increased by the NFMCNT coatings.

CHF was decreased by the hydrophobic MWCNTs, while it could be increased by the hydrophobic-hydrophilic NFMWCNTs (Figure 6.2a). CHF was decreased from 151.7 W/cm^2 on bare structure to 120.3 W/cm^2 on the structure with hydrophobic MWCNT coatings, because of the lack of capillary driving forces. In contrast, NFMWCNTs can not only enhance the HTC but also increase the CHF from 151.7 W/cm^2 to more than 171.7 W/cm^2 on the three types of hydrophobic-hydrophilic NFMWCNT coatings (Figure 6.3a).

It has been studied that flow resistance is significant for liquid supply during the capillary evaporation process [142]. Conformal ALD SiO_2 coatings maintain the CHF (Figure 6.3a) because of the non-improved liquid supply, but NFMWCNTs are superior to the CHF enhancement due to the reduced flow resistance. NFMWCNTs can enhance the overall liquid supply as the superhydrophobic areas can decrease the flow resistance in microchannels and superhydrophilic functional groups significantly improved local wettability. Figure 4a shows that the wetting speed in the hybrid wick is significantly improved by the NFMWCNT coatings. The hybrid structure was visualized by a high speed camera and microscope assembly. Wetting tests show that the wetting speed in the microchannels of the FMWCNT coated hybrid structure is 3.27 cm/s, while it is 1.9 cm/s in the bare structure. Although the FMWCNTs take extra roughness, the hydrophobic

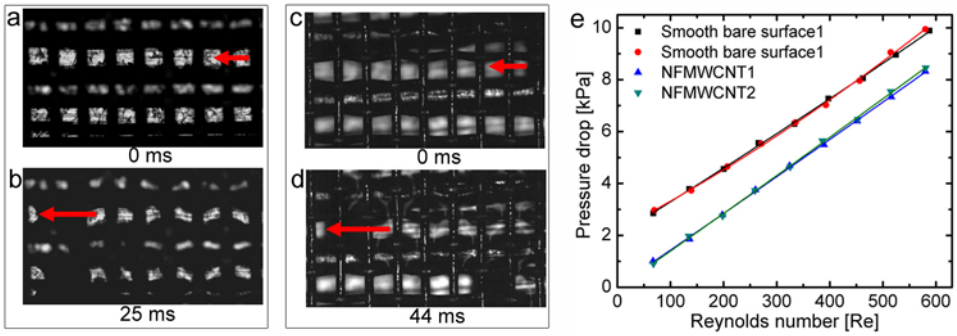

Figure 6.4 Characterization of the friction drag in the NFMWCNT coated hybrid wicks. (a, b) Wetting speed in the NFMWCNT coated hybrid wicks. (c, d) Wetting speed in the bare hybrid wicks. (e) Flow resistance measurement in the NFMWCNT coated microchannel.

cavities are filled with trapped air or vapor gases and water can not penetrate into the nanopores [97], resulting in improved fluid flow.

6.5 CHF ENHANCEMENT MECHANISM

Flow resistance was measured to further study the friction drag in the NFMWCNT coated smooth interface (Figure 6.4b). The flow resistance was reduced from 5.9 kPa to 4.2 kPa, which is 28.8%, at the Reynolds number of 300 (See supplementary in formation for flow resistance measurement). This validated the drag reduction and was consistent with the wetting speed test. The hydrophobic interface may induce boundary slip reduce friction drag [154]. The nanoporous interface with partial wetting areas can induce interfacial slippage due to the existence of nanobubbles [97]. Thus, the nanoengineered partially hydrophobic and partially hydrophilic interfaces could probably track some nanobubbles and induce boundary slip, yielding the reduce friction drag, which was good for the fluid flow and liquid supply. In addition, during the heat transfer process the hydrophobic-hydrophilic nanoporous interfaces could reduce the bubble size and increase the bubble growth and collapse frequency, which intensified fluid oscillations, resulting in improved fluid supply and CHF.

6.6 SUMMARY OF THE NANOENGINEERED HYBRID WICKS

In summary, the nanoengineered hydrophobic-hydrophilic interfaces are robust to enhance heat and mass transports. Hydrophobic-hydrophilic NFMWCNT coated hybrid wicks show enhanced capillary evaporation performances in both heat transfer and CHF. The increased HTC primarily resulted from the improved wetting conditions, oscillating fluid flow and augmented nucleate boiling; while the improved CHF resulted from the reduced friction drag and increased bubble growth and collapse frequency.

CHAPTER 7

CONCLUSIONS AND FUTURE STUDY

Surface roughness and interfacial wettability are two primary factors for two-phase heat and mass transports. Guided by Wenzel's effect, the apparent contact angles can be dramatically reduced by increasing surface roughness on hydrophilic surfaces. As a result, engineered surfaces with microscale, nanoscale, patterned and hierarchical structures have been employed to enhance boiling and evaporation. However, it is rather challenging to distinguish the effects of augmented surface roughness and the effect intrinsic wettability on heat transfer performance. The purpose of this study is to improve two-phase heat transport using nanoengineered interfaces with special wettability.

7.1 CONCLUSIONS

Intrinsically superhydrophilic TiO_2 coatings and partially hydrophobic and partially hydrophilic FMWCNTs were deposited on two layer micromeshes to enhance nucleate boiling. CHF can be effectively increased by the improved interfacial wettability because of the superwetting property. Ideal cavities were created by CNT-enabled hydrophobic-hydrophilic composite interfaces, resulting in augmented nucleate site density, increased bubble growth rate and improved bubble departure frequency. Therefore, both HTC and CHF were substantially enhanced.

The effect of interfacial wettability on boiling heat transfer was systematically studied. Intrinsically superhydrophilic surfaces can significantly increase the boiling CHF because of the superwetting property. Partially hydrophobic and partially hydrophilic

nanoporous media can create ideal cavities to enhance bubble dynamics. More hydrophobic surfaces yield higher HTC, while more hydrophilic surfaces result in higher CHF. The hydrophobic-hydrophilic interfaces perform better than the superhydrophobic interfaces in the boiling heat transfer.

Bio-inspired micromembrane-enhanced hybrid wicks effectively improve the CHF of capillary evaporation by increasing capillary forces and reducing flow resistance. Based on this newly developed hybrid wicks, intrinsically superhydrophilic SiO_2 coatings and partially hydrophobic and partially hydrophilic FMWCNTs were deposited on the micromembrane-enhanced hybrid wicks to enhance capillary evaporation. The improved wettability significantly improved the wetting conditions and thin film evaporation on micromembranes, resulting in dramatically increased HTC. FMWCNT coatings could reduce the friction drag due to the existence of "nanobubbles" and increase the wettability, yielding enhanced HTC and CHF simultaneously.

Surface structures and interfacial wettability were both studied to enhance capillary evaporation. High capillary pressure and low friction drag are critical to improve the liquid supply and increase evaporating CHF. The separation of capillary pressure generation and fluid flow result in significantly enhanced capillary evaporation. Improved interfacial wettability results in better wettings and thin film evaporation, which can dramatically increase the HTC. Nanoporous coatings with hydrophobic-hydrophilic wettabitiy can increase the capillary pressure, reduce the friction and create ideal heat transfer surfaces, resulting in enhanced HTC and CHF simultaneously.

Therefore, intrinsic interfacial wettability is critical for boiling and evaporation heat transfer. Improving the wettability could significantly increase the CHF of nucleate

boiling and enhance the HTC of capillary evaporation. The partially hydrophobic and partially hydrophobic functionalized carbon nanotubes can create ideal interfaces for nucleate boiling and reduce friction drag, resulting in enhanced HTC and CHF during boiling and evaporation.

7.2 FURTURE STUDY

7.2.1 CHF MECHANISM

Surface structures and interfacial wettability are significant for boiling and evaporation. This dissertation systematically studied the impact of interfacial wettability. However, further studies are needed to quantitatively define the effect to wettability on CHF mechanism of nucleate boiling.

Zuber considered the dynamic effects of vapor jets and developed the CHF model base on Taylor and Helmholtz instatiblities in 1959 [170]. As indicated in the correlation of CHF, $q_{Z,CHF} = \beta \cdot \rho_g^{0.5} h_{lg} [\sigma g(\rho_l - \rho_g)]^{0.25}$, where $q_{z,CHF}$ is the CHF predicted by Zuber's model; β is the constant; ρ_g is the vapor density; h_{lg} is the latent heat; σ is surface tension; g is the acceleration of gravity; ρ_l is the liquid density. This model is widely used to explain the CHF mechanism of boiling heat transfer on plain or structured surfaces. However, the impact of interfacial wettability, which was also critical for CHF, was not considered in this model.

Satish Kandlikar modified Zuber's model in 2001, considering the impact of interfacial wettability and surface orientation [171]. As indicated in Kandlikar's model, $q_{K,CHF} = q_{Z,CHF} \cdot (\frac{1+\cos\theta}{16})[\frac{2}{\pi} + \frac{\pi}{4}(1+\cos\theta)\cos\phi]^{0.5}$, where $q_{k,CHF}$ is the CHF predicted by Kandlikar's model, θ is the contact angle and φ is the tilted angle of the surface. This

model considered the contact angle and surface orientation, which was widely used in the boiling heat transfer area.

Most recently, Moo Hwan Kim found that Kandlikar's model could not explain the CHF mechanism when the micro/nanostructures were used and the contact angle is less than 10^o due to the liquid spreading effect [24]. Then Kandlikar's model was further modified to Kim's model, $q_{Kim,CHF} = q_{K,CHF} + q_{liquid\_spreading}$, where $q_{Kim,CHF}$ is the CHF predicated by Kim's model and $q_{liquid\_spreading}$ is the CHF contributed by liquid spreading.

However, no CHF model that considered the interfacial wettability was developed to explain the CHF enhancement in microporous media. There is no need to consider capillary effect in the previous models, but in porous structures capillary pressure should be dominated for liquid supply. Further study is needed to consider the capillary effect and develop a CHF model for the porous media.

7.2.2 HYDROPHOBIC-HYDROPHILIC SURFACES

This dissertation also developed partially hydrophobic and partially hydrophilic surfaces by functionalizing carbon nanotubes, resulting in significantly enhanced boiling and evaporation. This type of interface still needs to be further investigated to advance two-phase transport.

The hydrophobic cavity with hydrophilic surface was superior to HTC and CHF enhancement. However, the single bubble dynamics were not studied due to the difficulty in fabricating such an interface. Also, traditional bubble departure forces resulted from buoyancy force of vapor bubbles. If the bubble size can be reduced to nanoscale, buoyancy force may not play a critical role. Thus, bubble dynamics on nanoscale cavities can be studied to define the bubble size effect on CHF.

The hydrophobic-hydrophilic surfaces also exhibited significant advantages on fluid flow. When the capillary flow and Marangoni flow are in the direction, the drop motion can be advanced, resulting in advanced mass transport [94]. In addition, the nanoporous surfaces with partial wetting may track nanobubbles and yield significant drag reduction [172]. These fundamental studies may substantially advance fluid flow on solid-liquid interfaces.

REFERENCES

[1] S.V. Garimella, Advances in mesoscale thermal management technologies for microelectronics, Microelectr J, 37(11) (2006) 1165-1185.
[2] V.V. Viswanathan, D. Choi, D. Wang, W. Xu, S. Towne, R.E. Williford, J.-G. Zhang, J. Liu, Z. Yang, Effect of entropy change of lithium intercalation in cathodes and anodes on Li-ion battery thermal management, Journal of Power Sources, 195(11) (2010) 3720-3729.
[3] A. Faghri, Z. Guo, Challenges and opportunities of thermal management issues related to fuel cell technology and modeling, Int J Heat Mass Tran, 48(19-20) (2005) 3891-3920.
[4] C.-J. Weng, Advanced thermal enhancement and management of LED packages, International Communications in Heat and Mass Transfer, 36(3) (2009) 245-248.
[5] D.C. Price, A review of selected thermal management solutions for military electronic systems, Ieee Transactions on Components and Packaging Technologies, 26(1) (2003) 26-39.
[6] A. Rovira, M.J. Montes, M. Valdes, J.M. Martínez-Val, Energy management in solar thermal power plants with double thermal storage system and subdivided solar field, Applied Energy, 88(11) (2011) 4055-4066.
[7] B. Zalba, J.M. Marin, L.F. Cabeza, H. Mehling, Review on thermal energy storage with phase change: materials, heat transfer analysis and applications, Applied Thermal Engineering, 23(3) (2003) 251-283.
[8] I.C. Bang, J. Buongiorno, L.-W. Hu, H. Wang, Measurement of Key Pool Boiling Parameters in Nanofluids for Nuclear Applications, Journal of Power and Energy Systems, 2(1) (2008) 340-351.
[9] C. Li, Z. Wang, P.-I. Wang, Y. Peles, N. Koratkar, G.P. Peterson, Nanostructured copper interfaces for enhanced boiling, Small, 4(8) (2008) 1084-1088.
[10] K.-H. Chu, R. Enright, E.N. Wang, Structured surfaces for enhanced pool boiling heat transfer, Applied Physics Letters, 100(24) (2012) 241603-241604.
[11] Y. Nam, E. Aktinol, V.K. Dhir, Y.S. Ju, Single bubble dynamics on a superhydrophilic surface with artificial nucleation sites, International Journal of Heat and Mass Transfer, 54(7–8) (2011) 1572-1577.
[12] H.S. Ahn, C. Lee, J. Kim, M.H. Kim, The effect of capillary wicking action of micro/nano structures on pool boiling critical heat flux, International Journal of Heat and Mass Transfer, 55(1–3) (2012) 89-92.
[13] C. Li, G.P. Peterson, Y. Wang, Evaporation/boiling in thin capillary wicks (I) - Wick thickness effects, J. Heat Trans.-T. ASME, 128(12) (2006) 1312-1319.
[14] J.J. Wei, H. Honda, Effects of fin geometry on boiling heat transfer from silicon chips with micro-pin-fins immersed in FC-72, International Journal of Heat and Mass Transfer, 46(21) (2003) 4059-4070.

[15] S.G. Liter, M. Kaviany, Pool-boiling CHF enhancement by modulated porous-layer coating: theory and experiment, International Journal of Heat and Mass Transfer, 44(22) (2001) 4287-4311.
[16] D.H. Min, G.S. Hwang, Y. Usta, O.N. Cora, M. Koc, M. Kaviany, 2-D and 3-D modulated porous coatings for enhanced pool boiling, International Journal of Heat and Mass Transfer, 52(11–12) (2009) 2607-2613.
[17] C.H. Li, T. Li, P. Hodgins, C.N. Hunter, A.A. Voevodin, J.G. Jones, G.P. Peterson, Comparison study of liquid replenishing impacts on critical heat flux and heat transfer coefficient of nucleate pool boiling on multiscale modulated porous structures, International Journal of Heat and Mass Transfer, 54(15–16) (2011) 3146-3155.
[18] Y.Y. Hsu, ON THE SIZE RANGE OF ACTIVE NUCLEATION CAVITIES ON A HEATING SURFACE, Journal of Heat Transfer 84 (1962) 207-216.
[19] C.Y. Lee, B.J. Zhang, K.J. Kim, Morphological change of plain and nano-porous surfaces during boiling and its effect on nucleate pool boiling heat transfer, Experimental Thermal and Fluid Science, 40 (2012) 150-158.
[20] R. Chen, M.-C. Lu, V. Srinivasan, Z. Wang, H.H. Cho, A. Majumdar, Nanowires for Enhanced Boiling Heat Transfer, Nano Letters, 9(2) (2009) 548-553.
[21] A. Hee Seok, V. Sathyamurthi, D. Banerjee, Pool Boiling Experiments on a Nano-Structured Surface, Components and Packaging Technologies, IEEE Transactions on, 32(1) (2009) 156-165.
[22] S. Launay, A.G. Fedorov, Y. Joshi, A. Cao, P.M. Ajayan, Hybrid micro-nano structured thermal interfaces for pool boiling heat transfer enhancement, Microelectronics Journal, 37(11) (2006) 1158-1164.
[23] J.P. McHale, S.V. Garimella, T.S. Fisher, G.A. Powell, POOL BOILING PERFORMANCE COMPARISON OF SMOOTH AND SINTERED COPPER SURFACES WITH AND WITHOUT CARBON NANOTUBES, Nanoscale and Microscale Thermophysical Engineering, 15(3) (2011) 133-150.
[24] H.S. Ahn, H.J. Jo, S.H. Kang, M.H. Kim, Effect of liquid spreading due to nano/microstructures on the critical heat flux during pool boiling, Applied Physics Letters, 98(7) (2011) 071908.
[25] R.N. Wenzel, RESISTANCE OF SOLID SURFACES TO WETTING BY WATER, Industrial & Engineering Chemistry, 28(8) (1936) 988-994.
[26] H.T. Phan, N. Caney, P. Marty, S. Colasson, J. Gavillet, How does surface wettability influence nucleate boiling?, Comptes Rendus Mécanique, 337(5) (2009) 251-259.
[27] B. Bourdon, R. Rioboo, M. Marengo, E. Gosselin, J. De Coninck, Influence of the Wettability on the Boiling Onset, Langmuir, 28(2) (2011) 1618-1624.
[28] H. Jo, S. Kim, H. Kim, J. Kim, M.H. Kim, Nucleate boiling performance on nano/microstructures with different wetting surfaces, Nanoscale Research Letters, 7 (2012).
[29] Y. Takata, S. Hidaka, J.M. Cao, T. Nakamura, H. Yamamoto, M. Masuda, T. Ito, Effect of surface wettability on boiling and evaporation, Energy, 30(2–4) (2005) 209-220.
[30] B. Feng, K. Weaver, G.P. Peterson, Enhancement of critical heat flux in pool boiling using atomic layer deposition of alumina, Applied Physics Letters, 100(5) (2012) 053120-053123.

[31] K.S. Udell, Heat-transfer in porous-media heated from above with evaporation, condensation, and capillary effects, J. Heat Trans.-T. ASME, 105(3) (1983) 485-492.
[32] R.J. McGlen, R. Jachuck, S. Lin, Integrated thermal management techniques for high power electronic devices, Appl. Therm. Eng. , 24(8–9) (2004) 1143-1156.
[33] Y.F. Maydanik, Loop heat pipes, Appl. Therm. Eng. , 25(5-6) (2005) 635-657.
[34] D.H. Min, G.S. Hwang, M. Kaviany, Multi-artery, heat-pipe spreader, Int. J. Heat Mass Transf., 52(3–4) (2009) 629-635.
[35] G.S. Hwang, M. Kaviany, W.G. Anderson, J. Zuo, Modulated wick heat pipe, Int. J. Heat Mass Transf., 50(7–8) (2007) 1420-1434.
[36] Q.J. Cai, C.L. Chen, Design and Test of Carbon Nanotube Biwick Structure for High-Heat-Flux Phase Change Heat Transfer, J Heat Trans-T ASME, 132(5) (2010).
[37] J.A. Weibel, S.V. Garimella, M.T. North, Characterization of evaporation and boiling from sintered powder wicks fed by capillary action, Int. J. Heat Mass Transf., 53(19-20) (2010) 4204-4215.
[38] A.J. Jiao, H.B. Ma, J.K. Critser, Evaporation heat transfer characteristics of a grooved heat pipe with micro-trapezoidal grooves, International Journal of Heat and Mass Transfer, 50(15-16) (2007) 2905-2911.
[39] M.A. Hanlon, H.B. Ma, Evaporation heat transfer in sintered porous media, J. Heat Trans.-T. ASME, 125(4) (2003) 644-652.
[40] S.-C. Wong, J.-H. Liou, C.-W. Chang, Evaporation resistance measurement with visualization for sintered copper-powder evaporator in operating flat-plate heat pipes, Int J Heat Mass Tran, 53(19-20) (2010) 3792-3798.
[41] A. Brautsch, P.A. Kew, Examination and visualisation of heat transfer processes during evaporation in capillary porous structures, Appl. Therm. Eng. , 22(7) (2002) 815-824.
[42] J. Wu, B. Yu, A fractal resistance model for flow through porous media, Int J Heat Mass Tran, 50(19-20) (2007) 3925-3932.
[43] M.J. Fuerstman, A. Lai, M.E. Thurlow, S.S. Shevkoplyas, H.A. Stone, G.M. Whitesides, The pressure drop along rectangular microchannels containing bubbles, Lab on a Chip, 7(11) (2007) 1479-1489.
[44] W.T. Wu, J.F. Liu, W.J. Li, W.H. Hsieh, Measurement and correlation of hydraulic resistance of flow through woven metal screens, Int J Heat Mass Tran, 48(14) (2005) 3008-3017.
[45] D. Khrustalev, A. Faghri, Heat-transfer during evaporation on capillary-grooved structures of heat pipes, J. Heat Trans.-T. ASME, 117(3) (1995) 740-747.
[46] X. Xu, V.P. Carey, Film Evaporation from a Micro-Grooved Surface-An Approximate Heat Transfer Model and Its Comparison with Experimental Data, J. Thermophys Heat Transfer 4(4) (1990) 512-520.
[47] C.J. Morris, F.K. Forster, Oscillatory flow in microchannels - Comparison of exact and approximate impedance models with experiments, Exp Fluids, 36(6) (2004) 928-937.
[48] J. Wang, I. Catton, Evaporation heat transfer in thin biporous media, Heat and Mass Transfer, 37(2-3) (2001) 275-281.
[49] T. Semenic, Y.Y. Lin, I. Catton, D.B. Sarraf, Use of biporous wicks to remove high heat fluxes, Appl. Therm. Eng., 28(4) (2008) 278-283.
[50] T. Semenic, Y.-Y. Lin, I. Catton, Thermophysical Properties of Biporous Heat Pipe Evaporators, Journal of Heat Transfer, 130(2) (2008) 022602.

[51] T. Semenic, I. Catton, Experimental study of biporous wicks for high heat flux applications, Int J Heat Mass Tran, 52(21-22) (2009) 5113-5121.
[52] M.C. Lu, J.Y. Chang, A. Majumdar, Enhanced Heat Transfer in Biporous Wicks in the Thin Liquid Film Evaporation and Boiling Regimes, (2012).
[53] X.L. Cao, P. Cheng, T.S. Zhao, Experimental study of evaporative heat transfer in sintered copper bidispersed wick structures, J. Thermophys Heat Transfer 16(4) (2002) 547-552.
[54] D. Ćoso, V. Srinivasan, M.C. Lu, J.Y. Chang, A. Majumdar, Enhanced Heat Transfer in Biporous Wicks in the Thin Liquid Film Evaporation and Boiling Regimes, J. Heat Transfer 134 (2012) 101501.
[55] X. Dai, L. Tran, F. Yang, B. Shi, R. Yang, Y.C. Lee, C. Li, Characterization of Hybrid-Wicked Copper Heat Pipe, ASME Conference Proceedings, 2011(38921) T30005.
[56] M.T. North, D.B. Sarraf, J.H. Rosenfeld, Y.F. Maidanik, S. Vershinin, High heat flux loop heat pipes, AIP Conference Proceedings, 387(1) (1997) 561-566.
[57] C.-C. Yeh, C.-N. Chen, Y.-M. Chen, Heat transfer analysis of a loop heat pipe with biporous wicks, Int. J. Heat Mass Transf., 52(19–20) (2009) 4426-4434.
[58] D.L. Damm, A.G. Fedorov, Radiation heat transfer in SOFC materials and components, J Power Sources, 143(1-2) (2005) 158-165.
[59] J.M. Koo, S. Im, L.N. Jiang, K.E. Goodson, Integrated microchannel cooling for three-dimensional electronic circuit architectures, J Heat Trans-T ASME, 127(1) (2005) 49-58.
[60] K. Kordas, G. Toth, P. Moilanen, M. Kumpumaki, J. Vahakangas, A. Uusimaki, R. Vajtai, P.M. Ajayan, Chip cooling with integrated carbon nanotube microfin architectures, Appl Phys Lett, 90(12) (2007).
[61] D.G. Norton, E.D. Wetzel, D.G. Vlachos, Thermal management in catalytic microreactors, Ind Eng Chem Res, 45(1) (2006) 76-84.
[62] L. Song, J.W. Evans, Electrochemical-thermal model of lithium polymer batteries, J Electrochem Soc, 147(6) (2000) 2086-2095.
[63] E.M. Landis, Capillary pressure and capillary permeability, Physiol Rev, 14(3) (1934) 0404-0481.
[64] S.J. Kim, I.C. Bang, J. Buongiorno, L.W. Hu, Surface wettability change during pool boiling of nanofluids and its effect on critical heat flux, Int J Heat Mass Tran, 50(19-20) (2007) 4105-4116.
[65] S.J. Kim, I.C. Bang, J. Buongiorno, L.W. Hu, Effects of nanoparticle deposition on surface wettability influencing boiling heat transfer in nanofluids, Appl Phys Lett, 89(15) (2006).
[66] A.R. Betz, J. Xu, H. Qiu, D. Attinger, Do surfaces with mixed hydrophilic and hydrophobic areas enhance pool boiling?, Appl Phys Lett, 97(14) (2010) 141909-141903.
[67] A.R. Betz, J. Jenkins, C.-J.C. Kim, D. Attinger, Boiling heat transfer on superhydrophilic, superhydrophobic, and superbiphilic surfaces, Int J Heat Mass Tran, 57(2) (2013) 733-741.
[68] N.R. Jana, C. Earhart, J.Y. Ying, Synthesis of water-soluble and functionalized nanoparticles by silica coating, Chemistry of Materials, 19(21) (2007) 5074-5082.
[69] Y. Takata, S. Hidaka, J.M. Cao, T. Nakamura, H. Yamamoto, M. Masuda, T. Ito, Effect of surface wettability on boiling and evaporation, Energy, 30(2-4) (2005) 209-220.

[70] J.S. Coursey, J. Kim, Nanofluid boiling: The effect of surface wettability, Int J Heat Fluid Fl, 29(6) (2008) 1577-1585.
[71] P. Vassallo, R. Kumar, S. D'Amico, Pool boiling heat transfer experiments in silica-water nano-fluids, Int. J. Heat Mass Transf., 47(2) (2004) 407-411.
[72] S.M. You, J.H. Kim, K.H. Kim, Effect of nanoparticles on critical heat flux of water in pool boiling heat transfer, Appl Phys Lett, 83(16) (2003) 3374-3376.
[73] B. Feng, K. Weaver, G.P. Peterson, Enhancement of critical heat flux in pool boiling using atomic layer deposition of alumina, Appl Phys Lett, 100(5) (2012) 053120.
[74] D.S. Wen, Y.L. Ding, Experimental investigation into the pool boiling heat transfer of aqueous based gamma-alumina nanofluids, Journal of Nanoparticle Research, 7(2-3) (2005) 265-274.
[75] R.A. Taylor, P.E. Phelan, Pool boiling of nanofluids: Comprehensive review of existing data and limited new data, Int J Heat Mass Tran, 52(23-24) (2009) 5339-5347.
[76] A.I. Abdulagatov, Y. Yan, J.R. Cooper, Y. Zhang, Z.M. Gibbs, A.S. Cavanagh, R.G. Yang, Y.C. Lee, S.M. George, Al2O3 and TiO2 Atomic Layer Deposition on Copper for Water Corrosion Resistance, ACS Applied Materials & Interfaces, 3(12) (2011) 4593-4601.
[77] S.J. kline, F.A. McClintock, Describing Uncertainties in Single-Sample Experiments, Mech. Eng., 75 (1953) 3-8.
[78] J.W. Elam, M.D. Groner, S.M. George, Viscous flow reactor with quartz crystal microbalance for thin film growth by atomic layer deposition, Rev Sci Instrum, 73(8) (2002) 2981-2987.
[79] R.L. Puurunen, Surface chemistry of atomic layer deposition: A case study for the trimethylaluminum/water process, J Appl Phys, 97(12) (2005) 121301-121352.
[80] M. Ritala, M. Leskela, E. Rauhala, Atomic layer epitaxy growth of titanium dioxide thin films from titanium ethoxide, Chemistry of Materials, 6(4) (1994) 556-561.
[81] B.B. Burton, M.P. Boleslawski, A.T. Desombre, S.M. George, Rapid SiO2 Atomic Layer Deposition Using Tris(tert-pentoxy)silanol, Chemistry of Materials, 20(22) (2008) 7031-7043.
[82] Y. Nam, S. Sharratt, G. Cha, Y. Ju, Characterization and Modeling of the Heat Transfer Performance of Nanostructured Cu Micropost Wicks, J Heat Trans-T ASME, 133(10) (2011).
[83] Y.Y. Hsu, On the size range of active nucleation cavities on a heating surface, J. Heat Trans.-T ASME, 84 (1962) 207-216.
[84] C. Gerardi, J. Buongiorno, L.-w. Hu, T. McKrell, Study of bubble growth in water pool boiling through synchronized, infrared thermometry and high-speed video, Int J Heat Mass Tran, 53(19–20) (2010) 4185-4192.
[85] C. Li, G.P. Peterson, Evaporation/boiling in thin capillary wicks (II) - Effects of volumetric porosity and mesh size, J Heat Trans-T ASME, 128(12) (2006) 1320-1328.
[86] T. Kumada, H. Sakashita, POOL BOILING HEAT-TRANSFER .2. THICKNESS OF LIQUID MACROLAYER FORMED BENEATH VAPOR MASSES, Int J Heat Mass Tran, 38(6) (1995) 979-987.
[87] T.G. Theofanous, T.N. Dinh, J.P. Tu, A.T. Dinh, The boiling crisis phenomenon: Part II: dryout dynamics and burnout, Exp Therm Fluid Sci, 26(6–7) (2002) 793-810.
[88] N. Zuber, HYDRODYNAMIC ASPECTS OF BOILING HEAT TRANSFER (thesis), University of California, Los Angeles, Los Angeles, 1959.

[89] A.K. Das, P.K. Das, P. Saha, Heat transfer during pool boiling based on evaporation from micro and macrolayer, Int J Heat Mass Tran, 49(19-20) (2006) 3487-3499.
[90] Y.Y. Hsu, On the size range of active nucleation cavities on a heating surface, Journal of Heat Transfer, 84 (1962) 207-216.
[91] N.A. Patankar, Supernucleating surfaces for nucleate boiling and dropwise condensation heat transfer, Soft Matter, 6(8) (2010) 1613-1620.
[92] D. Chandler, Interfaces and the driving force of hydrophobic assembly, Nature, 437(7059) (2005) 640-647.
[93] E. Martines, K. Seunarine, H. Morgan, N. Gadegaard, C.D.W. Wilkinson, M.O. Riehle, Superhydrophobicity and Superhydrophilicity of Regular Nanopatterns, Nano Letters, 5(10) (2005) 2097-2103.
[94] S. Daniel, M.K. Chaudhury, J.C. Chen, Fast Drop Movements Resulting from the Phase Change on a Gradient Surface, Science, 291(5504) (2001) 633-636.
[95] D.T. Wasan, A.D. Nikolov, H. Brenner, Droplets Speeding on Surfaces, Science, 291(5504) (2001) 605-606.
[96] N. Miljkovic, R. Enright, E.N. Wang, Effect of Droplet Morphology on Growth Dynamics and Heat Transfer during Condensation on Superhydrophobic Nanostructured Surfaces, ACS Nano, 6(2) (2012) 1776-1785.
[97] C. Cottin-Bizonne, J.-L. Barrat, L. Bocquet, E. Charlaix, Low-friction flows of liquid at nanopatterned interfaces, Nat. Mater., 2(4) (2003) 237-240.
[98] Z.-G. Guo, W.-M. Liu, Sticky superhydrophobic surface, Appl Phys Lett, 90(22) (2007) 223111.
[99] M.H. Jin, X.J. Feng, L. Feng, T.L. Sun, J. Zhai, T.J. Li, L. Jiang, Superhydrophobic aligned polystyrene nanotube films with high adhesive force, Advanced Materials, 17(16) (2005) 1977-+.
[100] A.R. Betz, J. Xu, H. Qiu, D. Attinger, Do surfaces with mixed hydrophilic and hydrophobic areas enhance pool boiling?, Appl Phys Lett, 97(14) (2010) 141909.
[101] A.S. Klymchenko, S. Furukawa, K. Müllen, M. Van der Auweraer, S. De Feyter, Supramolecular Hydrophobic−Hydrophilic Nanopatterns at Electrified Interfaces, Nano Letters, 7(3) (2007) 791-795.
[102] E.T. Thostenson, Z.F. Ren, T.W. Chou, Advances in the science and technology of carbon nanotubes and their composites: a review, Composites Science and Technology, 61(13) (2001) 1899-1912.
[103] S.L. Mielke, D. Troya, S. Zhang, J.L. Li, S.P. Xiao, R. Car, R.S. Ruoff, G.C. Schatz, T. Belytschko, The role of vacancy defects and holes in the fracture of carbon nanotubes, Chemical Physics Letters, 390(4-6) (2004) 413-420.
[104] Y. Fan, B.R. Goldsmith, P.G. Collins, Identifying and counting point defects in carbon nanotubes, Nat Mater, 4(12) (2005) 906-911.
[105] S. Berber, Y.K. Kwon, D. Tomanek, Unusually high thermal conductivity of carbon nanotubes, Phys. Rev. Lett., 84(20) (2000) 4613-4616.
[106] P. Qi, O. Vermesh, M. Grecu, A. Javey, Q. Wang, H. Dai, S. Peng, K.J. Cho, Toward Large Arrays of Multiplex Functionalized Carbon Nanotube Sensors for Highly Sensitive and Selective Molecular Detection, Nano Letters, 3(3) (2003) 347-351.
[107] S. Agrawal, M.S. Raghuveer, H. Li, G. Ramanath, Defect-induced electrical conductivity increase in individual multiwalled carbon nanotubes, Appl Phys Lett, 90(19) (2007) 193104.

[108] J.-P. Tessonnier, A. Villa, O. Majoulet, D.S. Su, R. Schlögl, Defect-Mediated Functionalization of Carbon Nanotubes as a Route to Design Single-Site Basic Heterogeneous Catalysts for Biomass Conversion, Angewandte Chemie International Edition, 48(35) (2009) 6543-6546.
[109] Y. Lu, S. Bangsaruntip, X. Wang, L. Zhang, Y. Nishi, H. Dai, DNA Functionalization of Carbon Nanotubes for Ultrathin Atomic Layer Deposition of High κ Dielectrics for Nanotube Transistors with 60 mV/Decade Switching, Journal of the American Chemical Society, 128(11) (2006) 3518-3519.
[110] J. Wang, M. Musameh, Y. Lin, Solubilization of Carbon Nanotubes by Nafion toward the Preparation of Amperometric Biosensors, Journal of the American Chemical Society, 125(9) (2003) 2408-2409.
[111] A. Felten, C. Bittencourt, J.J. Pireaux, G. Van Lier, J.C. Charlier, Radio-frequency plasma functionalization of carbon nanotubes surface O-2, NH3, and CF4 treatments, J Appl Phys, 98(7) (2005) 074308.
[112] K. Balasubramanian, M. Burghard, Chemically functionalized carbon nanotubes, Small, 1(2) (2005) 180-192.
[113] K.K.S. Lau, J. Bico, K.B.K. Teo, M. Chhowalla, G.A.J. Amaratunga, W.I. Milne, G.H. McKinley, K.K. Gleason, Superhydrophobic carbon nanotube forests, Nano Letters, 3(12) (2003) 1701-1705.
[114] A.B.D. Cassie, S. Baxter, Wettability of porous surfaces, Transactions of the Faraday Society, 40 (1944) 546-551.
[115] S. Boduroglu, M. Cetinkaya, W.J. Dressick, A. Singh, M.C. Demirel, Controlling the Wettability and adhesion of nanostructured poly-(p-xylylene) films, Langmuir, 23(23) (2007) 11391-11395.
[116] A. Lafuma, D. Quere, Superhydrophobic states, Nature Materials, 2(7) (2003) 457-460.
[117] S. Lee, J.-W. Peng, C.-H. Liu, Probing plasma-induced defect formation and oxidation in carbon nanotubes by Raman dispersion spectroscopy, Carbon, 47(15) (2009) 3488-3497.
[118] C.J. Vanoss, Hydrophobic, hydrophilic and other interactions in epitope-paratope binding, Mol Immunol, 32(3) (1995) 199-211.
[119] E.T. Mickelson, C.B. Huffman, A.G. Rinzler, R.E. Smalley, R.H. Hauge, J.L. Margrave, Fluorination of single-wall carbon nanotubes, Chem Phys Lett, 296(1-2) (1998) 188-194.
[120] V.N. Khabashesku, W.E. Billups, J.L. Margrave, Fluorination of single-wall carbon nanotubes and subsequent derivatization reactions, Accounts Chem Res, 35(12) (2002) 1087-1095.
[121] H.B. Ma, C. Wilson, B. Borgmeyer, K. Park, Q. Yu, S.U.S. Choi, M. Tirumala, Effect of nanofluid on the heat transport capability in an oscillating heat pipe, Appl. Phys. Lett., 88(14) (2006).
[122] S. Ergun, Fluid flow through packed columns, Chem Eng Prog, 48(2) (1952) 89-94.
[123] C. Li, G.P. Peterson, The effective thermal conductivity of wire screen, Int. J. Heat Mass Transf., 49(21-22) (2006) 4095-4105.
[124] W.L. Qu, I. Mudawar, Measurement and prediction of pressure drop in two-phase micro-channel heat sinks, Int. J. Heat Mass Transf., 46(15) (2003) 2737-2753.

[125] P.C. Reeves, M.A. Celia, A Functional Relationship Between Capillary Pressure, Saturation, and Interfacial Area as Revealed by a Pore-Scale Network Model, Water Resour Res, 32(8) (1996) 2345-2358.
[126] Q. Wang, B. Mazé, H.V. Tafreshi, B. Pourdeyhimi, A note on permeability simulation of multifilament woven fabrics, Chem. Eng. Sci. , 61(24) (2006) 8085-8088.
[127] M. Eroglu, T.I. Khan, N. Orhan, Diffusion bonding between Ti-6Al-4V alloy and microduplex stainless steel with copper interlayer, Materials Science and Technology, 18(1) (2002) 68-72.
[128] R. Xiao, K.-H. Chu, E.N. Wang, Multilayer liquid spreading on superhydrophilic nanostructured surfaces, Appl. Phys. Lett. , 94(19) (2009) 193104.
[129] M. Toiya, J. Stambaugh, W. Losert, Transient and oscillatory granular shear flow, Phys. Rev. Lett. , 93(8) (2004).
[130] K.C. Leong, L.W. Jin, An experimental study of heat transfer in oscillating flow through a channel filled with an aluminum foam, Int. J. Heat Mass Transf., 48(2) (2005) 243-253.
[131] S. Herminghaus, M. Brinkmann, R. Seemann, Wetting and dewetting of complex surface geometries, Annual Review of Materials Research, 38 (2008) 101-121.
[132] R.N. Wenzel, Surface Roughness and Contact Angle, The Journal of Physical and Colloid Chemistry, 53(9) (1948) 1466-1467.
[133] K.-H. Chu, Y.S. Joung, R. Enright, C.R. Buie, E.N. Wang, Hierarchically structured surfaces for boiling critical heat flux enhancement, Applied Physics Letters, 102(15) (2013) 151602-151604.
[134] P.K. Jal, S. Patel, B. Mishra, Chemical modification of silica surface by immobilization of functional groups for extractive concentration of metal ions, Talanta, 62(5) (2004) 1005-1028.
[135] E.-P. Ng, S. Mintova, Nanoporous materials with enhanced hydrophilicity and high water sorption capacity, Microporous and Mesoporous Materials, 114(1-3) (2008) 1-26.
[136] H.T. Phan, N. Caney, P. Marty, S. Colasson, J. Gavillet, How does surface wettability influence nucleate boiling?, Comptes Rendus Mecanique, 337(5) (2009) 251-259.
[137] W. Wu, H. Bostanci, L.C. Chow, Y. Hong, M. Su, J.P. Kizito, Nucleate boiling heat transfer enhancement for water and FC-72 on titanium oxide and silicon oxide surfaces, Int. J. Heat Mass Transf., 53(9-10) (2010) 1773-1777.
[138] S.M. George, Atomic Layer Deposition: An Overview, Chemical Reviews, 110(1) (2010) 111-131.
[139] J.W. Elam, D. Routkevitch, P.P. Mardilovich, S.M. George, Conformal coating on ultrahigh-aspect-ratio nanopores of anodic alumina by atomic layer deposition, Chemistry of Materials, 15(18) (2003) 3507-3517.
[140] B. Kuznicka, Erosion-corrosion of heat exchanger tubes, Engineering Failure Analysis, 16(7) (2009) 2382-2387.
[141] N. Boulay, M. Edwards, Role of temperature, chlorine, and organic matter in copper corrosion by-product release in soft water, Water Research, 35(3) (2001) 683-690.
[142] X. Dai, F. Yang, Y.-C. Lee, R. Yang, C. Li, Micromembrane-enhanced Capillary Evaporation Int. J. Heat Mass Transf., (2013) In press.
[143] P. Luzeau, X.Z. Xu, M. Lagues, N. Hess, J.P. Contour, M. Nanot, F. Queyroux, M. Touzeau, D. Pagnon, COPPER-OXIDE THIN-FILM GROWTH USING AN OXYGEN

PLASMA SOURCE, Journal of Vacuum Science & Technology a-Vacuum Surfaces and Films, 8(6) (1990) 3938-3940.
[144] X. Dai, F. Yang, Y.-C. Lee, R. Yang, C. Li, Micromembrane Enhanced Capillary Evaporation Int. J. Heat Mass Transf., (2013) In review.
[145] Y.Y. Hsu, On the size range of active nucleation cavities on a heating surface, J Heat Trans-T ASME, 84 (1962) 207-216.
[146] X. Dai, X. Huang, F. Yang, X. Li, J. Sightler, Y. Yang, C. Li, Enhanced nucleate boiling on horizontal hydrophobic-hydrophilic carbon nanotube coatings, Appl Phys Lett, 102(16) (2013) 161605-161605.
[147] R. Xiao, K.-H. Chu, E.N. Wang, Multilayer liquid spreading on superhydrophilic nanostructured surfaces, Appl Phys Lett, 94(19) (2009) 193104-193103.
[148] E.W. Washburn, The dynamics of capillary flow, Physical Review, 17(3) (1921) 273-283.
[149] A.A. Darhuber, S.M. Troian, W.W. Reisner, Dynamics of capillary spreading along hydrophilic microstripes, Physical Review E, 64(3) (2001) art. no.-031603.
[150] F. Heslot, A.M. Cazabat, P. Levinson, N. Fraysse, Experiments on wetting on the scale of nanometers: Influence of the surface energy, Phys Rev Lett, 65(5) (1990) 599-602.
[151] A.J. Jiao, H.B. Ma, J.K. Critser, Evaporation heat transfer characteristics of a grooved heat pipe with micro-trapezoidal grooves, Int J Heat Mass Tran, 50(15–16) (2007) 2905-2911.
[152] Y. Nam, E. Aktinol, V.K. Dhir, S. Ju, Single bubble dynamics on a superhydrophilic surface with artificial nucleation sites, Int. J. Heat Mass Transf., 54(7-8) (2011) 1572-1577.
[153] H.Y. Wu, P. Cheng, An experimental study of convective heat transfer in silicon microchannels with different surface conditions, Int J Heat Mass Tran, 46(14) (2003) 2547-2556.
[154] C. Neto, D.R. Evans, E. Bonaccurso, H.J. Butt, V.S.J. Craig, Boundary slip in Newtonian liquids: a review of experimental studies, Rep Prog Phys, 68(12) (2005) 2859-2897.
[155] C. Cottin-Bizonne, B. Cross, A. Steinberger, E. Charlaix, Boundary slip on smooth hydrophobic surfaces: Intrinsic effects and possible artifacts, Phys Rev Lett, 94(5) (2005).
[156] P. Tsai, A.M. Peters, C. Pirat, M. Wessling, R.G.H. Lammertink, D. Lohse, Quantifying effective slip length over micropatterned hydrophobic surfaces, Phys Fluids, 21(11) (2009).
[157] S. Iijima, Helical microtubules of graphitic carbon, Nature, 354(6348) (1991) 56-58.
[158] S. Ujereh, T. Fisher, I. Mudawar, Effects of carbon nanotube arrays on nucleate pool boiling, Int J Heat Mass Tran, 50(19-20) (2007) 4023-4038.
[159] V. Sathyamurthi, H.S. Ahn, D. Banerjee, S.C. Lau, Subcooled Pool Boiling Experiments on Horizontal Heaters Coated With Carbon Nanotubes, J Heat Trans-T ASME, 131(7) (2009).
[160] K.-J. Park, D. Jung, Enhancement of nucleate boiling heat transfer using carbon nanotubes, Int J Heat Mass Tran, 50(21-22) (2007) 4499-4502.

[161] V. Khanikar, I. Mudawar, T. Fisher, Effects of carbon nanotube coating on flow boiling in a micro-channel, Int J Heat Mass Tran, 52(15-16) (2009) 3805-3817.
[162] N. Singh, V. Sathyamurthy, W. Peterson, J. Arendt, D. Banerjee, Flow boiling enhancement on a horizontal heater using carbon nanotube coatings, Int J Heat Fluid Fl, 31(2) (2010) 201-207.
[163] Q. Cai, C.-L. Chen, Design and Test of Carbon Nanotube Biwick Structure for High-Heat-Flux Phase Change Heat Transfer, J Heat Trans-T ASME, 132(5) (2010).
[164] E. Terrado, R. Molina, E. Natividad, M. Castro, P. Erra, D. Mishkinis, A. Torres, M.T. Martinez, Modifying the Heat Transfer and Capillary Pressure of Loop Heat Pipe Wicks with Carbon Nanotubes, Journal of Physical Chemistry C, 115(19) (2011) 9312-9319.
[165] H.S. Xue, J.R. Fan, R.H. Hong, Y.C. Hu, Characteristic boiling curve of carbon nanotube nanofluid as determined by the transient calorimeter technique, Appl Phys Lett, 90(18) (2007).
[166] M. Horton, H. Hong, C. Li, B. Shi, G.P. Peterson, S. Jin, Magnetic alignment of Ni-coated single wall carbon nanotubes in heat transfer nanofluids, J Appl Phys, 107(10) (2010).
[167] K.-J. Park, D. Jung, S.E. Shim, Nucleate boiling heat transfer in aqueous solutions with carbon nanotubes up to critical heat fluxes, Int J Multiphas Flow, 35(6) (2009) 525-532.
[168] G. Nagayama, P. Cheng, Effects of interface wettability on microscale flow by molecular dynamics simulation, Int J Heat Mass Tran, 47(3) (2004) 501-513.
[169] B. Zhao, J.S. Moore, D.J. Beebe, Surface-Directed Liquid Flow Inside Microchannels, Science, 291(5506) (2001) 1023-1026.
[170] N. Zuber, Hydrodynamic Aspects of Boiling Heat Transfer, Ph.D. thesis (1959), Research Laboratory, Los Angeles and Ramo-Wooldridge Corporation, University of California, Los Angeles, CA.
[171] S.G. Kandlikar, A Theoretical Model to Predict Pool Boiling CHF Incorporating Effects of Contact Angle and Orientation, Journal of Heat Transfer, 123(6) (2001) 1071-1079.
[172] C. Cottin-Bizonne, J.-L. Barrat, L. Bocquet, E. Charlaix, Low-friction flows of liquid at nanopatterned interfaces, Nat Mater, 2(4) (2003) 237-240.
[173] S.J. Kim, Y.J. Park, E.J. Ra, K.K. Kim, K.H. An, Y.H. Lee, J.Y. Choi, C.H. Park, S.K. Doo, M.H. Park, C.W. Yang, Defect-induced loading of Pt nanoparticles on carbon nanotubes, Applied Physics Letters, 90(2) (2007).
[174] J.P. Holman, Experimental methods for engineers, 6th ed., McGraw-Hill, 1994.
[175] W.L. Qu, I. Mudawar, Experimental and numerical study of pressure drop and heat transfer in a single-phase micro-channel heat sink, Int J Heat Mass Tran, 45(12) (2002) 2549-2565.

APPENDIX A

EXPERIMENTAL AND MODELING DETAILS

Details of the FMWCNT synthesis and coating, plasma treatment process, sintering methods, pool boiling experiments and visualization studies are available below:

1. Functionalized multiwall carbon nanotube (FMWCNT) synthesis and deposition

Multiwall carbon nanotubes (MWNTs) were purchased from CheapTubes Inc. (VT, USA). The outer diameter of the MWNT is in the range from 8 to 15 nm and the inside diameter is from 3 to 5 nm and the length is from 10 to 50 μm. The specific surface area is 233 m^2/g.

MWCNTs were oxidized in an acid reflux bath at 80 ºC for 4 hrs to generate defects and to grow hydrophilic carboxylic and hydroxylic functional groups on the surface of each MWNT. Aqua regia, a mixture of HCl (12M) and HNO_3 (16M) in 1:1 volume ratio, was used to oxidize MWNTs. The treated MWNTs were filtered out and thoroughly rinsed with DI water. A sonicator was used to disperse FMWCNTs in isopropyl alcohol to form “inks” for subsequent spray coating. 5 mg of FMWCNTs dispersed in 10 ml of isopropyl alcohol with the addition of 20 mg of a 5% Nafion™ (Dupont DE521) (Fig. A1) solution was used to form the "ink". A 700W, 20 kHz, sonic probe was used to treat the "ink" with Nafion and FMWCN (NFMWCNT) suspension for 1 hour (45 seconds - off and 15 seconds-on duty cycle) at a power level of 30%. Nafion was slowly added into the MWNT mixture while dispersing.

2. FMWCNT dispersion

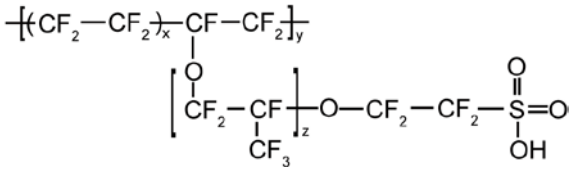

Figure A.1 Chemical formula of Nafion.

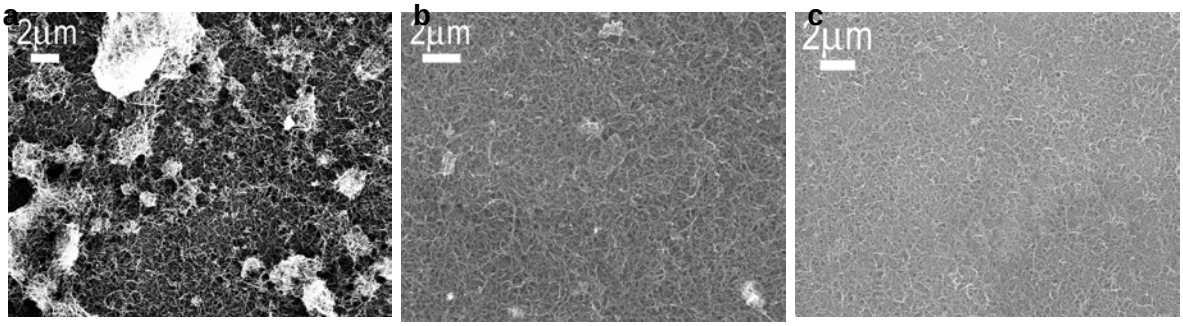

Figure A.2 Characterization of the dispersion of CNTs. (a) pure MWCNTs. (b) FMWCNTs. (c) Mixture of FMWCNTs and nafion with heating treatment.

Figure A.3 Sonotek Exacta-Coat sprayer controlled by X-Y-Z Robot.

The combination of acid reflux treatment and the use of nafion as surfactant resulted in excellent dispersion of CNT in isopropyl alcohol (Fig. A2). As shown in Fig. A2, numerous agglomerations have been observed on the MWCNTs without functional groups (Fig. A2a). After acid treated few agglomerations can be seen in the FMWCNT coatings (Fig. A2b). When FMWCNTs were dispersed in Isopropanol mixed with Nafion,

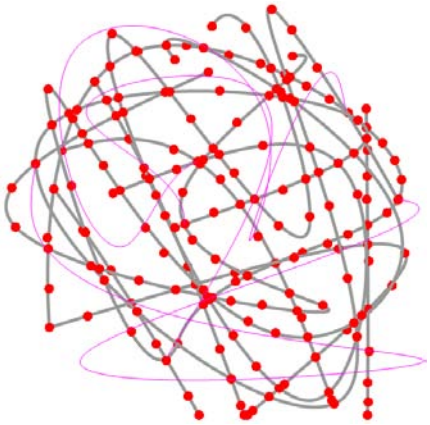

Figure A.4 Mixture of FMWCNTs and Nafions (red dot: functional group; magenta line: Nafion; LT gray line: carbon nanotube).

excellent dispersion was obtained (Fig. A2c).

3. FMWCNT coating

Deposition of the NFMWCNT "ink" was done with an ultrasonic spray coater (Sonotek Exacta-Coat) (Fig. A3). A 120 kHz spray head was used with an ink feed rate of 0.2ml/min. The ultrasonic spray head was programmed to move in a raster pattern at a distance 5 mm from the top surface of the substrate, traversing at a speed of 25 mm/sec, forming a track at the width of approximately 1.25mm. The raster pattern was repeated numerous times (coats) to building up the thickness of the coating. During spray, the substrate was heated to ~100 ºC to speed up the evaporation of the solvent (Fig. A4).

4. Plasma treatment

Oxygen plasma (Plasma Etch Inc., NV, USA) was used to tune the wettability of the interface by controlling the amount and distribution of functional groups on each FMWCNT. The sample was treated at a 6 mL/min flow rate of oxygen at a vacuum of 200.3 Pa. The pristine MWCNT coating needed less plasma treatment time since the bonding between individual CNTs was not as tight as NFMWCNT. The treatment time of FMWCNT coated on the 2-layer mesh required longer time than that on flat copper sheet

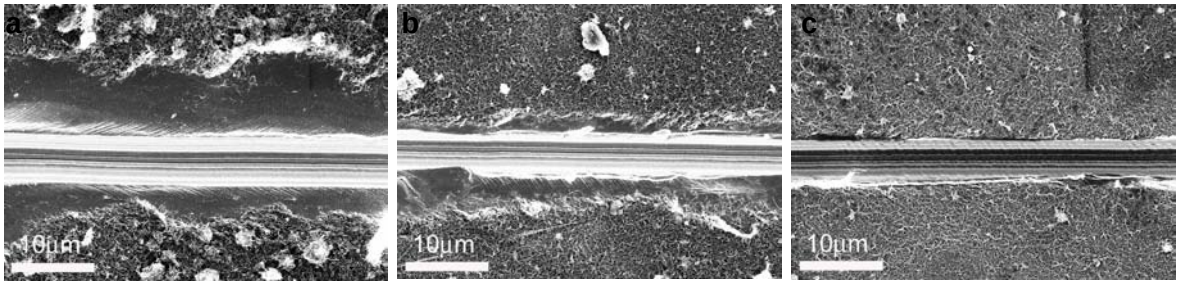

Figure A.5 Characterization of the bonding of CNTs. (a) Scratch on the pure MWCNT coated interface (b) Scratch on the FMWCNT coated interface (c) Scratch on the mixture coated interface.

due to the larger surface area.

5. Scratch test

Microscratch tests were performed using a microtribometer (CETR Inc., CA, USA). A conical diamond indenter with a tip radius of 1.5 μm and an included angle of 60° was attached to a 500 μN load cell, which can record both normal and lateral forces. During scratch tests, the indenter was first brought into contact with the sample surface under a 4 μN normal force and the duration time was 60 s, such setting can keep the indenter in good contact with the sample surfaces. Then the indenter was drawn over a sample surface and the normal force 6 μN was set as constant normal force. The 10 mm long scratches were made by translating the sample ramping the loads on the conical tip over various loads. The normal load was detected *in situ* during scratching.

Pristine CNTs were peeled off near the scratch edge (Fig. A5a), which indicated hydrophobic pristine CNTs were not compatible with copper substrate. However, the bonding between the FMWCNT coating and substrate was improved by inducing hydrophilic functional groups (Fig. A5b). The reason is that the superhydrophicility of functional groups enhanced the bonding to hydrophilic copper substrates. Additionally, amphiphilic Nafion served as a gluing media to further strengthen the bonding after

thermally curing, which is indicated by the residual FMWCNTs wrapped by polymer near the scratch edge (Fig. A5c).

6. Sintering method

Commercially available copper woven meshes (made by Belleville Wire Cloth) are used to serve as main channels for liquid supply. The diffusion bonding technique is employed to achieve nearly perfect contact conditions between the copper meshes and a copper heating block. First fold one-layer mesh to get two-layer meshes and make them sintered together in a high temperature furnace at 1000 ^{o}C in hydrogen (H_2) atmosphere for 2 hours. The surface of the 1×1 cm^2 copper heating block smooth was polished as a mirror and was sintered with the two layer copper meshes on the smooth surface in the same sintering conditions as before.

7. Transmission electron microscopy (TEM)

The distribution and concentration of hydrophilic groups are approximately indicated by tracer particles. Positive charged platinum ions (Pt^{4+}) induced by H_2PtCl_6 were used to locate the distribution of the functional groups on the FMWCNT wires and bundles as the platinum particles are loaded by the defects of FMWCNTs [108, 173]

$$CH_2OHCH_2OH = CH_3CHO+H_2O$$

$$2CH_3CHO + (PtCl_6)^{2-} = 2CH_3CHOO^- + Pt + Cl^- + 4H_2O$$

The Hitachi H8000 Scanning Transmission Electron Microscope (TEM), which is developed to achieve a 1.5 nm scanning transmitted electron image, is used in this work to get the image of Pt loaded FMWCNTs. 200 kV accelerating voltage and 150 K magnification are used to capture the images.

8. Scanning electron microscope (SEM)

The Zeiss Ultraplus thermal field emission scanning electron microscope (SEM), which has a resolution of 1.0 nm at 15 KV at WD = 2 mm, is used to take images of copper woven meshes.

9. Raman analysis

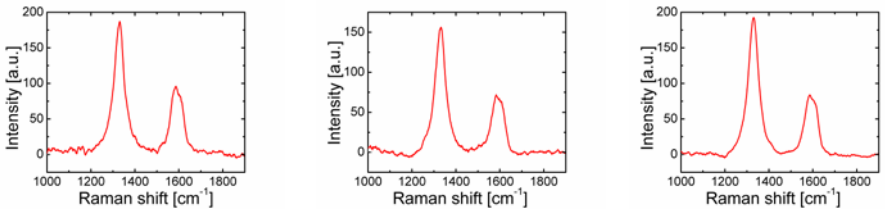

Figure A.6 Intensity ratio as a function of oxygen plasma treatment time. Intesntity ratio and plasma treatment time: I_D/I_G=1.95, 0 S; I_D/I_G=2.22, 30 s; I_D/I_G=2.30, 120 s.

I_D/I_G ratios were analyzed in the LabRAM HR systems. Raman spectra of the samples that were treated by oxygen plasma with different time were collected on a LabRAM HR laser Raman spectrometer with excitation wavelength of 633 nm. Fig. S6 shows the time dependent Raman intensity ratio I_D/I_G. Basically, longer plasma treatment time results in more defects, that is, more functional groups (e.g. C=O, O-C=O, O-H, C_2-F), which was verified by the intensity ratio I_D/I_G.

10. Flow resistance measurement

Flow resistance measurements were conducted in an open test loop as shown in Figure A7. Deionized (DI) water was degassed in a water tank at 10^4 Pa with saturation temperature at approximately 46 ^oC and the water temperature was maintained at 60 ^oC by a flexible silicone-rubber heat sheet (McMaster) for 12 hours prior to tests. The degassed DI water was pumped from a reservoir to the test section by a gear pump (ISMATEC® Regol-z digital) at a constant flow rate. The pump with a digital flow meter was calibrated using a bucket and stopwatch method prior to tests [174]. A differential

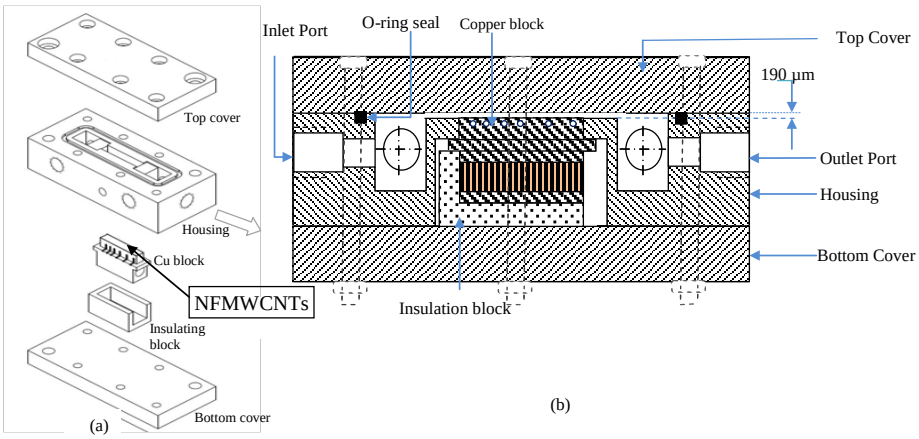

Figure A.7 (a) Test setup assembly. (b) Side view of the test sample and flow direction.

pressure transducer (OMEGADYNE, INC. PX409, 0-15 PSI) was used to measure the pressure drop between the inlet and outlet plenums. The temperature and pressure signals were recorded by an Agilent 34972A data acquisition system.

As shown in Figure A7a, the schematic of the test sample assembly was comprised of two cover plates, a housing block, a copper block and insulation layers. The copper heat sink and heating block were machined from oxygen free single Cu blocks C10100. The copper block was sealed by silicone to avoid leakage.

A desired flow rate was set by the digital gear pump. The electric power was supplied to four heaters by a DC power supply at a given step. The differential pressure and fluid flow rate were monitored and recorded. Two hundred sets of data were collected in steady state.

The measured pressure drop, Δp_m, is between the inlet and the outlet plenums. To eliminate the inlet contraction and outlet expansion pressure losses, the pressure drop (Δp) through the microgap was calculated [175] as: $\Delta p = \Delta p_m - (\Delta p_{c1} + \Delta p_{c2}) - (\Delta p_{e1} + \Delta p_{e2})$, where Δp_{c1} and Δp_{c2} are the contraction pressure losses from the deep plenum to the shallow plenum and from the shallow plenum to the microgap, respectively; Δp_{e1} and

Δp_{e2} are the expansion pressure losses from the shallow plenum to the deep plenum and from the microgap to the shallow plenum, respectively [175]. Reynolds number *Re* is defined as $Re = \rho v D_h/\mu$, where ρ is the water density; v is the average fluid velocity; D_h is the hydrolic diameter and μ is the dynamic viscosity. The relationship between the pressure drop in the microchannel and the reynolds number were ploted in Figure 6.4e.